THE UNIVERSITY of EDINBURGH

Title	Near infrared integral field spectroscopy with UIST
Author	Todd, Stephen Peter.
Qualification	PhD
Year	2003

Thesis scanned from best copy available: may contain faint or blurred text, and/or cropped or missing pages.

Digitisation Notes:

- Pages xiv, 20, 56, 116 and 147 missing from original

Scanned as part of the PhD Thesis Digitisation project
http://libraryblogs.is.ed.ac.uk/phddigitisation

Near-infrared integral field spectroscopy with UIST

STEPHEN PETER TODD

Institute for Astronomy
School of Physics

A thesis submitted to the University of Edinburgh
for the degree of Doctor of Philosophy

October 2003

Abstract

UIST is a facility class near-infrared imager and spectrometer, built at the UK Astronomy Technology Centre (UKATC) in Edinburgh, and now in use at the UK Infrared Telescope (UKIRT). UIST operates at wavelengths of 1–5 μm, providing a variety of imaging and spectroscopy modes. UIST is the first instrument to include a cryogenic deployable integral field unit (IFU), allowing integral field spectroscopy to be carried out over a 3.3 x 6.0 arcsec field of view using any of the grisms available for spectroscopy in UIST.

The optical components of the image slicing IFU were tested and aligned on the bench before the IFU was integrated into UIST for cryogenic tests in the laboratory in Edinburgh and on the telescope. These tests included measurements of the image quality produced by the IFU and the transmission of the IFU relative to a slit of equivalent width as a function of wavelength, found to increase from 0.4 at 1 μm to 0.62 at 2.5 μm. When the seeing is poor and high spectral resolution is required the loss of light in the IFU may be significantly less than the slit-losses from a conventional slit. The conditions under which use of the IFU may be preferable to use of a slit are discussed.

The data reduction methods used to automatically combine IFU observations with arc-lamp spectra, flat-field frames and standard-star spectra in order to transform the two-dimensional output of the IFU into a calibrated (x, y, λ) datacube in near real-time and the procedures required to obtain the necessary calibration data are outlined.

An example of one type of observation made possible by the IFU is shown by observations of H_2 lines excited in bow-shocks in the outflow from a young star in the vicinity of the ultra-compact H II region G25.65+1.05, allowing measurement of the spatial variation of the excitation temperature in these shocks.

Declaration

I hereby declare that this thesis is not substantially the same as any that I have submitted for a degree or diploma or other qualification at any other University. I further state that no part of my thesis has already been or is being concurrently submitted for any such degree, diploma or other qualification.

This thesis is the outcome of my own work except where specifically indicated in the text.

Some of the work presented here has previously been published in S. P. Todd, M. Wells, S. K. Ramsay Howat and P. R. Hastings. A cryogenic image slicing IFU for UKIRT – manufacture, alignment, laboratory testing and data reduction, in *Specialized optical developments in Astronomy* E. Atad-Ettedgui, S. D'Odorico, editors, Proc. SPIE 4842, pp 151–161, 2002.

Stephen Todd
Edinburgh,
October 2003.

Contents

1 Introduction 1

1.1 The importance of integral field spectroscopy 1

1.2 Spectroscopy 3

1.2.1 Dispersing elements 5

1.3 Techniques of integral field spectroscopy 9

1.3.1 Fibre-bundle integral field spectrometers 9

1.3.2 Lenslet array integral field spectrometers 12

1.3.3 Image slicing integral field spectrometers 13

1.4 UIST: A new imaging spectrometer for UKIRT 18

2 UIST and IFU design, testing and alignment 21

2.1 Overview of UIST 21

2.1.1 Reducing background light 22

2.1.2 Imaging 26

2.1.3 Spectroscopy 26

2.1.4 Polarimetry 30

2.1.5 Mechanisms 32

2.2 The Integral Field Unit 33

2.3 Manufacture of the powered mirrors 38

2.4 Testing the mirrors 41

2.5 Aligning the components of the IFU 43

2.5.1 Defining the optical axis 44

2.5.2 Aligning the f-conversion mirror 45

2.5.3 Aligning the slicing mirrors 46

2.5.4 Aligning the image-plane assembly 47
2.5.5 Aligning the image-plane mask 48
2.6 Scattered light in the IFU 49
2.6.1 Absorption and scattering in the IFU 49
2.6.2 Scattering from the slicing mirrors 49
2.6.3 Transmission of the IFU 51
2.6.4 Measuring the throughput using flat-field and arc observations . 52

3 Data-reduction software **57**
3.1 Reducing IFU data 57
3.2 Overview of ORAC-DR 58
3.2.1 Recipes 60
3.2.2 Primitives 60
3.2.3 Calibration data 61
3.2.4 ORAC-DR and UIST 61
3.3 Masking bad pixels and adding variance arrays 62
3.3.1 Readnoise variance 62
3.3.2 Poisson variance 64
3.4 Reduction of flat-field frames 64
3.4.1 Locating the slices on the array 64
3.4.2 Extracting the slices 68
3.4.3 Normalising the flat-field frame 68
3.5 Reduction of arc spectra 69
3.5.1 Determining the wavelength calibration 69
3.5.2 Applying the wavelength calibration 73
3.6 Reduction of standard star observations 75
3.6.1 Sky subtraction and coadding of observations 75
3.6.2 Extracting the standard-star spectrum 77
3.6.3 Forming a datacube 78
3.7 Observing a single pointing 80
3.7.1 Flux calibration 82
3.7.2 Displaying images and spectra 82

3.8 Mapping an extended source 83
3.9 Using these recipes with other IFUs 85

4 On-sky testing of the IFU **87**
4.1 Image reconstruction 87
4.1.1 Measuring the alignment 88
4.1.2 Measuring the plate scale 92
4.1.3 The effect of changing grism on the image reconstruction 92
4.2 Point source image quality 94
4.3 Measuring the throughput using observations of stars 97
4.3.1 Flat-fielding the frame 99
4.3.2 Compensating for slit-losses 101
4.3.3 Results 103
4.4 Comparing the IFU to long-slit spectroscopy 106
4.4.1 Point sources 106
4.4.2 Extended sources 109
4.5 Mapping an extended source 110

5 Shocked H_2 around G25.65+1.05 **117**
5.1 Introduction 117
5.1.1 Bipolar outflows in high-mass star formation 117
5.1.2 G25.65+1.05 120
5.1.3 Shocks 121
5.1.4 Near-infrared molecular hydrogen emission 124
5.2 Observations 127
5.2.1 Imaging 127
5.2.2 Long-slit spectroscopy 128
5.2.3 Integral field spectroscopy 128
5.3 Discussion 143
5.3.1 Morphology 143
5.3.2 Shock excitation 146
5.4 Summary 146

6 Conclusions and future work **149**

6.1 Conclusions 149

6.2 The future of integral field spectroscopy 151

6.2.1 Mid-infrared integral field spectroscopy with the James Webb Space Telescope 151

6.2.2 Multiple integral field spectroscopy 151

List of Figures

1.1 A schematic view of the optics of a long-slit spectrometer 4

1.2 A diffraction grating 5

1.3 The configuration is which grisms are generally used for spectroscopy . 8

1.4 A schematic view of a fibre based IFU 9

1.5 A lenslet array IFU 13

1.6 The optics of 3D, the first image slicing integral field spectrograph 16

1.7 The stepped slit image produced by 3D 17

2.1 An overview of the optical and mechanical layout of UIST 23

2.2 An overview of the optical layout of UIST 24

2.3 The optics of the image rotator 27

2.4 The image rotator flips the image about an axis defined by the angle of the image rotator 28

2.5 A Wollaston prism 31

2.6 The optical layout of the UIST IFU 34

2.7 A photograph of the UIST IFU 35

2.8 The UIST IFU mounted on the slit wheel 35

2.9 If a simple spherical mirror was placed at the slicing plane of the IFU it would form an image of the pupil and the focal plane 36

2.10 The slicing mirrors form two columns of nine pupil images, each containing light from one slice on the sky 36

2.11 Staggering the arrangement of the reimaging mirrors allows these mirrors to be oversized 37

2.12 The order in which the slices of the field of view appear at the output of the IFU 38
2.13 The configuration of the slicing mirrors during machining and in the IFU 40
2.14 A Twyman-Green interferometer 42
2.15 A photograph of the 18 pupils produced by the slices of the IFU superposed on a photograph of the pupil plane mask 47
2.16 The slice images at the output of the IFU 48
2.17 The reflectivity of aluminium 52
2.18 The predicted transmission of the IFU 53
2.19 The measured transmission of the IFU 55
2.20 The variation in transmission from one slice to another 55

3.1 A schematic view of the operation of ORAC-DR 59
3.2 The factor by which the readnoise is reduced for multiple reads was measured for UIST 63
3.3 The REDUCE_FLAT recipe 65
3.4 An unreduced flat field frame 65
3.5 The flat-field frame shown in figure 3.4 after reduction 66
3.6 The REDUCE_ARC recipe 70
3.7 An unreduced arc frame 71
3.8 The slices are extracted from the image shown in figure 3.7, rearranged and approximately aligned 72
3.9 An arc frame after reduction 73
3.10 The STANDARD_STAR recipe 76
3.11 An unreduced standard star spectrum 77
3.12 A reduced standard star spectrum 78
3.13 The 1-d spectrum extracted from the 2-d spectrum shown in figure 3.12 . 79
3.14 Once the spectrum has been formed into a datacube an image can be produced by averaging over a range of wavelengths 80
3.15 The EXTENDED_SOURCE recipe 81
3.16 The MAP_EXTENDED_SOURCE recipe 84

4.1 An image of a star was moved along and across the field of view of the IFU to determine the alignment of the slices relative to one another and the plate scale of each slice 88

4.2 Observations were subtracted in pairs. This image shows the poor image reconstruction before the y-offsets were determined 89

4.3 After measuring and applying the y-offsets the images of the star shown in figure 4.2a are reconstructed accurately 90

4.4 The plate scale of each slice of the IFU 93

4.5 The flux transmitted by the IFU plotted against y-position on the array averaged in the dispersion direction 94

4.6 The shift in position of each slice image on the array as a function of position on the array when the *HK* grism is replaced with the long-J grism or the short-H grism 95

4.7 The point spread function was measured by fitting equation 4.1 to images of a star 98

4.8 Cuts through the stellar image shown in figure 4.7 in the x- and y-direction 99

4.9 The proportion of flux from a gaussian PSF centred on the slit transmitted by a 0.24 arcsec wide slit as a function of FWHM seeing 102

4.10 The inverse of the function plotted in 4.9 102

4.11 The variation of transmission of a 0.24 arcsec wide slit as a point source image is offset from the centre of the slit 103

4.12 The PSF function given in equation 4.1 can be well approximated by the sum of two Gaussian functions 104

4.13 The transmission of the IFU measured from stellar spectra 105

4.14 The ratio of time taken to reach a given signal to noise ratio observing a point source using the IFU to the time taken using the 2 pixel slit 107

4.15 The FWHM seeing at which it would take the same time to reach a given signal to noise ratio using the IFU or the slit 108

4.16 Images of the planetary nebula NGC 7027 extracted from the datacube formed by mosaicing six IFU pointings 111

4.17 A spectrum of NGC 7027, extracted from the same datacube as the images in figure 4.16. 112
4.18 A spectrum of NGC 7027, extracted from the same datacube as the images in figure 4.16. 113

5.1 The structure of a C-shock 124
5.2 Part of the UFTI mosaic images (a) K98 broad-band filter; (b) $1-0$ S(1) narrow-band filter 129
5.3 A continuum subtracted $1-0$ S(1) image created by subtracting figure 5.2a from figure 5.2b 130
5.4 Spectra of sources C and D 131
5.5 The $1-0$ S(1) line extracted from the mosaiced datacube and the temperature map derived from the IFU data 133
5.6 The spectrum obtained by summing over the brightest region of source A 133
5.7 (a) The likelihood of the parameters T and α were evaluated for a single spatial pixel using the intensity of a single spectral line. (b) When other spectral lines are introduced the degeneracy is partly broken 138
5.8 The marginalised likelihood distributions of T and the column densities with a line of the form of equation 5.12 with the most likely value of T and the most likely value of α given T. 139
5.9 The temperature measured along three 0.48 arcsec wide strips running west-east on the left of figure 5.5 144

List of Tables

2.1 The UIST grism set 29
2.2 The radii of curvature of the reimaging mirrors 43
2.3 The offsets of the target image from the optical axis as a function of the rotation of the f-conversion mirror 46

3.1 The values in the `ifu_profile.dat` file, described in the text 67

4.1 The magnification of the 2-d spectrum produced by a given grism relative to that produced by the *HK* grism 96
4.2 Lines detected in the spectrum shown in figure 4.17 114
4.3 Lines detected in the spectrum shown in figure 4.18 115

5.1 The wavelengths, upper energy levels, Einstein A coefficients and degeneracies of the H_2 lines detected in our spectra 135

6.1 The parameters of the four IFUs that will be used in the Mid-infrared instrument (MIRI) on the James Webb Space Telescope 151

Acknowledgments

I would like to thank my supervisors, Suzie Ramsay Howat and Peter Brand, for their support, encouragement and advice over the past three years. I must also thank Martyn Wells, who explained the operation of the IFU to me and showed me how to go about testing and aligning the optical components in the laboratory.

In addition to Suzie and Martyn, I should also thank the rest of the UIST team. They were always willing to explain things to me and made me feel that I was actually contributing something to the project right from the beginning. The development of the data reduction recipes was made significantly easier by the willingness of a number of people to supply technical assistance by email. Tim Jenness, Paul Hirst and Malcolm Currie were always ready to send detailed and helpful explanations and comments. I must also thank all the staff of the Joint Astronomy Centre in Hawaii who provided support or assistance during the commissioning of UIST.

The past three years have been a very enjoyable time, largely due to the friends that I have met here in Edinburgh, particularly the other members of "our year" (Dan, Dave, Olivia, Tara and Ian), who were all people with whom I really enjoyed spending time. Ian was always ready to talk or advise, and his assistance was very helpful when I started using IDL (partly because he always seemed more interested in solving problems in other people's work than in his own). Tara was always ready for interesting discussions on a wide range of topics, and instituted the series of dinner parties to which everyone eventually contributed.

As is traditional, I would like to thank my family for their encouragement throughout my education. Finally, of course, I must also thank Eleanor, my wife, for her love and support.

Chapter 1

Introduction

1.1 The importance of integral field spectroscopy

Almost all astronomical observations are made by detecting photons. Ideally each photon would be detected individually and the position on the sky from which it originated, the energy and polarisation of the photon and the time of arrival would be measured and recorded. This would ensure that all the information obtainable from the the photon would be retained. Modern X-ray telescopes (Chandra and XMM-Newton, for example) come close to this ideal, which is made possible by the low photon arrival rate and the high energy of each photon. At longer wavelengths (optical and infrared) this is not possible due to the large number of photons needed to produce a detectable signal in the presence of background radiation and detector noise and the relatively low energy of each one. Making an infrared observation bins the data to give statistically significant numbers of photons in each bin, allowing measurement and subtraction of the sky background radiation. Each pixel on the detector array is a single bin which covers a known range of angles on the sky, and a known range of photon energies (wavelengths) and each exposure forms one bin over a range of photon arrival times.

The two most common types of instrument found on astronomical telescopes are imagers and spectrometers. An imaging instrument is simply a camera, focusing the image formed by the telescope onto the the detector array. The light is generally passed through a filter. The resulting image is a single (x, y) plane covering a range

of wavelengths defined by the filter. Most spectrometers currently used at optical or infrared wavelengths are long-slit spectrometers, which produce a two-dimensional (y, λ) plane on the detector and can therefore be used to measure the variations in the spectrum across an extended source. Imaging and spectroscopy are both essential techniques for astronomy. Imaging gives information about the relative positions and the morphology of sources, both of which can gives clues to the identification of the sources and the processes by which they were formed. Spectroscopy is essential for constraining models of astronomical sources by providing a means of measuring temperatures, densities, velocities and abundances of molecules, atoms and ions.

For most observations the emission from the target is not time dependent, so in general, to build up as complete a picture as possible of a source, we would like to create a three-dimensional dataset, with two spatial dimensions and one spectral dimension. From such a dataset it would be possible to extract a spectrum at any spatial point on the source or an image at any wavelength. To obtain physical quantities, such as temperature, from an observation it is often necessary to examine the relative intensities of two or more spectral lines. If the data is in the form of an (x, y, λ) datacube then such a measurement can be made at every spatial pixel, giving information about the variation in physical conditions across the source. When a measurement like this is made from a (y, λ) long-slit spectrum the variation is only measured along a single strip of the source, forcing the observer to make more assumptions about the morphology of the source when interpreting the measurements.

It is possible to build up a three-dimensional (x, y, λ) datacube by taking a series of two-dimensional observations which scan across the third dimension. A Fabry-Perot interferometer can be used as a very narrow-band tunable filter to take a series of images at different λ, each forming a (x, y) plane of the datacube. This is an efficient method of observing a small wavelength range over a relatively large area, which might be useful for making a velocity map of a single spectral line. Alternatively, a long-slit spectrometer can be scanned across the source with each observation forming a (y, λ) plane of the datacube. This provides a large spectral coverage but is inefficient for small sources because most of the length of the slit is empty and is slow for observing larger sources because a large number of slit positions are required. Both of these

methods have the significant disadvantage that they involve taking a sequence of observations and are therefore seriously affected by variations in atmospheric opacity or seeing.

Integral field spectroscopy is a term used to describe observational techniques which allow all three dimensions of the (x, y, λ) datacube to be measured simultaneously. There are a number of techniques used at optical and infrared wavelengths, which are described below. The total number of pixels in the datacube is limited by the number of pixels on the detector array, but the number of pixels in each dimension can be chosen when the instrument is designed to maximise the efficiency of certain types of observations. By observing all three dimensions simultaneously the problems caused by varying atmospheric conditions are greatly reduced.

1.2 Spectroscopy

The layout of a basic spectrometer is shown in figure 1.1. The light to be analysed enters the spectrometer through the entrance slit. The collimator forms the light from each point on the entrance slit into a beam of parallel rays. If the dispersing element were not present the camera would simply form an image of the entrance slit on the detector. The dispersing element is a grating, prism or grism (described below), which bends the light through an angle which is a function of wavelength. This, therefore, shifts the image of the slit on the detector by a distance which depends on the wavelength, forming a spectrum. In a long-slit spectrometer the input slit is placed at the focal plane of the telescope so that the slit selects an approximately one-dimensional strip of the image. By examining the variation of the spectrum formed along the length of the slit (perpendicular to the dispersion direction) it is possible to measure the variation of the spectrum across an extended source, or to measure the spectra of two stars simultaneously by finding a slit position which crosses both. The slit is generally narrower than the point-spread function in the image so the narrow strip of the image can be assumed to vary only along its length, and can be treated as a one dimensional cross-section of the image.

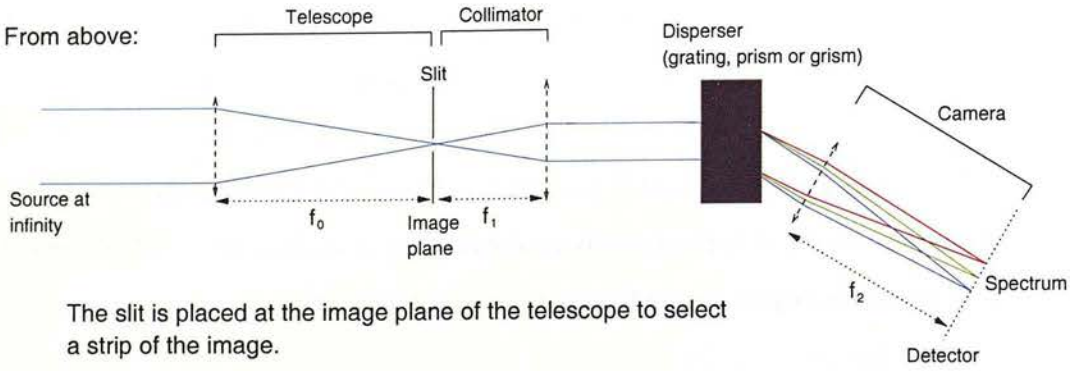

Figure 1.1: A basic long-slit spectrometer as viewed from above and from the side. From the side neither slit nor the dispersing element have any effect, so the system is simply imaging the source. Note that while the coloured lines in the view from above represent light of different wavelengths, in the view from the side they represent light from different sources.

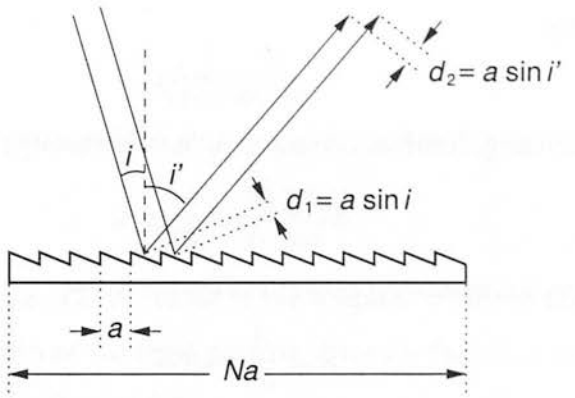

Figure 1.2: A diffraction grating with N grooves with separation a. Constructive interference is produced when the optical path difference $(d_1 + d_2) = (a \sin i + a \sin i')$ is an integer number of wavelengths.

1.2.1 Dispersing elements

Diffraction gratings

We consider a diffraction grating with N grooves with separation a with light incident at an angle i and diffracted to an angle i' (as shown in figure 1.2). The condition for constructive interference is

$$\sin i \pm \sin i' = \frac{m\lambda}{a}$$

where m is an integer and the sign on the left is $+$ for a reflection grating and $-$ for a transmission grating. The angular dispersion, A, is obtained by differentiating this equation:

$$A = \frac{di'}{d\lambda} = \frac{m}{a \cos i'}.$$

The linear dispersion at the detector is obtained by multiplying A by the focal length of the camera, f_2:

$$\frac{dl}{d\lambda} = f_2 A.$$

There is a fundamental limit on the spectral resolution obtainable with a given grating. Viewed from an angle i' (from the camera positioned to focus the diffracted light onto the detector) the grating has an angular width of $Na \cos i'$, so the diffraction limit on the minimum angular width of the image that would be formed on the

detector is given by

$$\delta i' = \frac{\lambda}{Na\cos i'}.$$

The minimum wavelength difference resolvable is, therefore,

$$\delta\lambda = \frac{\delta i'}{A} = \frac{\lambda}{mN}.$$

The maximum spectral resolving power is then given by

$$R = \frac{\lambda}{\delta\lambda} = mN.$$

In practice, as we see below, this maximum spectral resolution is rarely reached due to the non-zero width of the entrance slit of the spectrometer.

In order to find the spectral resolving power with a non-zero width slit it is helpful to use the principle of conservation of étendue in optical systems, normally stated as $n\Omega A = \text{constant}$, where Ω is the solid angle of the beam incident on an area A in a medium of refractive index n. In vacuum or air, and in one dimension this simplifies to $\omega a = \text{constant}$, where ω and a are the opening angle of the beam and the width of the aperture.

The image from the telescope, which has focal length f_0 and diameter d_0 (and hence focal ratio $F_0 = f_0/d_0$) is focused onto the entrance slit which has width w. On the sky the slit subtends an angle of ϕ_w, where $\phi_w = w/f_0$. The light passes through a collimator with focal length f_1 and diameter d_1 ($F_1 = f_1/d1$). After passing through the dispersing element with angular dispersion A the slit is imaged by a camera with focal length f_2 and diameter d_2 ($F_2 = f_2/d_2$) onto the detector array. The monochromatic image of the slit on the detector has width w'. The opening angle of the beam is the inverse of the focal ratio so, using the conservation of étendue described above, we find

$$\frac{w}{F_1} = \frac{w'}{F_2}.$$

If we define the minimum resolvable wavelength difference, $\delta\lambda$, as that which gives a separation on the detector equal to the slit image width then

$$\delta\lambda = \left(\frac{d\lambda}{dl}\right) w' = \frac{awF_2\cos i'}{mf_2F_1}.$$

The width of the part of the grating illuminated by the beam, W is given by

$$W = \frac{d_2}{\cos i'},$$

and $F_2/f_2 = 1/d_2$, so

$$\delta\lambda = \frac{aw}{mF_1W}.$$

The spectral resolving power of the spectrometer is defined as

$$R = \frac{\lambda}{\delta\lambda} = \frac{mF_1W\lambda}{aw}.$$

It is more useful to express this in terms of the angular width of the slit on the sky, $\phi_w = w/f_0$. The focal ratio of the light passing through the slit is unchanged by the slit, so $F_1 = F_0 = f_0/d_0$. We then find that

$$R = \frac{mW\lambda}{ad_0\phi_w}.$$

This equation is valid even if the image from the telescope is reimaged onto the slit rather than directly illuminating it because $d_0\phi_w$ will be unchanged by the reimaging optics due to conservation of étendue. From this equation it can be seen that to maintain the spectral resolving power of a spectrograph when moving to a larger telescope either the slit must be narrower on the sky, which will reduce the transmitted flux, or the number of lines on the grating must be increased in proportion with the size of the telescope, either by decreasing the spacing, a, or by increasing the size of the grating (and hence the dimensions of the whole instrument).

Grisms

A grism is a prism with a grating ruled on one surface. If we consider two rays of light passing through a prism with angle α and refractive index n with a grating with lines separated by a distance a on the exit surface of the prism, as shown in figure 1.3, then we can calculate where constructive interference will occur. Within the grism, path 1 is longer than path 2 by $a \sin\alpha$, creating an optical path difference of $na \sin\alpha$. Between the grism and the detector, path 1 is shorter than path 2 by $a \sin\theta$. Constructive interference will occur when the total optical path difference is an integer multiple of the wavelength:

$$na \sin\alpha - a \sin\theta = m\lambda.$$

The same derivation can then be followed as for the grating, yielding the same result:

$$R = \frac{mW\lambda}{ad_0\phi_w}.$$

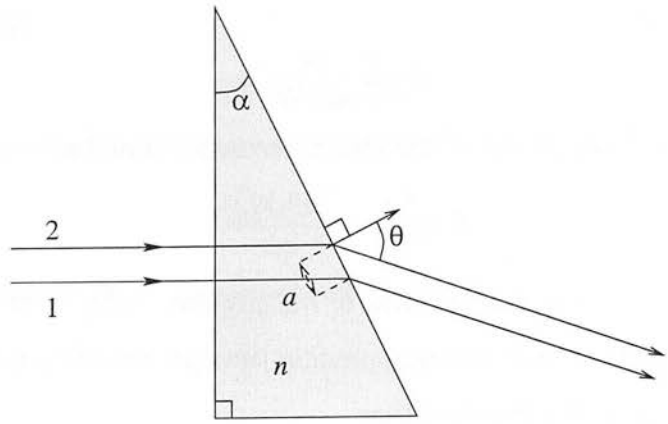

Figure 1.3: The configuration is which grisms are generally used for spectroscopy.

The advantage of using a grism is that the grating spacing, prism angle and refractive index of the material can be chosen to give the desired spectral resolution and to centre the desired spectral range on the undeviated beam. Avoiding the large off-axis angles of grating based spectrometers makes the design of a combined imager and spectrometer using a single detector array far more simple and compact because when the slit and the grism are inserted into the beam the spectrum is formed where the image had previously been. In this configuration

$$(n-1)\sin\alpha = \frac{m\lambda}{a}.$$

The width of the illuminated part of the grating is given by $W = d_1/\cos\alpha$, so

$$R = \frac{(n-1)d_1\tan\alpha}{d_0\phi_w}.$$

The main disadvantage of using a grism rather than a grating is that the central wavelength and spectral resolving power are reduced by a factor of approximately $2/(n-1)$, so if conventional glasses are used, which typically have refractive indices of around 1.5, the line spacing must be decreased by a factor of 4 compared to that on a grating for use at the same wavelength and spectral resolution. It is therefore necessary to use more exotic optical materials with high refractive indices. Most of the UIST grisms are manufactured from KRS5, which has a refractive index of 2.5, but is mechanically fragile, difficult to machine and highly toxic.

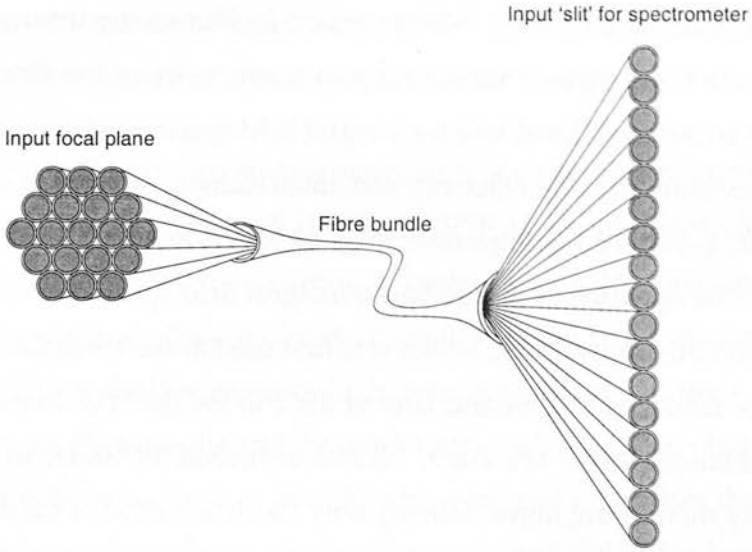

Figure 1.4: A schematic view of a fibre based IFU, as described in the text.

1.3 Techniques of integral field spectroscopy

Integral field spectrometers work by reformatting a two-dimensional field of view in some way and using this reformatted image as the input to the spectrometer in place of the slit. Each pixel in the output from the spectrometer corresponds to one (x, y, λ) pixel in the datacube. Data-reduction software can then be used to construct the datacube from the 2-d frame. The part of the instrument which carries out this reformatting is known as an integral-field unit (IFU). A variety of techniques are used to reform the image. These are summarised below.

1.3.1 Fibre-bundle integral field spectrometers

Fibre based integral field spectrometers use a bundle of optical fibres arranged in a two-dimensional pattern at the focal plane of the telescope and in a line to form the input slit of the spectrometer, thereby mapping each pixel along the length of the 'slit' to a pixel on the sky, shown schematically in figure 1.4.

This technique was first used in the Medusa spectrograph built for the Steward 90 inch telescope [Hill et al., 1980]. This allowed spectroscopy of around 40 objects simultaneously by inserting fibres into a custom-made metal plate to align the fibres to individual sources on the sky. Another instrument of this type was FOCAP at the

Anglo-Australian Telescope [Gray, 1986] in which 50 fibres were inserted into holes in a custom-made brass plate. Plates were also made to space the fibres at regular intervals over a two-dimensional area for integral field spectroscopy, but it was found that the low maximum packing efficiency and small number of fibres, combined with the loss of light, gave no advantage over long-slit spectroscopy. The first spectrometer designed to be operated as a fibre-based integral field spectrometer was SILFID [Vanderriest and Lemonnier, 1987], which was first used at the 1.9-m Observatoire de Haute-Provence telescope in 1984 and later at the 2-m Pic du Midi telescope and the 3.6-m Canada-France-Hawaii telescope. SILFID contained 397 fibres in a hexagonal field and 100 sky monitoring fibres. Initially only about one third of the field could be used due to the small size of available detector arrays, but the development of large format (2048 $\times$ 2048 pixel) CCDs enabled the entire field to be used.

The two main disadvantages of fibre-based IFUs were discussed by Allington-Smith and Content [1998]:

1. The sensitivity and photometric accuracy of fibre-based IFUs is reduced because of the low packing efficiency of the fibres at the focal plane. The filling factor, ϕ, is

$$\phi = \frac{\pi}{2\sqrt{3}} \left(\frac{d_1}{d_2} \right)^2$$

where d_1 and d_2 are the diameter of the fibre core and the outer diameter of the fibre. The fibre cladding must be at least 10λ thick to avoid significant losses via evanescent waves. Typically fibres used in IFUs have $d_1 = 50$–100 μm, giving maximum filling factors of 63–75%.

2. If input beams slower than about f/5 are used then focal ratio degradation (FRD) becomes a problem and the output beam is broadened, becoming faster than the input beam. This does not conserve étendue ($A\Omega$ – the product of the aperture size and solid angle of the beam at that aperture), which is equivalent to increasing in entropy, or losing information. The spectrograph must be oversized to avoid loss of light and the shadow of the telescope primary mirror is blurred at the pupil plane preventing the use of optics with internal obstructions. If the focal ratio of the input beam from the telescope is reduced in order to minimise

FRD then the size of the input focal plane is reduced which may increase problems with the filling factor and sampling of the image.

A number of optical instruments recently built or currently under construction, including GMOS [Gemini], FLAMES [VLT] and SPIRAL [Anglo-Australian Telescope], have overcome these problems by using a lenslet array with a packing efficiency of 100% at the focal plane. This produces an array of small pupil images with a much faster beam. This technique requires high precision manufacturing – any misalignment between the fibre bundle and the lenslet array will lose flux – but when aligned allows all the light to be focused into the fibre core and minimises the losses due to FRD. A linear array of lenslets may be used at the output of the fibre bundle to convert the beam to a focal ratio compatible with an existing spectrograph.

In all fibre-based IFUs, whether lenslets are used or not, a compromise must be reached between making efficient use of the array area and reducing the overlap between the spectra from adjacent fibres in the slit. In GMOS the fibres are arranged so that adjacent fibres in the slit are also adjacent in the input focal plane [Allington-Smith and Content, 1998]. This, combined with the common wavelength scale of all the spectra due to the straight input slit to the spectrograph makes this analogous to adjacent pixels along the slit of a conventional long slit spectrograph. Some overlap is then acceptable, producing only a small reduction in spatial resolution if the spacing between fibre centres was kept above $\sim$ 4 pixels. A pitch of 4.3 pixels/fibre was selected as the best compromise for the GMOS IFU between maintaining spatial resolution and making good use of the array.

All the instruments mentioned above operate at optical wavelengths. A number of instruments have also used fibres for integral field spectroscopy at near-infrared wavelengths. The first such instrument was ISIS-IR [Dallier et al., 1994] at the Canada-France-Hawaii Telescope (CFHT), which used silica fibres to feed a warm spectrometer operating in the J and H bands. Other fibre based infrared IFUs operating in the J include COHSI [Kenworthy et al., 1998], which included a mask to suppress the bright OH lines, allowing observations of faint extended sources such as high redshift galaxies and gravitational arcs, CIRPASS [Parry et al., 2000], SMIRFS [Haynes and Allington-Smith, 1998], which was a fibre-based IFU used to feed the CGS4 long-slit

spectrometer on UKIRT using both silica and zirconium fluoride fibres to operate at *J*, *H* and *K* and FMOS, currently under construction for Subaru. All of these instruments used fibres at room temperature to feed a cryogenic spectrometer. Silica fibres provide good transmission at wavelengths short of 2.3 μm. Alternatively zirconium fluoride fibres can be used to provide good transmission at 0.8–4.3 μm but are more fragile and more expensive. For use at wavelengths where the thermal emission of the parts of the instrument at room temperature becomes significant (from about the middle of the *K* band), it would be necessary to cool the fibres. Lee et al. [2001] carried out an investigation of the properties of optical fibres at cryogenic temperatures. They found that, providing the fibres were mounted to avoid the build up of stresses during cooling, the focal ratio degradation was not greatly increased and the fibres remained flexible. There seem, therefore, to be no obstacles to using fibres at cryogenic temperatures to make observations in the thermal near-infrared in future instruments.

1.3.2 Lenslet array integral field spectrometers

If an array of lenslets is placed at the focal plane of the telescope then an array of small pupil images is formed. Each image is an image of the input pupil of the system, generally the telescope primary mirror, containing only light from one spatial pixel of the image. This array of pupil images can then be used as the input to the spectrometer in place of a slit. This is similar to the technique of slitless spectroscopy sometimes used to observe multiple point sources in an otherwise sparsely populated field of view. The dispersion axis is rotated slightly relative to the axes of the lenslet array to make maximum use of the array area, as shown in figure 1.5. Spectral coverage is generally limited with a band-pass filter to limit the length of the spectra, preventing them overlapping. The filling factor on the array tends to be rather low because cross-talk between adjacent spectra must be avoided due to the large offset in wavelength scale between adjacent spectra, so a bright wavelength range in the spectrum from one lenslet may be adjacent to a faint region in the spectrum from another.

The first integral field spectrograph of this type was TIGER [Courtès et al., 1987], built for the 3.6 m Canada-France-Hawaii Telescope (CFHT) and first used in 1987 . The image from the telescope was enlarged and focused onto an array of small silica

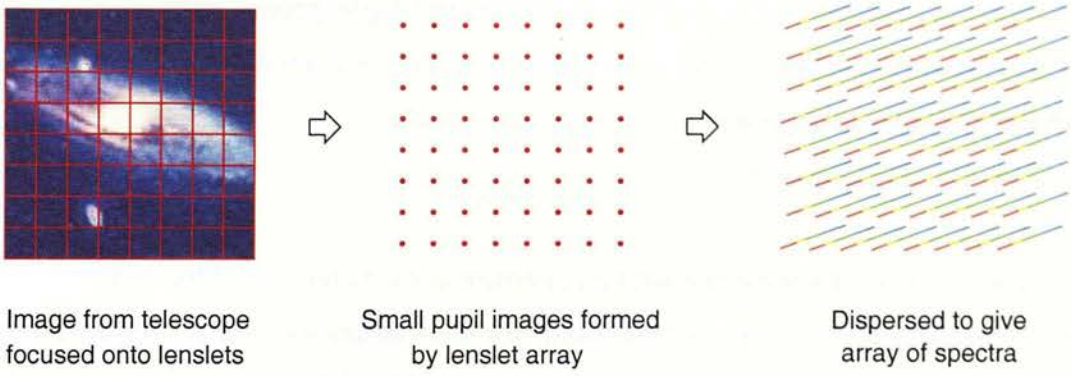

Figure 1.5: In a lenslet array IFU the image from the telescope is focused onto the lenslets. These form an array of small pupil images, each containing light from one spatial pixel. This is used as the input to the spectrometer. The dispersion axis is rotated relative to the axes of the lenslet array to make efficient use of the array area.

lenses. Using a 640×1024 pixel CCD it was possible to observe a 7×9 array of spectra with a filling factor on the CCD of 0.5. More recently SAURON [Bacon et al., 2001] has been built for the 4.2 m William Herschel Telescope (WHT), covering a (41×33) arcsec^2 field of view with (0.94×0.94) arcsec^2 square lenslets or a (9×11) arcsec^2 field of view with (0.27×0.27) arcsec^2 lenslets to fully sample the seeing at La Palma. A patch of sky 1.9 arcmin away is measured simultaneously for sky subtraction. To make more efficient use of the array area a low level of cross-talk was accepted and is removed in the data-reduction pipeline.

Lenslet based IFUs are optically simpler than other types of IFU, making manufacture and alignment easier and throughput higher. A large number of spatial pixels can be observed, giving a wide field of view, but spectral coverage is limited by the need to avoid overlaps between spectra. The need to keep cross-talk to an acceptable level results in relatively inefficient use of the array.

1.3.3 Image slicing integral field spectrometers

Image slicers to reduce slit-losses

Early image slicers were not built to allow integral field spectroscopy, but to slice and reformat the point spread function from a star in order to pass a large fraction of the

flux though a narrow slit, giving low slit-losses and high spectral resolution. Bowen [1938] showed the necessity for such a device as follows: the image of a stellar PSF which subtends an angle ϕ on the sky has a diameter

$$a = \phi d_0 F_0$$

at the focal plane of a telescope with an aperture of diameter d_0 and focal ratio F_0. If a spectrograph with slit width w and collimator and camera lenses with effective focal ratios $F_{\rm coll}$ and $F_{\rm cam}$ to produce a slit image with width w' then

$$\frac{w}{F_{\rm coll}} = \frac{w'}{F_{\rm cam}}.$$

If we model the stellar image as a uniformly illuminated circle of diameter a, centred on the slit, then the fraction of light transmitted by the slit is approximately given by

$$R \approx \frac{aw}{\pi(a/2)^2} = \frac{4F_{\rm coll}w'}{\pi F_{\rm cam}\phi d_0 F_0}.$$

If all the light entering the spectrograph is to pass through the collimator then $F_{\rm coll} \leq F_0$, and the maximum efficiency is therefore

$$R \approx \frac{4w'}{\pi\alpha d_0 F_{\rm cam}}.$$

From this we can see that the efficiency is independent of the focal ratio of the telescope and the collimator. Reducing a by the introduction of condensing lenses in front of the slit makes no difference. For the Palomar 200 inch telescope, with 1 arcsec seeing, $F_{\rm cam} = 30$ and $w' = 30$ μm (the resolution of a photographic plate) the efficiency is only 5%.

Changing the area of the stellar image using condensing lenses does not help, but rearranging the shape without changing the area does. Bowen went on to propose a design for an image slicer to be placed close to the image plane of the telescope. This allowed most of the light to pass though the slit, producing a much wider spectrum perpendicular to the dispersion direction. A cylindrical lens was then used to decrease the width of the spectrum in this direction and hence increase the intensity at the photographic plate. An alternative image slicing method was proposed by Richardson [1968]. Image slicers based on both these design were built and used on a number of telescopes for stellar spectroscopy.

Neither of these designs is suitable for use in integral field spectroscopy because the path lengths of the different slices are not the same. Some of the slices would be significantly out of focus at the slit plane. This does not reduce the spectral resolution if the slit is used to limit the width of the sliced image, but it would greatly reduce the spatial resolution.

Image slicers as IFUs

An image slicing integral field spectrometer slices a two-dimensional field of view into strips, maintaining spatial resolution within each strip, then re-arranges these strips to form the input slit to the spectrometer. The output from each slice is effectively an individual long-slit spectrum, so the effect is that of simultaneously observing a number of long-slit spectra from adjacent slits. One advantage of image slicers over other types of IFU is the efficient use which can be made of the array. Within the two-dimensional spectrum produced by each slice all of the pixels on the array are used. The only pixels not used are those between slices. The packing efficiency on the array can be very close to 100%. All of the image slicing IFUs currently in use or under development are designed to operate in the near-infrared. Image slicers are particularly suitable for use at infrared wavelengths and in cryogenic instruments due to their all reflective optics, therefore eliminating the need to develop new techniques. While the use of fibres at cryogenic temperatures appears practical, as discussed above, it still requires refinements of the techniques used when working with fibres at room temperatures. Image slicers allow the use of well understood, proven manufacturing techniques.

The first instrument of this type was 3D [Weitzel et al., 1996] which operated at wavelengths of 1.2 to 2.45 μm. It consisted of a 16 slice IFU at room temperature feeding light into a cryogenic spectrometer. The image from the telescope was focused onto a stack of flat slicing mirrors, each 8 mm long and 0.4 mm wide, and each rotated by a different angle. A second set of flat mirrors rearranges the slices into a long stepped slit. It was essential that the 16 slice images all appear to come from a common pupil so that an aperture stop could be used within the spectrometer to absorb the background flux. It was also necessary to maintain equal optical path lengths for all 16 slices. These conditions were met by arranging the second set of mirrors along a

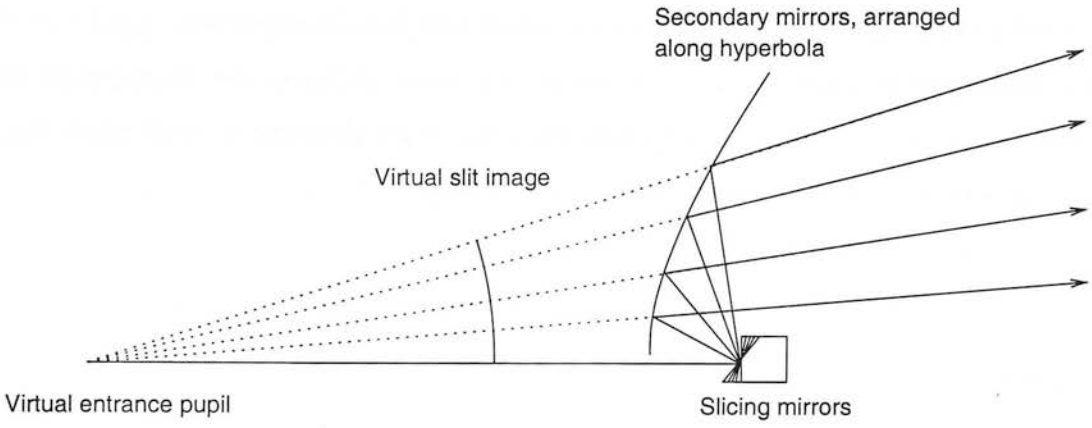

Figure 1.6: 3D was the first image slicing integral field spectrograph. A stack of flat slicing mirrors was placed at the telescope focal plane. A set of secondary mirrors were arranged along and tangential to a hyperbola to give all slices the same optical path length, forming a common virtual input pupil. A set of virtual images of the slices are formed in a slightly curved plane.

hyperbola and tangential to it as shown in figure 1.6. This hyperbola has one focus at the telescope focus, which is where the slicing mirrors are located, and the other focus is at the position of the new virtual entrance pupil. This produces a virtual image of a stepped slit, as shown in 1.7, which is used as the input to the spectrometer.

This design results in the virtual images of the 16 slits lying along the circumference of a circle rather than in a single, flat focal plane. This results in a small defocus of the slice images and the spectrometer was therefore required to focus all 16 slightly defocused slice images with sufficient image quality.

The image slicer of 3D was at room temperature and passed the light through a window into the cryogenic spectrometer. This significantly increased the background levels because at each slice position along the staggered slit image there is actually an image of all 16 slices, one of which is illuminated by the sky and the other 15 of which are reflecting the inside of the IFU housing.

A similar image slicing integral field spectrograph was built for the Palomar 200 inch telescope [Murphy et al., 1999]. This used a cryogenic image slicer to feed one of two spectrographs, allowing operation from 1–5 μm. The image slicer produces two columns of slice images, doubling the number of spatial pixels available on the ($256 \times$

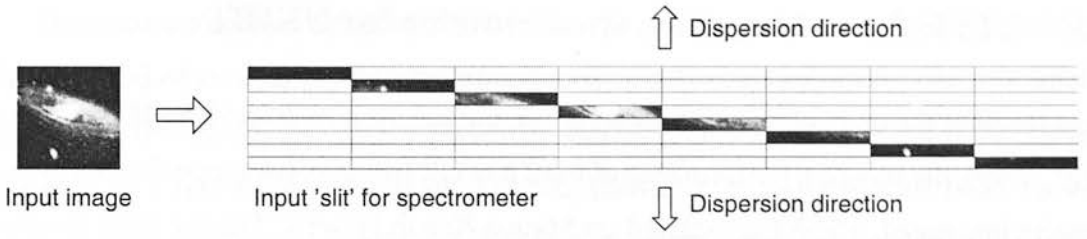

Figure 1.7: The virtual slit image produced by 3D as the input for the spectrometer is a stepped slit. Each of the secondary mirrors produced an image of all the slicing mirrors, only one of which will be reflecting illumination from the sky. The others will be reflecting the dark interior of the instrument.

256) pixel array, while halving the number of pixels available in the spectral dimension. Other image slicers are currently under development. SPIFFI (for the VLT) is based on the the design of 3D [Tecza et al., 2000], which is updated to take advantage of the larger infrared arrays now available (1024 × 1024 pixels) and the spatial resolution available from the VLT with adaptive optics, with exchangable pre-optics providing pixel scales of 0.25 arcsec, 0.1 arcsec and 0.025 arcsec.

The image slicing integral field spectrographs mentioned so far have used flat slicing mirrors, but Content [1997] proposed the use of spherical mirrors to make the design more compact. In this design the slicing mirrors were all part of a common spherical surface and were then tilted relative to one another as in 3D. The effect of this is that the slicing mirrors each form an image of the entrance pupil. The secondary mirrors are also concave spherical surfaces and are positioned at these pupil images. This makes the secondary mirrors much smaller than in previous designs, reducing the maximum angle of tilt necessary on the slicing mirrors and hence the variation in focus position along the slice. The secondary mirrors form a real, rather than a virtual, image of the staggered slit to be used as the input to the spectrometer. This allows IFUs of this design to be used to feed light into existing spectrometers which are not designed to accommodate virtual slit images. This design also dramatically reduces the size of the spectrometer optics. The two IFUs with different spatial resolutions designed for GNIRS on Gemini are based on this concept [Dubbeldam et al., 2000], and are sufficiently compact that they will be deployed by the GNIRS slit-slide mechanism.

1.4 UIST: A new imaging spectrometer for UKIRT

As a result of the upgrades programme carried out between 1990 and 1998 [Hawarden et al., 1999], the imaging performance of the 3.8 m UK Infrared Telescope (UKIRT) was greatly improved. UKIRT is situated on Mauna Kea in Hawaii. During 2001 images with FWHM < 0.6 arcsec were produced 53% of the time and < 0.4 arcsec 13% of the time [Seigar et al., 2002]. In November 1998 *K*-band images with FWHM of 0.17 arcsec were observed at UKIRT. New instruments were required to take advantage of the increased spatial resolution. A simple imager, UFTI [Roche et al., 2003], operating at wavelengths of 1–2.5 μm was rapidly developed to provide high resolution imaging at short wavelengths, and was commissioned in 1998. UIST (the UKIRT Imager Spectrometer) was developed to be a a facility class near-infrared imager and spectrometer operating at wavelengths of 1–5 μm [Ramsay Howat et al., 2000], making use of the high image quality.

The development of large infrared arrays (1024×1024 pixels) made the inclusion of an IFU an attractive way to take advantage of the high spatial resolution. An image slicing design was chosen, primarily due to the uncertainties over the difficulties of using fibres in a cryogenic environment and the recent success of the 3D instrument. UIST was designed primarily as an imager and long-slit spectrometer. It was essential that the IFU could easily be deployed without complicating the design of the rest of the instrument. This made it essential that the IFU was compact enough to be mounted on the slit wheel, used to switch between different slits for spectroscopy and apertures for imaging. For this reason a design based on the concepts described by Content [1997] was selected.

The parameters of the IFU are fairly well determined just by the design of the rest of the instrument. The plate scale used for long-slit spectroscopy is 0.12 arcsec/pixel, to fully sample the PSF under almost all seeing conditions. The slice images produced by the IFU should be at this same plate scale. To produce a fully sampled spectrum the slice images should be 2 pixels wide at the detector, or 0.24 arcsec on the sky. The total number of spatial pixels is limited by the dimensions of the array to 1024. The final design used 18 slices, each 0.24 arcsec wide and 6.0 arcsec long on the sky to provide a field of view of 4.3×6.0 arcsec.

There are a number of classes of astronomical sources which are similar in scale to the IFU field of view, and could therefore be efficiently observed using one or a small number of IFU pointings. Active galactic nuclei (AGN) typically contain structure on the scale of a few arcsec. For example NGC 1068 shows jets on a scale of 13 arcsec and a narrow line region of highly excited gas 6 arcsec across. Observations of near-infrared wavelengths are important for understanding high redshift galaxies because at redshifts greater than 1 the bulk of the emission from the stellar population is shifted into the *J*, *H* and *K* bands. The Hα line, a commonly used diagnostic of star formation, is shifted to a wavelength of 1 μm at redshift 0.6. Many of the phenomena associated with star-formation within our galaxy are also best studied in the near-infrared due to the high extinction by dust at optical wavelengths. As I will show in chapter 5, regions of shocked molecular gas can be observed in star forming regions at scales of a few arcsec. The IFU can also be used to obtain spectra of a number of stars in a cluster simultaneously, as demonstrated by Krabbe et al. [1995], who used 3D to obtain spectra from 25 stars within an 8×8 arcsec field of the galactic centre.

A large project such as UIST involves the collaboration of a relatively large number of people. At the time that I joined the project the design of UIST, including the IFU, had been finalised, and many of the components manufactured. I was responsible for testing and aligning the components of the IFU in collaboration with Martyn Wells. Once the instrument was assembled I assisted in testing the UIST mechanisms in the laboratory. I carried out the analysis of the expected transmission of the IFU and the measurements of the transmission (chapter 2). I also wrote the scripts required to transform the raw IFU data into calibrated datacubes using the ORAC-DR data reduction system, re-using many of the components already used for spectroscopy data reduction at UKIRT (chapter 3). Once UIST had been installed on UKIRT, I spent two months in Hawaii commissioning the instrument with Suzanne Ramsay Howat, Chris Davis and Sandy Leggett. During this period I was responsible for making and processing all the measurements required to test and calibrate the IFU (chapter 4). During the commissioning period I also obtained observations of a compact region of shocked gas in a region of high-mass star formation, demonstrating one type of observation for which the IFU is ideally suited (chapter 5).

Chapter 2

UIST and IFU design, testing and alignment

At the time that I joined the UIST project the design of the instrument had been finalised and many of the components manufactured. In this chapter I will give an overview of the design of UIST. I will then describe the procedures used to align and test the components of the IFU, which I was responsible for, in collaboration with Martyn Wells. Once the instrument was assembled I assisted in testing the UIST mechanisms in the laboratory. I carried out the analysis of the expected transmission of the IFU and the measurements of the transmission which are presented towards the end of this chapter.

2.1 Overview of UIST

The detector used in UIST is a 1024 × 1024 InSb array which has high sensitivity at wavelengths of 1 to 5 μm. It is possible to switch between imaging, long-slit spectroscopy, imaging polarimetry, spectropolarimetry and integral field spectroscopy or to switch to any of the filters or grisms (the dispersing elements used for spectroscopy) within around 30 seconds. The plate scale in most observing modes is 0.12 arcsec/pixel, giving a field of view 2 arcmin across. In imaging mode it is possible to switch to a plate scale of 0.06 arcsec/pixel with a 1 × 1 arcmin field of view to ensure that the point spread function is fully-sampled or over-sampled during even the best seeing

conditions observed at UKIRT.

UIST is constructed as a series of modules, as shown in figure 2.1. Each is individually internally aligned and they are then aligned to one another on the optical bench which forms the lid of the cryostat. All the modules and the optical bench are manufactured from the same aluminium alloy, eliminating differential contraction as the instrument is cooled to its operating temperature of 65 K, necessary to reduce thermal emission from the instrument itself which would make observations in the *K* band and at longer wavelengths impossible. The alignment can be carried out at room temperature and will be maintained when UIST is cold.

The optical layout of UIST can be seen in figures 2.1 and 2.2. The light enters the instrument from the telescope though a CaF_2 window, reaching a focus just inside the instrument. The beam is collimated by lenses L1–3 in figure 2.2, forming a pupil image (an image of the telescope secondary mirror) at a cold-stop. The collimated beam passes through two filter wheels and is then focused onto the slit plane by L4 and L5. The image rotator consists of three flat mirrors (M1–3) which can be rotated about the optical axis to rotate the image of the sky formed on the slit, equivalent to being able to rotate the slit to position it across the features of interest in a source. The beam is again collimated before passing through the two grism wheels, and is then focused by the camera onto the array. The array can be moved along the optical axis by the focus mechanism, required because of the many refractive elements in the UIST optics.

2.1.1 Reducing background light

One of the main challenges of building a telescope and instrument to operate at infrared wavelengths is reducing background radiation. It is essential that the temperature of the instrument itself is reduced – UIST operates at 65 K and the array at 30 K. It is also essential to ensure that radiation emitted from warm (room temperature) surfaces in the dome, including the telescope itself, does not reach the detector array. The importance of excluding flux from the telescope surroundings can be seen if we compare the background flux which would enter the instrument due to thermal emission from the surroundings with the background flux from the region of sky being

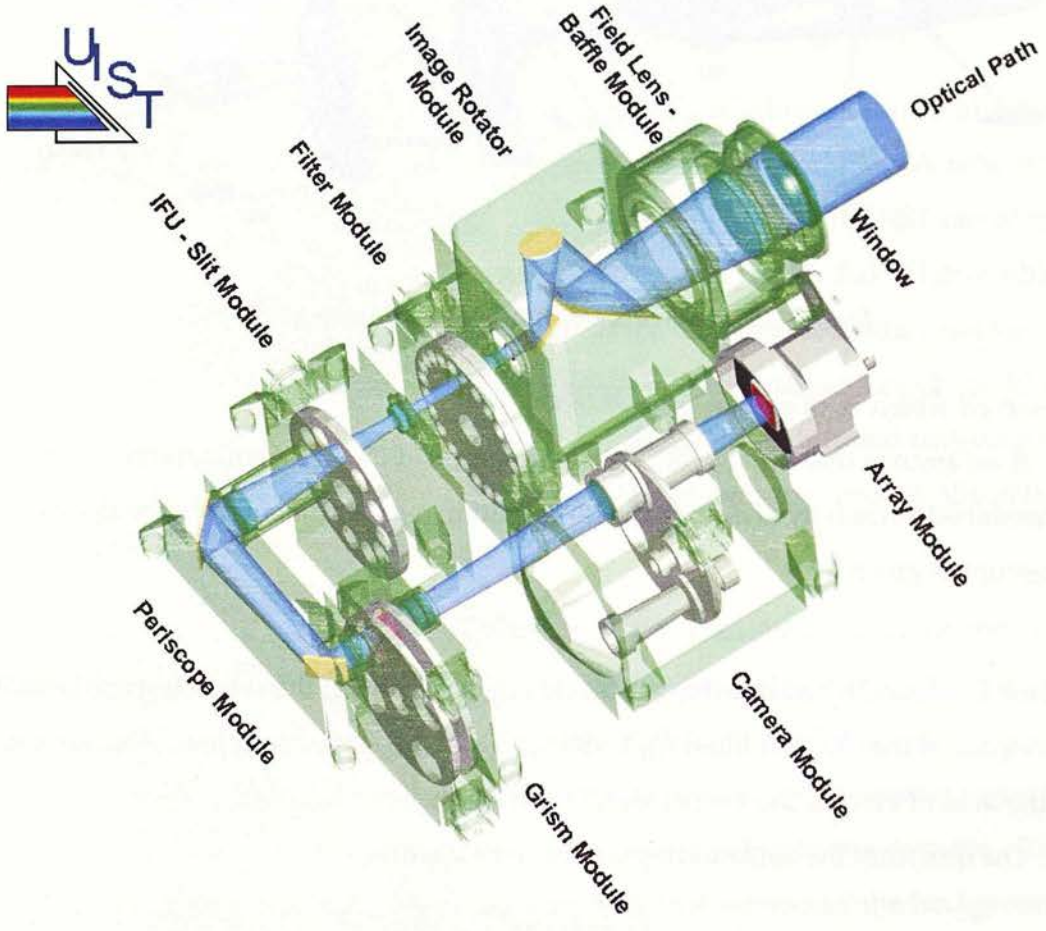

Figure 2.1: An overview of the optical and mechanical layout of UIST

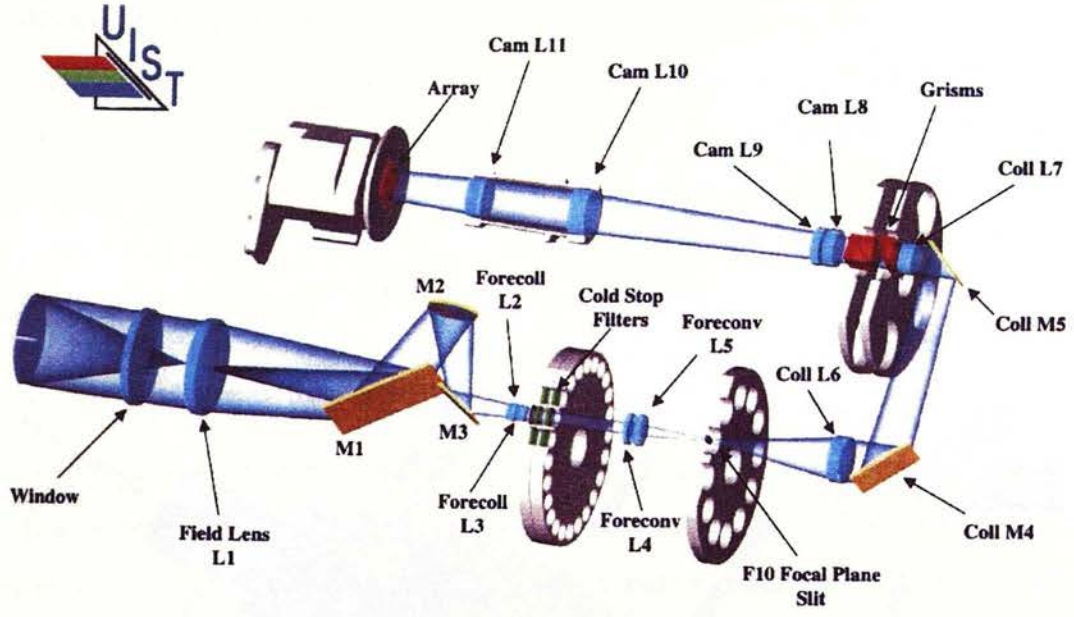

Figure 2.2: An overview of the optical layout of UIST.

observed which is, of course, unavoidable.

If we assume that the sky and the telescope are at the same temperature, and have a combined emissivity of ϵ_1 then the flux entering the instrument from the sky and the telescope is given by

$$F_1 = k\epsilon_1 \pi r_{\text{tel}}^2 \phi$$

where k is found by integrating the blackbody spectrum of the sky/telescope over the bandpass of the selected filter, r_{tel} is the radius of the telescope primary mirror and ϕ is the field of view of the instrument (in steradians).

The flux from the surroundings of the instrument is

$$F_2 = k\epsilon_2 \pi r_{\text{window}}^2 2\pi$$

where ϵ_2 is the emissivity of the surroundings.

For UIST and UKIRT $r_{\text{tel}} = 1.9$ m, $r_{\text{window}} = 0.06$ m and $\phi = 3.4 \times 10^{-7}$ steradian. If we assume that the sky, telescope and surroundings are all at the same temperature, and that $\epsilon_1 = 0.1$ and $\epsilon_2 = 1.0$ then $F_1/F_2 = 180000$. This light must be either reflected out of the cryostat or absorbed by surfaces within the cryostat.

In telescopes designed purely for use at optical wavelengths the primary mirror may act as the stop in order to make full use of the whole surface of the expensive

primary mirror. The instrument sees light coming from the primary mirror which is surrounded by the dark telescope structure and dome floor. In the infrared, however, the instrument would see light from the sky reflected in the primary mirror and thermal emission from the telescope structure and the inside of the dome. In telescopes designed to operate at infrared wavelengths (including UKIRT) the secondary mirror is used to define the aperture stop of the system. The instrument receives light reflected from the secondary mirror (which must all have been reflected from the sky by the oversized primary mirror) which is surrounded by the dark night sky.

Light enters UIST from the telescope through a CaF_2 window as shown in figure 2.2. The image from the telescope is formed just inside this window. A reflective baffle is used to reflect light outside the 2×2 arcmin field of view of UIST out of the instrument. A collimator consisting of a ZnSe field lens (L1) and a BaF_2/LiF doublet (L2, L3) is used to form a pupil image (an image of the telescope secondary mirror) at a cold aperture stop and to produce a collimated beam which passes though the filter wheels. A cold stop is an important feature in the design of all infrared instruments to ensure that only light from the telescope can reach the detector array by absorbing thermal radiation from the surroundings.

It is also essential to filter the light before it reaches the detector because the flux of thermal radiation from the sky is very large at the longest wavelengths that the detector is sensitive to (5 μm). If even a fairly small fraction of this light reached the detector when observing at shorter wavelengths it would significantly increase the background noise in the observations, and possibly saturate the detector. The importance of filtering the light effectively can be seen if we model the background radiation as a black-body spectrum at a temperature of 273 K (valid for wavelengths greater than $\sim$ 2 μm, at shorter wavelengths the background is dominated by OH line emission from the atmosphere). If we assume, for example, that we are using a filter which transmits all light at wavelengths of 2.0–2.5 μm and a fraction, f, of light outside this band and within the range 1–5 μm, then to ensure that the background from outside the 2.0–2.5 μm band is insignificant compared to the background within the band we must make sure that $f \ll 2 \times 10^{-4}$. For this reason it is also necessary to prevent unfiltered light, which is scattered from optical surfaces before it reaches

the filter wheels, from reaching the detector. The inside of the radiation shield which covers the optical bench is painted with infrared black. There are gaps of $\sim$ 1 mm between the front reflective baffle and the front of the image rotator module (which contains the field lens, L1) and between the back of the image rotator and the lens barrel attached to the filter wheel. These gaps are closed using collars sprung against a flat surface on the adjacent module to form a light tight seal. Two concentric black tubes are used to prevent light reaching the array without passing through the camera. One is fixed to the front of the array housing, the other to the back of the camera module. The concentric tubes allow the movement of the array housing by the focus mechanism.

2.1.2 Imaging

Imaging can be carried out at two plate scales: 0.12 arcsec/pixel over a 2×2 arcmin field or 0.06 arcsec/pixel over a 1×1 arcmin field. The camera consists of two doublets (L8/9 and L10/11 on figure 2.2). The plate scale is selected by rotating the camera wheel. This contains four alternative L10/11 doublets: one which is used for 0.12 arcsec/pixel imaging and all spectroscopy modes, one used for 0.06 arcsec/pixel imaging in I, J and M bands, one used for 0.06 arcsec/pixel imaging in H, K and L bands and a pupil imaging camera. The two 0.06 arcsec/pixel cameras are needed for different wavelengths in order to keep the range of travel required of the focus mechanism sufficiently small to allow re-use of the focus mechanism design used in GMOS. To switch to imaging mode the appropriate camera is selected, both grism wheels are moved to the 'open' position, a filter is selected and the image rotator is moved to the low end of its range of travel so that the square field of view is not rotated with respect to the square array. A range of broad and narrow-band filters are available.

2.1.3 Spectroscopy

The image rotator

The first module reached by the light entering UIST from the telescope is the image rotator, which is located between the two elements of the collimator used to produce a collimated beam to pass though the filter wheel. The image rotator is used in spec-

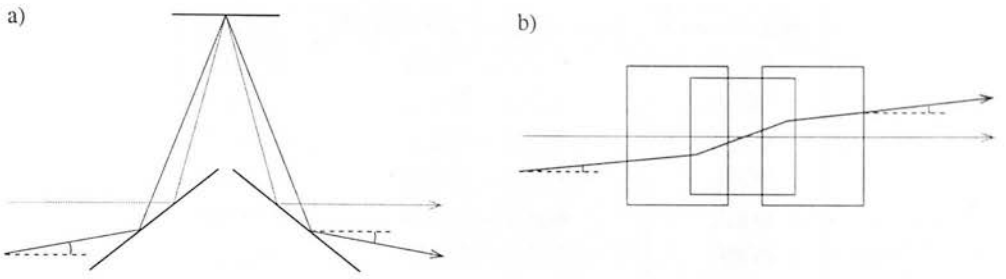

Figure 2.3: When viewed from the side (a) the image rotator inverts the angle between off-axis rays and the optical axis, but when viewed from above (b) off-axis rays are undeviated, emerging parallel to the input ray. The effect of the image rotator is to flip the output image about the plane parallel to the paper in (b).

troscopy modes to rotate the image before it is focused onto the slit so that the angle of the slit on the sky can be selected. It consists of three flat gold-coated mirrors which rotate as a single block about the optical axis.

Figure 2.3 shows that one component of the angle between a ray and the optical axis is inverted by the image rotator, and the component perpendicular to this is not. The effect of the image rotator is, therefore, to 'flip' the image about an axis defined by the angle of the image rotator. As shown in figure 2.4 this produces a rotation in the final image of 2θ when the image rotator is rotated by an angle θ.

There is a square baffle mounted on the input side of the image rotator. The image of this baffle rotates with the image rotator, rotating through the same angle as the image rotator. This vignettes the corners of the 2×2 arcmin field, but does not vignette the slit, which passes through the centre of the field of view.

Grisms

Spectroscopy is carried out using grisms, as described in chapter 1. The UIST grism set includes grisms covering all spectral bands in the 1–5 μm range at spectral resolutions of 1000–4000 using the two pixel slit. The available grisms are listed in table 2.1. The higher resolution grisms enable observations to be made between the closely packed atmospheric OH lines which form the majority of the background emission in the J, H and K [Martini and DePoy, 2000]. Even when the background is dominated by continuum emission the sensitivity is increased by increasing the spectral resolution

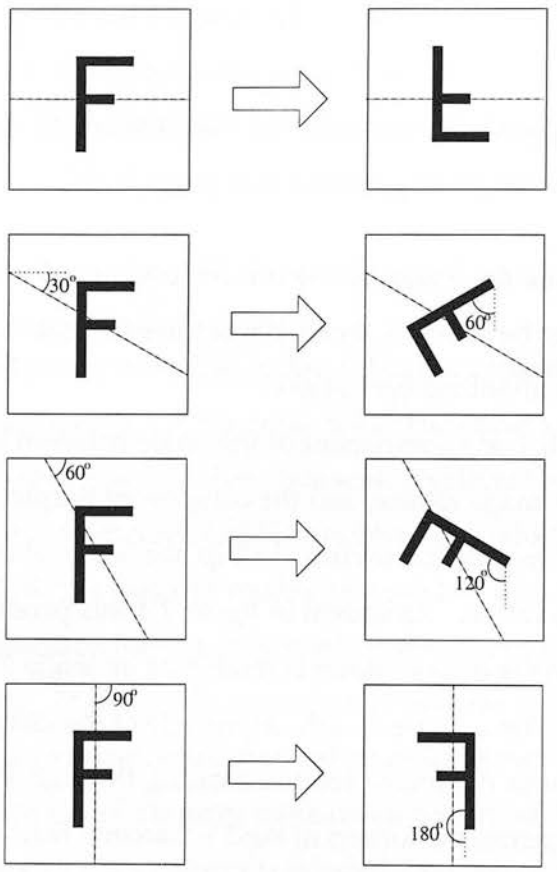

Figure 2.4: The image rotator flips the image about an axis defined by the angle of the image rotator. Rotating by θ the axis about which an image is flipped causes the flipped image to rotate by 2θ.

Grism	Wavelength range /μm	Resolution
short *J*	1.024 – 1.177	3000
Long *J*	1.162 – 1.315	4100
Short *H*	1.423 – 1.625	3800
Long *H*	1.603 – 1.803	4000
Short *K*	2.007 – 2.260	3600
Long *K*	2.204 – 2.513	3800
Short *L*	2.905 – 3.638	1300
Long *L*	3.620 – 4.232	2300
IJ	0.797 – 1.370	950
HK	1.395 – 2.506	900
KL	2.229 – 2.987	1400
M	4.382 – 5.314	2000

Table 2.1: The UIST grism set. The resolution quoted is that obtained at the centre of the wavelength range using the 2 pixel slit.

because the same background flux is spread across more pixels, reducing the flux in each pixel. If unresolved emission lines are to be observed then the signal detected on each pixel is unchanged by increasing the spectral resolution, so the signal to noise ratio is increased in proportion to the spectral resolution. Lower resolution grisms, such as the *HK* grism obviously have the advantage of a broad wavelength coverage, allowing measurements of a large number of spectral lines simultaneously.

Slits

A selection of slit widths is available. The narrowest is just 0.12 arcsec wide on the sky, corresponding to one pixel on the array. The narrowest slit which is routinely used is two pixels wide on the array, giving the highest possible spectral resolution fully-sampled spectrum. This slit is still only 0.24 arcsec wide on the sky, so if point sources are to be observed in average or poor seeing much of the flux falls outside the slit and is lost. In such cases a wider slit is generally used, provided that a reduction in spectral resolution is acceptable. Slits with widths of 4 pixels (0.48 arcsec), 5 pixels (0.60 arcsec) and 7 pixels (0.84 arcsec) are available. When observing extended sources the seeing does not affect the transmitted flux, so there is a simple trade-off between transmitted flux and spectral resolution.

Acquiring targets for observation

One advantage of a combined imager and spectrometer is that imaging mode may be used to acquire targets far more quickly than the traditional method of 'peaking-up' on the target (shifting the slit in small steps across the source looking for the maximum flux). Instead, the slit and grism can be removed from the beam, with the image rotator, camera wheel and filter wheel in the positions in which they will be used for the spectroscopic observations and an image can be obtained. The corners of the image may be vignetted by the image rotator as described above, but for the purposes of acquiring a target this is not a problem. The position of the slit image on the array is known, so all that is required is to offset the telescope to shift the source to the correct position on the array then replace the slit and grism in the beam. This is made possible by the repeatability of the positioning of the UIST slits, which is accurate to ~ 0.1 pixel.

This method of acquisition is particularly helpful with sources which cannot be used for peaking-up, either because they are too faint or because they are extended. The standard technique for observing such sources with CGS 4 was to peak-up on a nearby bright star then offset to the target. This requires an accurate measurement of the offset between the bright star and the desired slit position. Acquiring sources by imaging allows spectroscopy of objects for which accurate astrometry is unavailable and gives the observer more confidence that they know where the slit is positioned on an extended source.

2.1.4 Polarimetry

Polarimetry observations can be carried out by inserting an IRPOL2 waveplate into the beam from the telescope and a Wollaston prism which is mounted in one of the grism wheels.

A Wollaston prism is manufactured from a birefringent material. Such materials have different refractive indices for the components of light polarised parallel to different principal axes. The effect of such a material is to split a beam into two beams according to polarisation. In a Wollaston prism (figure 2.5) the principal axes in the two halves of the prism are rotated by 90° around the optical axis relative to one an-

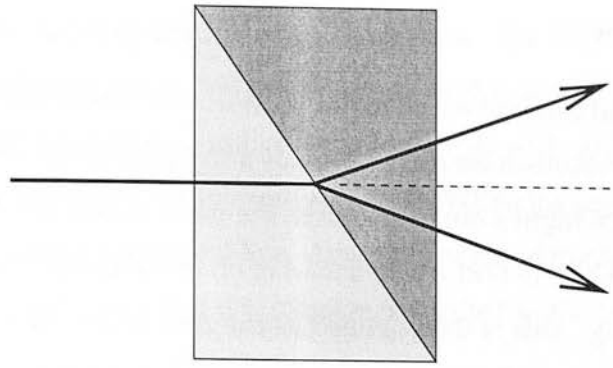

Figure 2.5: A Wollaston prism is used for polarimetry. This consists of two triangular prisms manufactured from the same birefringent material.

other. Neither beam is refracted on entering the prism perpendicular to the surface. At the boundary between the two halves the light of one polarization is passing from a material of lower refractive index to one of higher refractive index, and the reverse is true for light of the other polarization. The two polarisation components are therefore refracted in opposite directions.

The IRPOL2 waveplates (there are several for use at different wavelengths) consist of a disc of birefringent material with a thickness selected so that the phase of light polarised parallel to the fast axis of the waveplate is shifted by half a wavelength relative to light polarised perpendicular to the fast axis. This has the effect of rotating the angle of polarisation of the light. A polarimetry observation involves taking a series of frames each containing the two beams produced by the Wollaston prism and rotating the waveplate between each observation. The maximum difference in intensity between the two beams and the angle of the waveplate for which this is found gives a measurement of the degree and direction of polarisation of the light.

The Wollaston prism produces an offset between the two beams of 166 pixels in the *H*-band, corresponding to 20 arcsec on the sky. In order to prevent the two beams overlapping a mask is inserted using the slit wheel. For imaging polarimetry this consists of two 20 arcsec (E-W) $\times$ 120 arcsec (N-S) slots with sufficient separation to prevent the images overlapping. Spectropolarimetry can also be carried out using a mask consisting of two slits each 20 arcsec long. Not all of the grisms are available for polarimetry because the Wollaston prism is mounted in one of the grism wheels.

2.1.5 Mechanisms

The filters, grisms and cameras are all mounted in wheels. These wheels and the image rotator and focus mechanism are each driven by a stepping motor via a worm gear. At the beginning of each night's observing all of the mechanisms are datumed. This involves rotating the wheel to find where a marker on the wheel switches a microswitch on the wheel housing. This is then defined as the zero point. All other positions on the wheel are then given as the number of steps required to offset from this point.

Calibrating the mechanisms

Accurate calibration of the position of each slit and each grism was necessary. A small error, $\Delta\theta$, in the positioning of the slit wheel would rotate each spectral line by $\Delta\theta$ around its centre (the slits are tangential to the rotation of the wheel, so the position of the centre would not move for small errors in positioning). This would produce an offset between the wavelength calibration of the top and bottom of the array. Similarly, a small error in the positioning of a grism would rotate the dispersion axis. This would most clearly be seen in the spectrum from a point source with a continuum spectrum, which would no longer form a horizontal line across the array, but a line rotated by the same angle as the grism.

To calibrate the positions (in steps from the datum) of each slit in the wheel a frame was observed with the slit and a filter in the beam but no grism. Two rows of the image were extracted, one from near the top and one from near the bottom of the array, separated by a distance Δy. The horizontal position of the slit image in each of these two cross-sections was measured by fitting a Gaussian profile to the image, giving a measurement of the difference in horizontal position, Δx. From this the error on the positioning of the wheel could be calculated:

$$\Delta\theta = \tan^{-1}\left(\frac{\Delta x}{\Delta y}\right)$$

which, knowing the number of steps in one complete rotation of the wheel, N, could be converted into an offset in steps:

$$\Delta n = \frac{\Delta\theta}{360^\circ} \times N.$$

A similar procedure was used to align the grisms. The UIST slit wheel contains a number of pinholes for use in engineering tests of this sort in addition to the slits and apertures used for astronomical observations. For each grism a spectrum of a continuum source was observed through a pinhole. When the grism is correctly positioned this should give a horizontal line. Again the angle of the line on the array was measured, converted to steps and this offset was applied to the position of the grism wheel.

The positions of the slit image or dispersed pinhole could be measured to ~ 0.1 pixel. This corresponds to an angle of 0.008°, or 2 steps on the wheel (total number of steps for one rotation is 88000 for the slit wheel and 96000 for the grism wheel). This is comparable to the accuracy to which the wheels can repeatably be positioned. The accuracy to which the grism wheel can be positioned allows us to assume that the dispersion axis is parallel to the rows of pixels on the array, and hence that a single row extracted from a spectrum is the spectrum from a single spatial pixel along the slit. This reduces the need for resampling of the spectra prior to analysis. The repeatability of positioning the slit wheel allows the acquisition of targets for spectroscopy using imaging mode as described in section 2.1.3, which is only possible because we know where the slit image falls on the array to sub-pixel accuracy.

2.2 The Integral Field Unit

The UIST Integral Field Unit (IFU) is an image slicer, as described in chapter 1. The design of the UIST IFU was described in detail by Wells et al. [2000]. A schematic view of the IFU is shown in figure 2.6 and photographs of the IFU alone and attached to the UIST slit wheel are shown in figures 2.7 and 2.8. When the IFU is deployed the triple fold mirror is moved into the beam, diverting the focus which would normally be formed at the slit plane to fall just before the 'f-conversion mirror'. This is a small concave spherical mirror which changes the beam from a focal ratio of f/10 to f/220. This beam is reflected off the second face of the triple fold mirror producing an image on the slicing mirrors which is magnified by a factor of 22. This magnification allows the slices to be a comparatively manageable 0.9 mm wide rather than 0.04 mm, the width of the 2 pixel slit which is the same width on the sky as a single slice of the IFU.

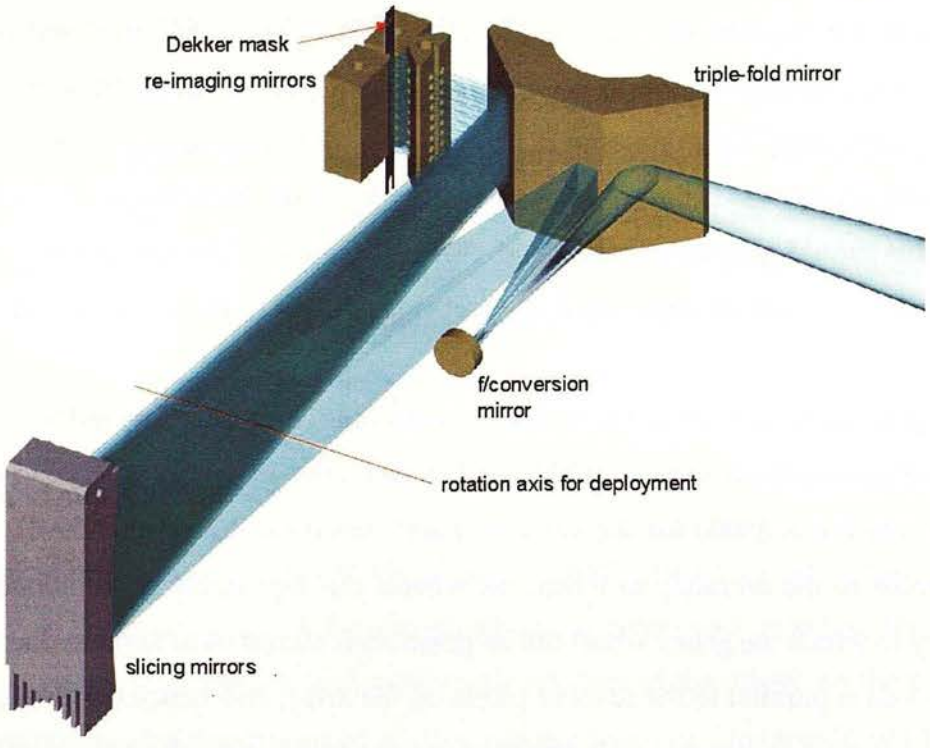

Figure 2.6: The optical layout of the UIST IFU.

The slices are required to be this narrow (0.24 arcsec on the sky) so that the spatial resolution is sufficient to sample the PSF under average seeing conditions. An image of the input pupil is also formed close to the f-conversion mirror.

The slicing mirrors are all part of a common spherical surface but each slice is tilted by a different angle about an axis parallel to the short dimension of the slice. A single spherical mirror at the slicing plane would simply re-image the pupil image, as shown in figure 2.9 (the triple fold mirror has been removed from these diagrams for clarity). The different tilts on each slice shift the positions of the re-imaged pupils parallel to the slices, producing 18 separate re-imaged pupils, each containing light from a single slice of the field of view. Half of the slices are also tilted around an axis parallel to the long dimension of the slices, producing two columns of pupil images.

A set of 18 re-imaging mirrors are used to produce simultaneously a de-magnified image of the slices and re-image each of the 18 pupils to produce a single output pupil which is identical to that which would be seen by the optics following the slit plane if the IFU was not used (figure 2.10). The two columns of pupil images are required

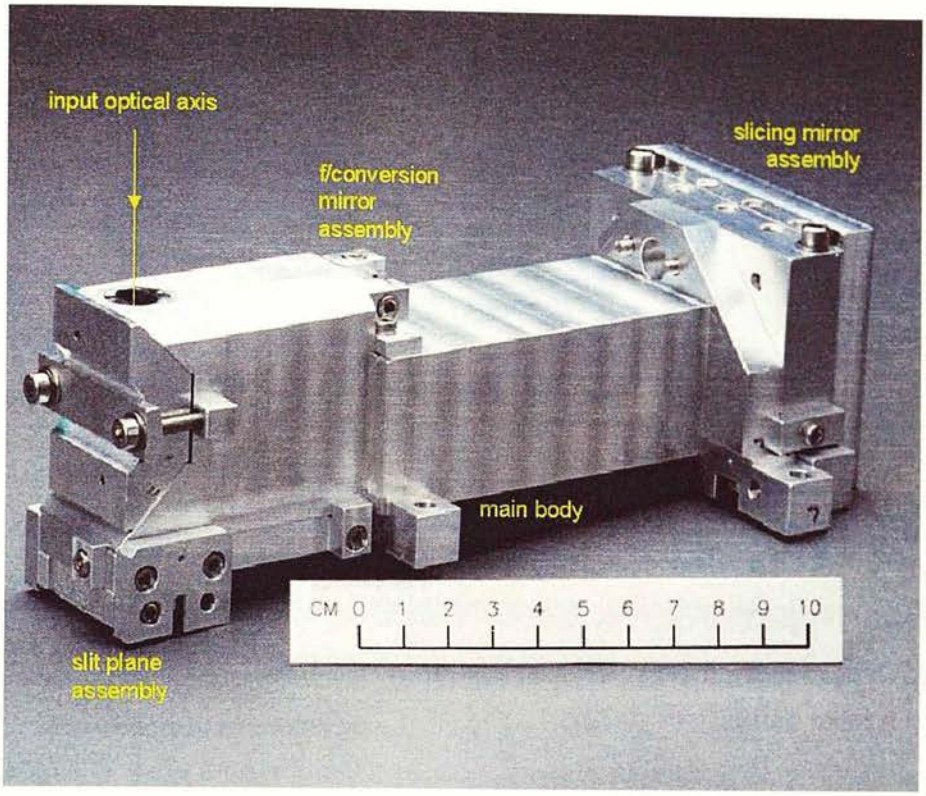

Figure 2.7: A photograph of the UIST IFU.

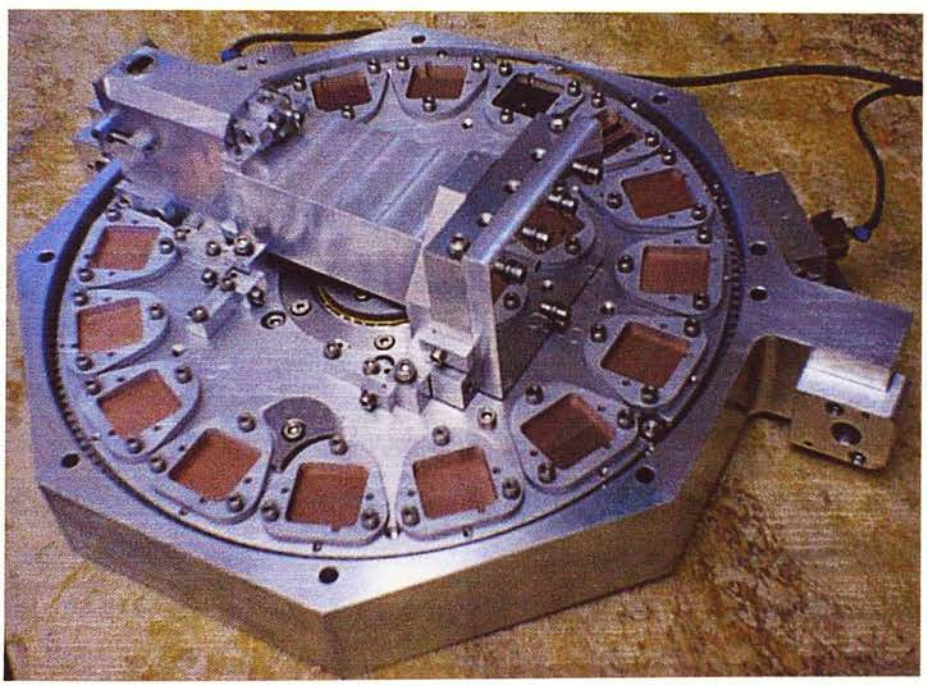

Figure 2.8: The UIST IFU mounted on the slit wheel.

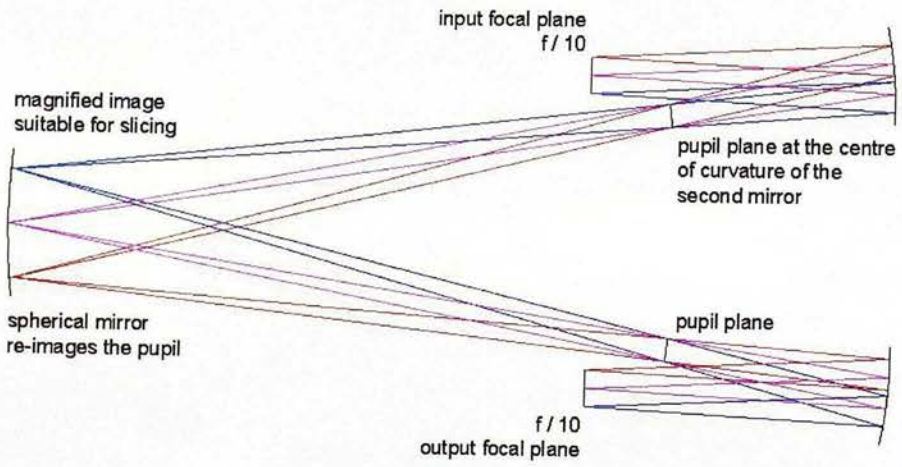

Figure 2.9: If a simple spherical mirror was placed at the slicing plane of the IFU it would form an image of the pupil and the focal plane (not to scale, and the triple fold mirror has been omitted for clarity).

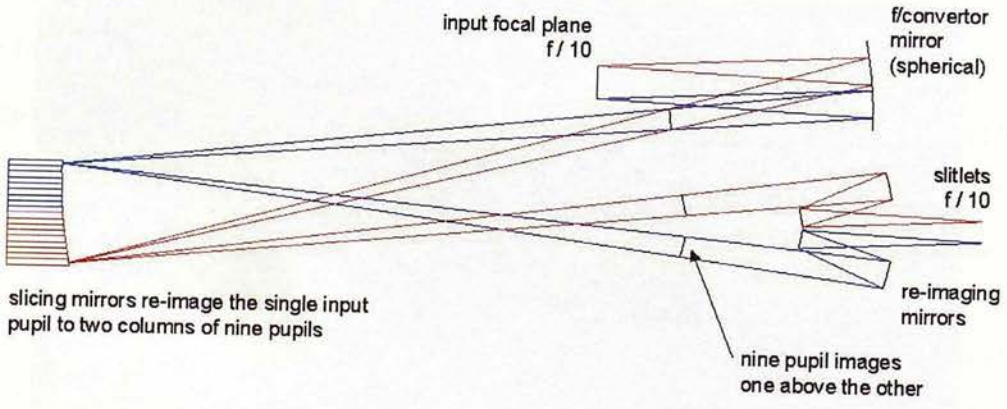

Figure 2.10: The slicing mirrors form two columns of nine pupil images, each containing light from one slice on the sky. The reimaging mirrors form two sets of nine demagnified slice images, which are folded to form two columns of slice images in a single focal plane by a pair of flat fold mirrors.

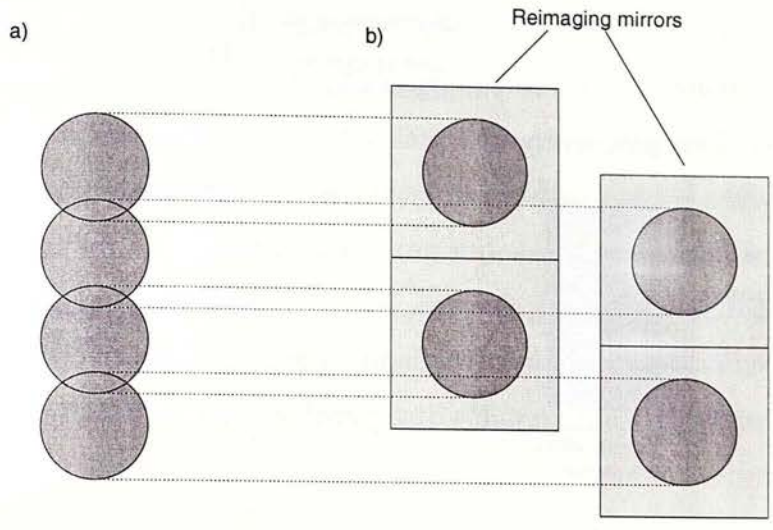

Figure 2.11: The reimaging mirrors are not at the pupil plane in the UIST IFU. If the output beams from all slices of the slices were arranged in one column they would overlap at the reimaging mirrors (a). Forming a staggered arrangement allows the use of oversized re-imaging mirrors (b).

because, unlike the design proposed by Content [1997], the re-imaging mirrors are not at the pupil plane, so if a single column of pupil images were formed they would overlap with one another (figure 2.11), or else the space between them would need to be increased which would then increase the space between the slice images at the output, making inefficient use of the detector array. Each of the images formed by the re-imaging mirrors is actually an image of all 18 slices, but light from the sky can only be seen in one slice in each image. A final flat fold mirror is used to produce two columns of slice images at the output plane of the IFU. The order in which these slice images are mapped to the field of view are shown in figure 2.12. The output focal plane of the IFU was designed to be in the same plane as the slits on the slit wheel. In practice an offset of $\sim$ 0.5 mm was found between the two focus positions. This was compensated for by finding the optimum position of the focus mechanism with each grism both for the slit and for the IFU. The ORAC-OT software automatically selects the correct position of the focus mechanism to be used.

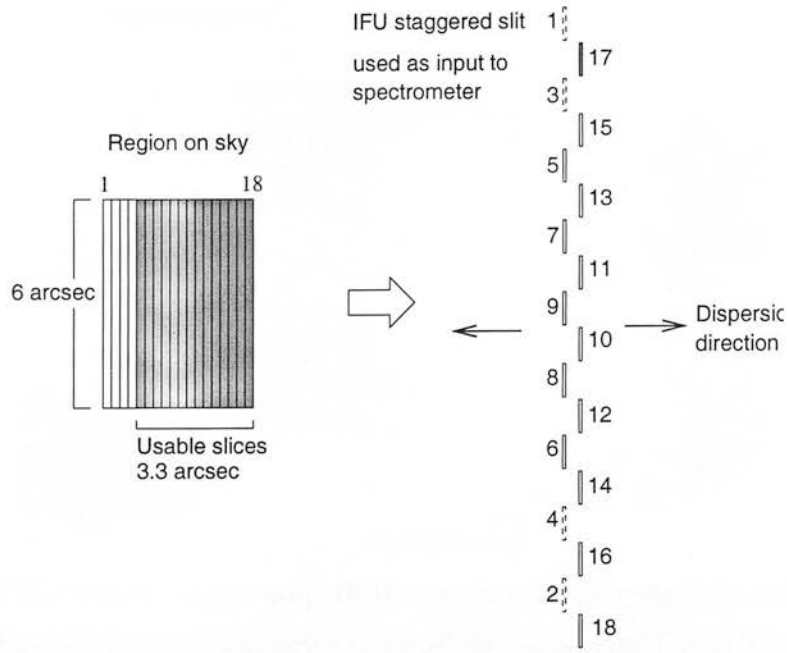

Figure 2.12: The order in which the slices of the field of view appear at the output of the IFU.

2.3 Manufacture of the powered mirrors

The process for making the slicing mirrors of the IFU was one of the crucial concepts in turning it from an idea to a working device. The mirror substrates were manufactured at the UK Astronomy Technology Centre. Each substrate was made as a rectangular slab of 6061 aluminium alloy. Each substrate was a different length and had an arc cut out of one edge to reduce the amount of material to be removed in the diamond-machining of the optical surface.

The optical surface on the slicing mirrors was machined by Precision Optical Engineering Ltd. with all eighteen substrates clamped together in a fixture (figure 2.13) [Wells et al., 2000]. A central spacer split the mirrors into two groups of nine and the two outer mirrors were flanked by sacrificial pieces to prevent damage to the edges of the mirrors during machining. The mirrors were held in a fixture which was closely based on the final mounting which would be used in UIST. The substrates were placed in the fixture with all the ends of the substrates aligned against an end wall in the fixture. The different lengths of the substrates were calculated so that if a common spherical surface were cut when one end of the substrates were aligned then the necessary

tilts of the mirrors would be produced by longitudinal displacement of the mirrors when the other ends were all aligned. This meant that the tilt of the mirrors, a critical part of the design, was produced by dividing a length, which could be easily measured and carefully controlled, by the radius of curvature of the mirror which was made very accurately by diamond machining and was several times bigger than the largest physical dimension of the substrate. Removing the central spacer and moving the two blocks of nine mirrors together tilted nine of the mirrors relative to the others in the perpendicular direction, producing two columns of slice images at the output focal plane.

The accuracy required was found by considering the effect of a lateral offset of the slicing mirrors on the pupil images following the slicing plane. In order to maintain the throughput of the IFU all of these pupils must be superimposed to form a single output pupil. A lateral offset of 10 μm of one of the slicing mirrors is equivalent to a tilt of 0.05 milliradian. At the pupil plane following the slicer this would give an offset of the pupil images of 20 μm, or 2.5% of the pupil diameter. A tolerance of of ± 10 μm was therefore set on the lengths of the slices.

The design of the clamping fixture was flawed: the arrangement of the moving jaw should not have been made similar to that in the IFU itself (which needed to be compact) but should have been much more like a miniature version of a conventional machine vice. At some point before, or during, machining, the moving jaw lifted slightly and the adjacent four substrates tilted slightly about their long axis. This was enough to displace the optical beams from these mirrors so that they no longer fell on their re-imaging mirrors and did not produce a slitlet at the output focal plane. The four missing slitlets were images of a contiguous piece of sky because the four faulty slicing mirrors were adjacent to one another. The decision was made that the IFU should be delivered with a reduced field-of-view (6.0×3.4 arcsec – 78% of the original) rather than to delay the project or incur the costs of designing and making a new machining fixture.

The machining of the re-imaging mirrors used basically the same principle but differed in detail. The mirrors were machined as pairs using nine similar fixtures. The optical surface and the mounting surface were cut in the same operation. The fixtures

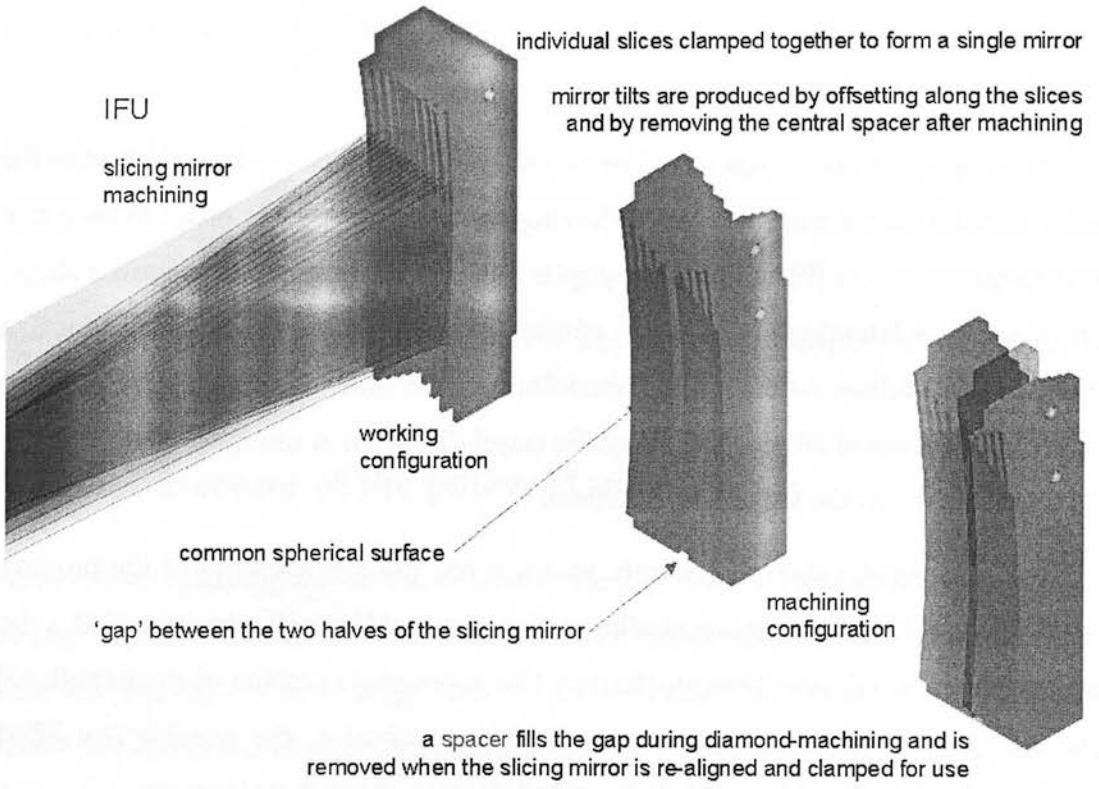

Figure 2.13: The slicing mirrors were clamped together as a single block for machining (right). The central spacer was removed and the slices were shifted along their length to the working configuration of the (left).

were sufficiently similar that they had to be individually numbered, as were the mirror blanks. The alignment of the mirrors in their final mounts was again made by aligning one end of them against a reference surface.

The simplest of the powered mirrors was that used to convert the incoming f/10 beam to the f/220 at the slicing mirrors. It was cut as a simple spherical surface in the end of a cylindrical substrate of 9 mm diameter. The optical surface, the mounting surface and the outside diameter were all diamond-turned at a single setting and therefore had a known, and highly accurate, relationship with each other. The optical surface that was used was to one side of the centre of the mirror thereby avoiding the slight roughness which occurs at the middle of the curve. Although in the event it was not necessary, the tilt of the mirror could have been adjusted by a lateral displacement of the mirror, again taking advantage of the fact that the radius of curvature of the mirrors was larger than any of its physical dimensions.

2.4 Testing the mirrors

Each of the 9 pairs of re-imaging mirrors and the f-conversion mirror was tested using a Twyman-Green interferometer. This allowed us to measure both deviations from a perfect spherical surface and the radius of curvature of the mirror. The input beam is split with a semi-silvered mirror as shown in figure 2.14. One beam is reflected off the mirror being tested, and is then recombined with the other beam to give interference fringes on the CCD.

To measure the deviation of a mirror from a perfect spherical surface the interferometer is first set up as shown in figure 2.14(a) with a reference mirror, which is known to have a very accurate spherical surface. The centre of curvature of the mirror is placed at the focus of the interferometer so that any given ray of light is returned along its own path. The intensity at each point on the CCD depends on the path difference between the light reflected from a single point on the test mirror and the light reflected from the flat mirror within the interferometer. The fringe pattern seen when the reference mirror was tested is then stored and the reference mirror was replaced by the mirror to be tested which is again positioned with the centre of curvature at the focus of the interferometer. The fringes seen with the reference mirror are then

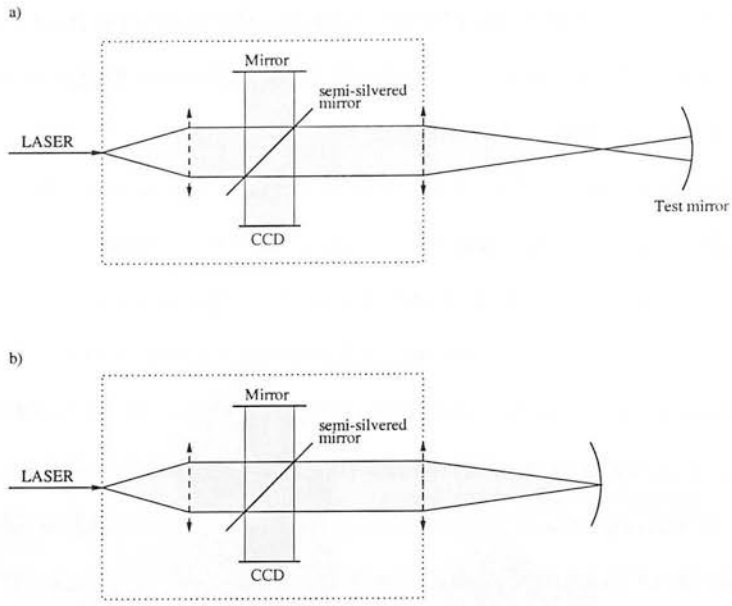

Figure 2.14: A Twyman-Green interferometer was used to test the mirrors. When used to measure the shape of a spherical mirror it is used in the configuration shown in (a), with the centre of curvature of the mirror at the focus of the interferometer, so any given ray of light is reflected back along its own path. When the focus is placed on the surface of the mirror (of any shape) as shown in (b) each ray is returned along the opposite path.

subtracted from those seen with this mirror in order to remove path differences due to imperfections in the optics of the interferometer. If the surface were perfectly spherical then all rays reflected from the mirror would have travelled the same distance, so the intensity at the CCD should be uniform. The CCD is read by a desktop PC with software for turning the images of interference fringes into measurements of the surface of the mirror.

The interferometer can be moved using three perpendicular micrometers. This makes it possible to measure the radius of curvature of a mirror. The interferometer is positioned as in figure 2.14(a) by moving it to minimize the deviation of the mirror surface from a sphere with its centre at the focus of the interferometer. The interferometer is moved forward until the focus is on the mirror, as shown in figure 2.14(b), when the interference pattern should be uniform. The distance moved can then be read off the micrometers. This measurement can be made to an accuracy of a few microns.

Mirror pair	Measured radius /mm	Designed radius /mm
4	15.714	15.718
6	15.715	15.719
7	15.699	15.696
8	15.820	15.828
9	16.055	16.058

Table 2.2: After re-machining the radii of curvature of a sample of the reimaging mirrors were measured to an accuracy of $\sim$ 2 μm. The tolerance on the radii was 5 μm.

When the re-imaging mirrors were tested in this way the surface quality was found to be within tolerance, but they were found to have been manufactured with the radii of curvature specified, but not on the correct substrates, for example reimaging mirror 3 had been given the radius of curvature specified for reimaging mirror 7. These mirrors were therefore returned for re-machining. After re-machining a sample of the mirrors were measured again to check the measurements returned with the mirrors by Precision Optical Engineering, who machined the optical surfaces. The results of these measurements are shown in table 2.2. The r.m.s. deviation from a spherical surface was found to be 10 nm, well within the 20 nm specification. The f-conversion mirror and the slicing mirrors were also tested in this way and were found to be within tolerance.

2.5 Aligning the components of the IFU

The optical components of the IFU are mounted on the IFU housing within three movable blocks – the f-conversion mirror assembly, the slicing mirror assembly and the slit-plane assembly – visible in figure 2.7. All optical components are positioned by permanent and repeatable means, using principles which are used on a larger scale in the rest of UIST, and have been successfully applied in other instruments from the UK ATC, including CGS4 [Ramsay Howat et al., 1994]. The alignment is carried out at room temperature using standard optical equipment. The alignment is maintained when the instrument is cooled due to the all aluminium construction.

Corrections to the positions and alignments are made by selective machining of blocks against which the optical components are located. The design of the blocks is such that the optical component can be moved in either direction in the two dimensions perpendicular to the optical axis by removal of material from the block. All non-flat optical surfaces are spherical, so tilts can be corrected by translation in this plane. This is easier and more accurate than trying to tilt the components because the radius of curvature of the mirrors, which is the effective lever arm of these corrections, is in all cases significantly larger than the physical dimensions of the component. No alignment was carried out parallel to the optical axis because the tolerances on the positions of the mirrors along the optical axis were significantly larger than the manufacturing accuracy of the IFU housing. The eighteen slicing mirrors are clamped in a single mount, as are the 18 re-imaging mirrors. These assemblies were then aligned to give the best overall performance. No attempt was made to align the individual slicing mirrors or re-imaging mirrors.

2.5.1 Defining the optical axis

Much of the alignment, both of the components of the IFU and of the rest of UIST, was carried out using a micro-alignment telescope. This is a telescope mounted on a rigid support with cross-wires in the eye piece and micrometers to shift the telescope horizontally and vertically allowing the distance between a target and the optical axis to be measured. The first stage of alignment is to define the optical axis. This is done either using two targets or one target and a surface perpendicular to the optical axis. Once the telescope has been aligned to the targets the telescope is used to define the optical axis.

If the optical axis is defined by two targets then the telescope is first approximately lined up with the targets by eye. The telescope is then shifted horizontally and vertically in order to get the nearer target on axis. The telescope is then tilted horizontally and vertically to get the more distant target on axis. Each time this procedure is repeated the alignment of the telescope converges with the axis defined by the targets. A similar procedure is used if the axis is defined by one target and a perpendicular surface. A light source is added to the telescope which illuminates a glass plate on the

front of the telescope marked with concentric circles. The telescope can be focused to produce an image of this glass plate reflected in the perpendicular surface. The distance between the centre of the circles and the cross-wires can be used to calculate the angle between the telescope and the reflecting surface. The telescope is tilted to bring the reflection on axis and shifted to bring the target on axis.

2.5.2 Aligning the f-conversion mirror

First the f-conversion mirror was aligned so that an on-axis image would appear at the centre of the slicing mirrors. In order to do this it was necessary to define the optical axis. The image-plane assembly and the fold mirror were removed, allowing light to pass undeviated through the IFU housing. An alignment telescope was set up to define the optical axis using a target at the centre of the input of the IFU, consisting of a brass disc which precisely fitted the entrance aperture of the IFU with a pinhole drilled in the centre. This marked the position of the optical axis. A mirror held against the rear surface of the IFU housing defined the tilt. The fold-mirror was then put back in place, taking care not to disturb the position of the IFU housing, and the slicing mirrors were removed and replaced by a target with a pinhole marking the centre of the slicing area. The alignment telescope was used to measure the offset of the image of the target from the optical axis. The requirement on the accuracy of alignment of the f-conversion mirror was that the target should be within 50 μm of the optical axis on the demagnified image of the slicing plane (one slice width).

In order to test the repeatability of these measurements the fold mirror was removed and replaced several times, measuring the position of the image each time. The same procedure was carried out removing and replacing the mount containing the the f-conversion mirror from the housing of the IFU and removing and replacing the f-conversion mirror itself from its mount. All of these gave shifts in the position of the image of the target of 10 μm or less – comparable to, or less than, the measurement accuracy possible using the alignment telescope.

Two, supposedly identical, f-conversion mirrors had been manufactured in order to provide a spare. When the first was tested it was found that the offset of the target image changed if the f-conversion mirror was rotated (table 2.3). It was concluded that

First mirror:

Rotation	x-offset	y-offset
0°	-0.11	0.03
90°	0.06	0.12
180°	0.10	0.01
270°	0.00	-0.07
0°	-0.09	0.02

Second mirror:

Rotation	x-offset	y-offset
0°	0.00	0.02
90°	0.01	0.02
180°	0.01	0.02

Table 2.3: The offsets of the target image from the optical axis as a function of the rotation of the f-conversion mirror (relative to an arbitrary start point). Offsets are in mm.

the mirror surface had been machined onto the substrate 100 μm off-centre. The second mirror was found to be correctly centred. The offset of the target image from the optical axis was 20 μm, so no adjustments were required to align it within tolerance.

2.5.3 Aligning the slicing mirrors

The slicing mirror assembly and the pupil mask at the output were put in place. The Twyman-Green interferometer was used as a focused light source and passed though a 41 mm aperture 410 mm before the focus to produce an f/10 beam, mimicking the input to the IFU in UIST. The beam was positioned so that the f-converter mirror re-imaged the focus onto the slicing mirrors. This allowed individual slices to be illuminated by moving the focus across the slices. The pupil images were photographed without the pupil plane mask in place. The mask was then replaced and photographed without moving the IFU or the camera. From this the positions of the pupil images and the holes in the pupil mask were measured and the slicing mirror assembly was shifted in order to centre the pupil images on the holes in the pupil mask. It was found that it was possible to align the slices so that 14 of the 18 pupil images suffered little or no vignetting at the mask. The other four pupils are almost completely vignetted at the mask (figure 2.15) due to the misalignment of the slicing mirrors during machining, as described in section 2.3.

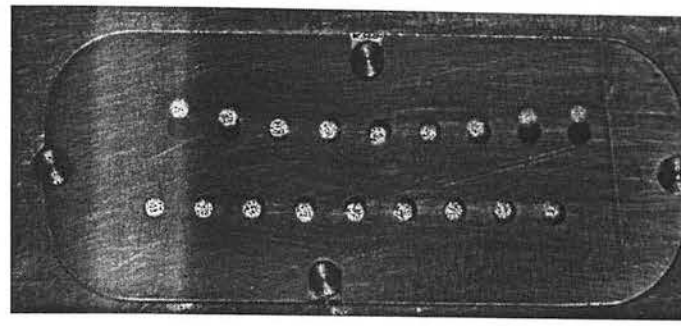

Figure 2.15: A photograph of the 18 pupils produced by the slices of the IFU superposed on a photograph of the pupil plane mask. Four pupil images (two top left and two top right) are not aligned with the holes in the pupil plane mask due to misalignment during manufacture.

2.5.4 Aligning the image-plane assembly

The image-plane assembly was attached to the IFU. Illumination was provided by an unfocused white light passing through a 41 mm aperture 410 mm in front of the focus position in the IFU, reproducing the size and position of the UIST input pupil. A camera lens was used to focus the output from the IFU onto a ground-glass screen which could then be photographed using a CCD camera. Either the slice images or the exit pupil images could be focused onto the screen by changing the distance between the lens and the screen. The 18 exit pupils should all be the same size and at the same position on the screen as the input pupil would be if the IFU were not present. This was checked by removing the IFU and positioning the ground-glass screen so that a focused image of the input pupil (the aperture) was seen on the screen, which was photographed. The IFU was then replaced without moving the illumination, aperture, lens, screen or camera. The 18 superimposed exit pupils were now seen on the screen and photographed. The offset of the output pupil image relative to the input pupil was measured and the position of the image-plane assembly was adjusted by machining the mounting blocks so that the output pupil was aligned to the input pupil.

The relative positions of the individual exit pupil images were examined by stopping down the input aperture to 2 mm, 5% of its original size. This makes the exit pupil images much smaller so that the individual images can be seen. The pupil images from all 14 usable slices were found to have their centres within $\sim$0.1 full-size

Figure 2.16: The slice images at the output of the IFU. Each of the slits in the image-plane mask of the IFU has a 0.5 mm hole in the centre to allow the offset of the slice image from the slit to be measured.

pupil diameters of the centre of the input pupil, so the vignetting of the pupil is negligible.

2.5.5 Aligning the image-plane mask

The slits in the image-plane mask are only 100 μm wide, and must be aligned with the slice images to within $\sim$ 20 μm. This could not be achieved on the bench using the methods used for aligning the other parts of the IFU. A mask was manufactured with the slits in the designed position, in the hope that the slice images would be close enough to their designed positions for the mask to work. This was found not to be the case: only three of the slice images passed through the mask with no vignetting. This mask was then used to let us specify a new mask with each slit individually aligned to the slice image. A circular hole of diameter 0.5 mm was drilled in the centre of each slit. During the following cooldown of UIST, images were taken which showed both the position of the slits and of the slice images (figure 2.16). The positions of the slits were measured and fitted to the designed positions with a universal rotation, scaling and offset. This determined the transformation to obtain the absolute position on the mask in the coordinate system defined on the manufacturing drawing from the pixel coordinates of an image on the array. These transformations were then applied to the positions of the slice images and the offsets between the two were calculated. The maximum offset required was 110 μm and the r.m.s. offset was 65 μm. A new mask was then prepared with the slit positions moved by these offsets which did allow all the slice images to pass through unvignetted.

2.6 Scattered light in the IFU

2.6.1 Absorption and scattering in the IFU

All the optics of the IFU are uncoated, diamond-turned mirrors manufactured from aluminium alloy 6061. Light passing through the IFU undergoes seven reflections, so a significant fraction of the light is lost due to absorption or scattering. Light will also be lost if each of the re-imaged pupils is not aligned with the UIST pupil.

The surface roughness of diamond turned mirrors is not purely random, but is primarily in a periodic, concentric structure. The total integrated scatter, S, is given by

$$S = R(\theta_i)\left(1 - \exp\left[-\left(\cos\theta_i \times 4\pi\sigma/\lambda\right)^2\right]\right) \tag{2.1}$$

where θ_i is the angle of incidence, $R(\theta_i)$ is the reflectivity of the material as a function of θ_i and σ is the r.m.s. surface roughness of the mirror Church and Zavada [1975]. All reflections in the IFU are close to normal incidence, so we can also assume that $\cos\theta_i \approx 1$, and therefore

$$S = R_{\mathrm{Al}}\left(1 - \exp\left[-\left(4\pi\sigma/\lambda\right)^2\right]\right). \tag{2.2}$$

2.6.2 Scattering from the slicing mirrors

There are two sources of scattering from the slicing mirrors: scattering due to surface roughness and scattering from the edges of the slices. Scattering does not broaden the image of the slice at the detector because the light is imaged to the same position irrespective of the angle at which it leaves the slice. Each re-imaging mirror re-images all of the slices unless the Dekker mask is used to prevent this. If there is no scattering then this is not a problem: each re-imaging mirror will image one illuminated slice and 17 dark slices, but if there is scattering then it will image the scattered light from all the slices. This will produce ghost images of bright spectral lines scattered from other slices which will appear offset from the same lines in the desired slice.

Scattering due to surface roughness

The total fraction of light scattered due to the roughness of a diamond turned mirror surface is given by equation 2.2. This scattered light is assumed to scatter uniformly

into a solid angle Ω_0. Any of this scattered light which passes through one of the holes in the pupil mask, each with solid angle Ω_P, will reach the detector. If there is no focal plane mask then the spectrum from each slice will include 17 ghost images from the other slices, offset from one another by one slice width, each with an intensity of α times the intensity of the true spectrum, where

$$\alpha = S \times \frac{\Omega_P}{\Omega_0}.$$

The surface roughness is thought to be $\sigma < 15$ nm. If we assume this worst case scenario, and assume that all of the scattered light is scattered by a small angle, falling within a circle of radius 10mm at the pupil mask for example, then we find that then we find that 3.4% of the light falling on the surface of a slice is scattered, and that 0.25% of this light passes through a given hole of radius 0.5mm in the pupil mask giving a ghost image of $\sim 10^{-4}$ times the intensity of the true image.

Scattering from the edges of the slices

We assume that there is a rough strip of width δ down both edges of each slice of width w which scatters any light falling on it uniformly into solid angle Ω_1. The intensity of the ghost images will therefore be

$$\frac{\Omega_P}{\Omega_1} \times \frac{2\delta}{w}$$

times that of the true image.

If we again assume a worst case scenario with $\delta \approx 20\mu$m and all the scattered light falling in a circle of radius 10mm at the pupil mask then we find again that the ghost image from each slice is $\sim 10^{-4}$ times the intensity of the true image.

The effect on the final spectrum

By assuming a worst case scenario for scattering due to the surface roughness of the mirrors and the edges of the slices we obtain an estimate for the ratio of the intensity of the ghost image from a single slice to the intensity of the true image of $\sim 2 \times 10^{-4}$. In practice the ratio is probably far lower than this. The greatest source of uncertainty is that we do not know the values of Ω_0 or Ω_1 and the ratio depends on the square of the

solid angle into which the light is scattered. If we assume that the light is scattered into a circle of radius 30mm at the pupil mask, which may well still be an under-estimate then the ratio is reduced by an order of magnitude.

The Dekker mask at the image plane is designed to reduce or eliminate these ghost images. If the slits in the mask were the same width as the images of the slices and the slice image fell exactly on the slit then the ghost images would be entirely eliminated. In practice, given that the alignment of the images to the mask is not going to be perfect, the only way of entirely eliminating the ghost images would be to make the slits in the mask narrower than the images of the slices, thus making the images of the slices at the detector less than 2 pixels wide and reducing the intensity of the spectrum. The slit should be slightly wider than the image of the slice to avoid vignetting due to misalignment of the image to the mask. If the slits are 100 μm wide, double the width of the slice image, then each will let through all the unscattered light from one slice and half of the scattered light from the two adjacent slices. This would leave two faint ghost images, one on each side of the true image, offset by a single slice width with intensity less than 5×10^{-5} times the intensity. A ghost image of this strength would be negligible. The profiles of spectral lines observed with the IFU and the 2 pixel slit were examined and no evidence of excess emission was found in the wings of the lines from the IFU.

2.6.3 Transmission of the IFU

The IFU contains masks at both pupil and image planes, so we can assume that virtually all scattered light from any of the mirrors is lost. The reflectivity of the ith mirror of the IFU is given by

$$R_i = R_{\mathrm{Al}} \exp\left[-(4\pi\sigma_i/\lambda)^2\right] \tag{2.3}$$

The total transmission of the IFU, assuming perfect alignment of the output pupil is

$$T = \prod_i R_i = R_{\mathrm{Al}}^7 \exp\left[-(4\pi/\lambda)^2 \sum_i \sigma_i^2\right] \tag{2.4}$$

Assuming that all the mirrors within the IFU have the same surface roughness, σ, and that the proportion of light lost due to misalignment of the output pupil of the nth

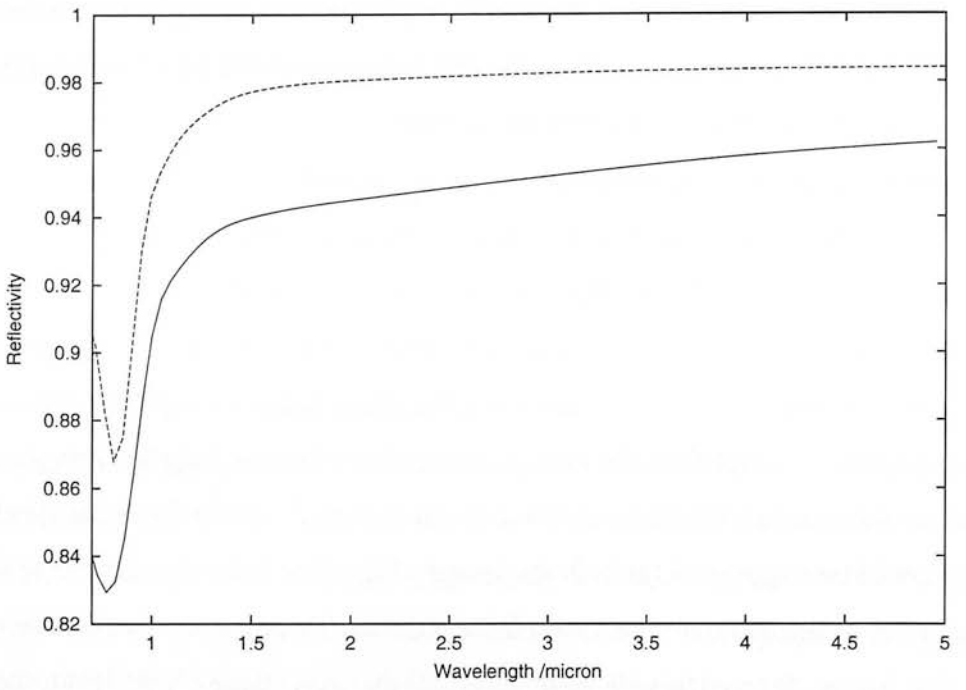

Figure 2.17: The reflectivity of aluminium alloy 6061 (solid line) and pure aluminium (dashed line) [Bass, 1995].

slice is $(1 - k_n)$, the transmission of the nth slice of the IFU can be written as

$$T_n = k_n R_{\mathrm{Al}}(\lambda)^7 \exp\left[-7 \times (4\pi\sigma/\lambda)^2\right]. \tag{2.5}$$

Using the values of the reflectivity of aluminium alloy 6061 shown in figure 2.17 [Bass, 1995] and estimating a value of $\sim$ 12 nm for the r.m.s. surface roughness of the mirrors and assuming that no light is lost due to misalignment of the pupil ($k_n = 1$) we predict that the transmission of the IFU should vary with wavelength as shown in figure 2.18.

2.6.4 Measuring the throughput using flat-field and arc observations

The transmission of the IFU can be measured by observing the same source with the IFU and with the two pixel wide slit, which is the same width as a single slice of the IFU, and dividing the IFU spectrum by the long-slit spectrum. This was done using the halogen lamp and argon lamp in the UIST calibration unit.

Both the long-slit spectrum and the IFU spectrum were divided by an imaging mode flat-field image to remove pixel to pixel and larger scale variations in the sensi-

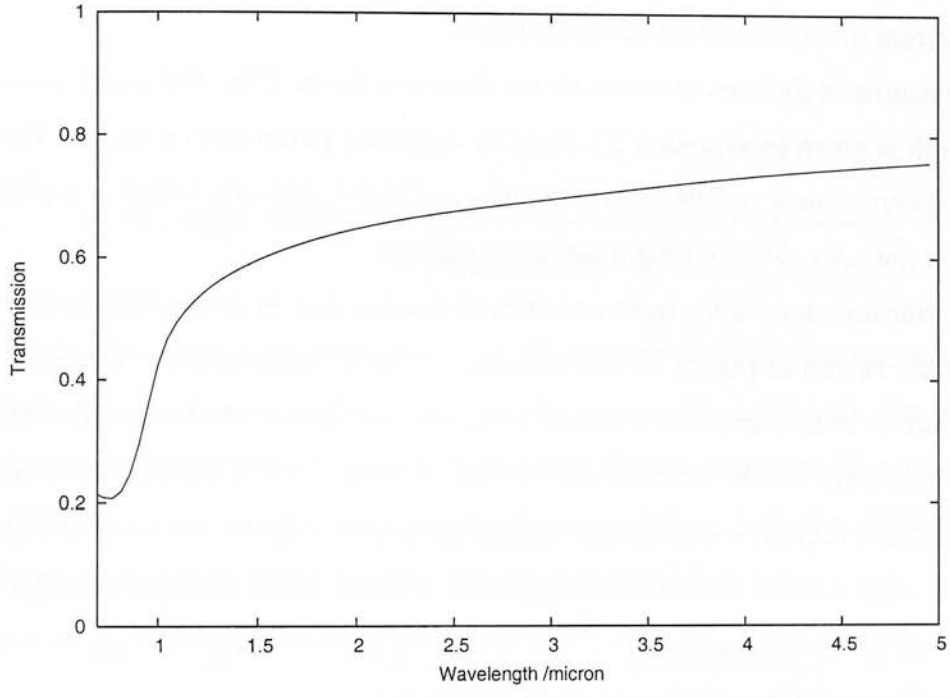

Figure 2.18: The predicted transmission of the IFU assuming that no light is lost due to misalignment of the output pupils and that the surfaces of the mirrors have an r.m.s. surface roughness of 12 nm.

tivity of the array. The slice images were extracted from the IFU spectrum and all rows were resampled to a a common wavelength scale (details of the procedures used to reduce IFU data are given in chapter 3). A 1-d spectrum was formed by averaging over all rows of the 2-d resampled spectrum. A spectrum was also formed by averaging over the length of the slit. When measuring the transmission using the halogen lamp this spectrum was resampled to the same wavelength scale as the IFU spectrum, and the IFU spectrum was then divided by the long-slit spectrum. When the argon lamp was used Gaussian profiles were fitted to individual spectral lines in the IFU and the slit spectrum to measure the ratio of the fluxes.

The results of these measurements are shown in figure 2.19. The curve plotted in this graph is given by equation 2.5 fitted by adjusting parameters k and σ. The best fit was given when $k = 0.942 \pm 0.008$ and $\sigma = (14.7 \pm 0.8)$ nm, which is a plausible value for the r.m.s. surface roughness of the mirrors.

The transmission varies from one slice to another due to small misalignments of each of the 14 output pupils, which will give different values of k for different slices. The variation in transmission is shown in figure 2.20. In the J-band the transmission varies from 0.413 ± 0.006 to 0.532 ± 0.006 with a mean over all the slices of 0.491. The slices with the highest transmission would therefore be expected to have a value of k which is 1.083 ± 0.015 times the average value of $k = 0.942 \pm 0.008$ previously found. This would give a value of $k_{\max} = 1.02 \pm 0.02$, a value consistent with $k_{\max} = 1$, which we would expect if the pupil were perfectly aligned.

In this chapter I have given an overview of UIST and the IFU and explained the procedures used to align the components of the IFU. The transmission of the IFU was measured as a function of wavelength in the J, H and K bands, and the curve produced from these measurements can be explained by the scattering from the mirrors in the IFU, the reflectivity of aluminium and small misalignments of some of the 18 output pupils. The image quality produced by the IFU and the transmission at longer wavelengths could only be measured once the instrument was installed on the telescope. These measurements are described in chapter 4. The data-reduction software required to extract useful measurements from the raw IFU data is outlined in the next chapter.

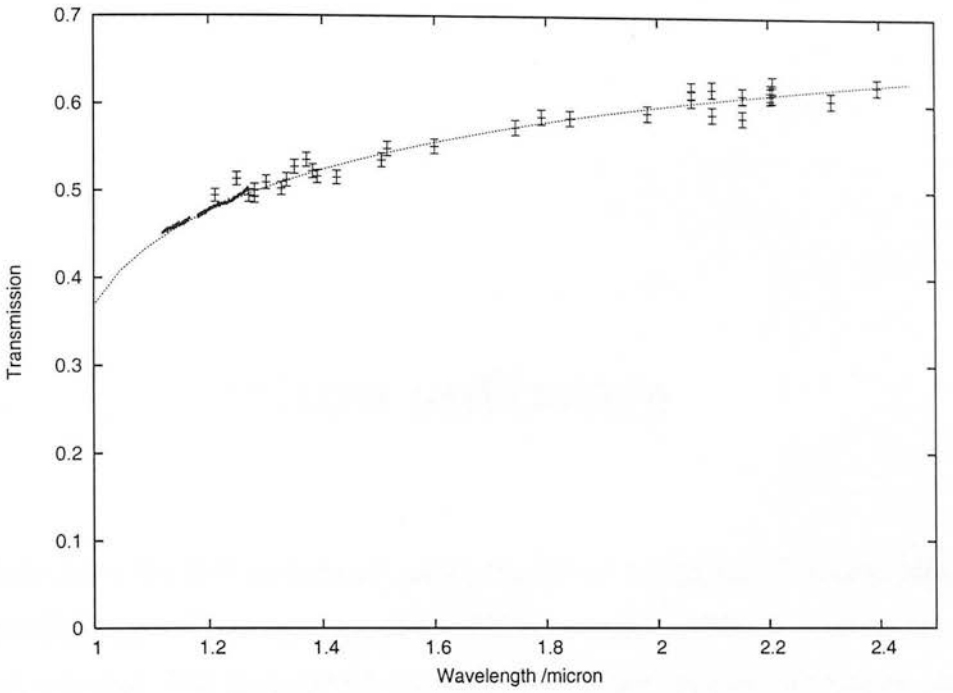

Figure 2.19: The average transmission of the IFU over all slices was measured by comparing the flux transmitted to that transmitted by the two pixel wide slit. The continuous data at short wavelengths was measured using the halogen lamp. The data points were measured by fitting Gaussian profiles to spectral lines from the argon lamp to determine the flux. The dotted line is given by equation 2.5.

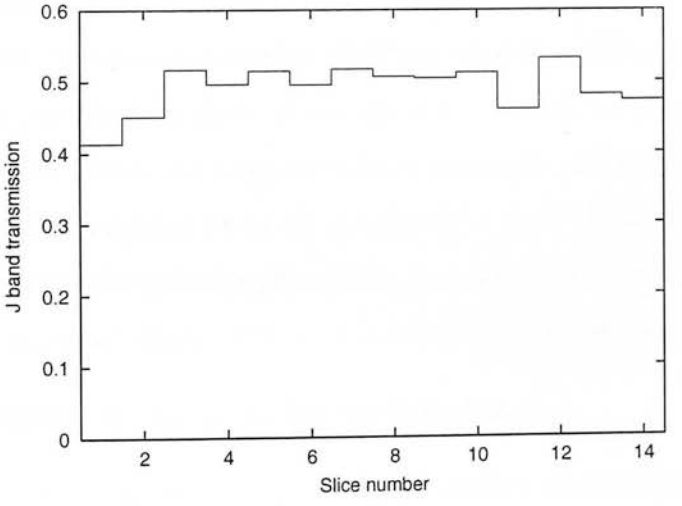

Figure 2.20: The transmission varies from one slice to another in the J-band ranges from 0.413 to 0.532 with a mean over all the slices of 0.491.

Chapter 3

Data-reduction software

The data from the IFU is reduced using the ORAC-DR pipeline system, already in use for imaging and spectroscopy at UKIRT. I was responsible for writing the scripts needed to reduce IFU data (which are described in this chapter) reusing or adapting components from the existing spectroscopy pipeline where possible.

3.1 Reducing IFU data

The raw output from the IFU is significantly harder to interpret than the output from a conventional long-slit spectrometer, and the reduction which must be carried out to extract measurements from the data is more complex. Each row in the raw output frame from the IFU contains a spectrum from one spatial pixel in the field of view. The 2-d spectrum produced by each slice in the output image forms a (y, λ) plane in the (x, y, λ) datacube. There is a large offset in wavelength calibration from one slice to another due to the staggered slit at the output focal plane of the IFU. There is also variation in calibration along the length of each slice spectrum due to curvature of the slice images. The essential stages of forming a datacube from the output of the IFU are

1. cut the 2-d spectrum from each slice out of the frame
2. align the 2-d spectrum from each slice in the dispersion direction
3. resample all rows of the output from all slices to a common wavelength scale
4. use each wavelength calibrated 2-d spectrum as a (y, λ) plane in the datacube.

Each (x, y) plane in the datacube is an image of the field at a given wavelength. Any misalignments in the optics of the IFU in the x direction shift the spectra in the dispersion direction,which is compensated for in the wavelength calibration of the spectra. Small misalignments in the y-direction shift the position of each slice image in the y-direction. However, the top and bottom of the slice image formed on the UIST array are defined by the slit-plane mask at the output of the IFU, which remains fixed. The image is therefore shifted in the y-direction within each slice image. It is necessary to shift each (y, λ) plane in the y direction to correctly align them to one another to reconstruct the image.

3.2 Overview of ORAC-DR

When observations are made using facility class instruments at UKIRT or using SCUBA at JCMT near real-time data-reduction is carried out using a system known as ORAC-DR [Economou et al., 2001]. Its primary function is to reduce data to a point where the observation can be assessed and to display it within seconds or minutes of the completion of the observation. In some cases publication quality results may be produced, but often further reduction of either the raw data or the final or intermediate products of the reduction is required.

ORAC-DR is a pipeline based system. Frames are processed consecutively from an input directory and the reduced data (and intermediate stages, some of which are deleted automatically once the reduction of the frame is complete) are written into an output directory. The observation type is identified using the headers in the file and the appropriate 'recipe' is applied. When ORAC-DR is run in real-time mode it watches the directory into which raw data files are written, waiting for a new file to be written. It can also be run off-line to re-reduce old data, possibly to use a different recipe, or different calibration data. The system is designed to be non-interactive, and the only means of controlling the reduction is by the contents of the headers of the files, the configuration files stored in the ORAC-DR calibration directory and options specified on the command line when the reduction is started.

A schematic view of the operation of ORAC-DR is shown in figure 3.1. Once it has been initialised it enters a loop, checking for data. If it finds a file ready for re-

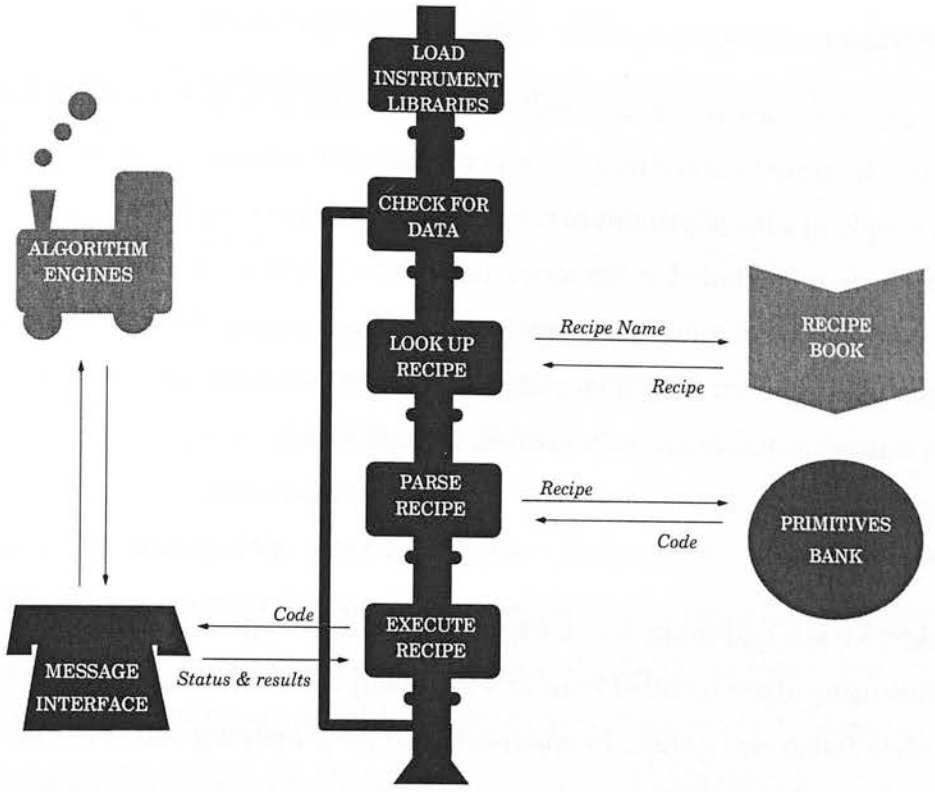

Figure 3.1: A schematic view of the operation of ORAC-DR (taken from Jenness and Economou [2001])

duction it obtains the name of the recipe to be used from the headers of the file (or it may be specified on the command-line) and retrieves the recipe itself from the recipe book. The recipe is parsed, and the primitives used by the recipe are obtained from the primitive bank. Each primitive is intended to correspond to a single meaningful stage of the reduction. The recipe is then executed. Operations are carried out using external algorithm engines, controlled via a message interface. At present the Starlink KAPPA, FIGARO and CCDPACK packages are used as the algorithm engines. Once the recipe has been executed ORAC-DR returns to the beginning of the loop, waiting for more data.

In most recipes the output data includes one or more 'group' files. These are files in which several frames are combined. This is used, for example, when a mosaic of imaging observations is formed, or when pairs of spectra are subtracted to remove the sky background and the resulting sky-subtracted spectra are added to increase the signal to noise ratio of the measurement.

3.2.1 Recipes

A recipe consists of a series of data-reduction steps, each of which is carried out by a 'primitive'. In order to make recipes more readable for non-programmers the recipe consists simply of a list of primitives to be executed, each of which is a Perl script. No Perl constructs are included in the recipe itself. The recipes are written in plain text, making modification possible using any text editor. Documentation is included within the recipes using the Perl POD (Plain Old Documentation) mark-up format which can easily be automatically converted to HTML or LaTeX format.

3.2.2 Primitives

Each primitive is a Perl script which carries out a single stage of the reduction. They are written using object oriented techniques to manipulate objects associated with the current data frame and group. In object-oriented programming each object is a collection of data with associated 'methods' which can be carried out on the object. For example, each frame is an object. The data associated with the frame object include the name of the file containing the frame and the contents of the headers of the frame. Most of the methods applied to the frame object are used to access, modify or add to this data. The actual processing of the data is carried out by sending instructions to the algorithm engines (the Starlink KAPPA, FIGARO and CCDPACK packages). Primitives may include calls to other primitives, to break the data reduction down into yet simpler stages. The primitive does not need to make any assumptions about the data location, file naming convention or frame number. This is all handled by instrument specific classes, allowing re-use of primitives for data from different instruments.

Simple scalar arguments can be passed to the primitive from the calling primitive or recipe, but other than this there is no communication between primitives and no data is shared between them other than that contained within the frame and group objects passed through the pipeline. Information can be added to the frame or group and passed down the pipeline by adding named entries to the user defined headers associated with the frame and group objects. Each header entry may contain either a simple scalar value or a reference to a more complex data structure. Ensuring that information is only passed into primitives in this well defined way makes it much

more straightforward to re-write one primitive without unexpectedly affecting other primitives later in the pipeline or to re-use primitives in new recipes in combination with new primitives.

3.2.3 Calibration data

When calibration observations, such as arc spectra, darks or flat-field images, are reduced they are filed in a calibration index. When a calibration frame – such as an arc spectrum, a dark frame or flat-field frame – is required, the recipe asks the ORAC-DR calibration system to automatically select the most appropriate frame which has been reduced so far. This is done using a 'rules file' which specifies which headers in the calibration frame must match those in the frame to be reduced and hence which parts of the instrument configuration must be unchanged if the calibration is to be valid. For example, when identifying a suitable flat-field frame to apply to a spectroscopy observation you would require the same slit, grism and filter to be used, however it would not matter if other parts of the instrument configuration, such as the exposure time, were to vary. If more than one valid calibration frame is found for a given observation then the calibration measured closest in time to the observation is used.

3.2.4 ORAC-DR and UIST

The existing generic imaging and spectroscopy recipes and primitives already used to reduce data from a number of near-IR instruments are used to reduce UIST data. A new set of recipes and primitives were required to reduce integral field data from UIST, though many of the existing spectroscopy primitives were re-used or modified.

IFU data is significantly more complex to reduce than imaging or long-slit spectroscopy data, so it is unlikely that observers would wish to re-reduce the raw data using other data-reduction packages. It is also much harder for an observer to interpret the raw data and assess the observation from this in the way that is often possible for long-slit spectra. It is therefore essential that the IFU recipes reliably extract the spectra from the raw frame, wavelength calibrate them and form them into a datacube.

The data reduction pipeline must be able to take a sequence of frames including

arc and flat-field calibration frames and sky and object observations and produce a co-added, sky-subtracted, wavelength calibrated, flat-fielded datacube. The datacube is saved as a standard Starlink NDF file which may be analysed or processed further using tools from the Starlink Software Collection, including the Datacube package [Allan, 2001], which uses routines from the Starlink FIGARO and KAPPA packages to allow interactive examination of the data-cube and provides scripts to simplify tasks such as producing a velocity map from the data-cube. NDF files can also easily be converted to other formats, such as FITS, for use with other data reduction software.

3.3 Masking bad pixels and adding variance arrays

A bad pixel mask is applied to all frames. This consists of a static mask of permanently bad pixels combined with a mask created by the ARRAY_TESTS recipe which is run at the beginning of each night to detect new or transient bad pixels.

A variance array is created and attached to the data array. This is then propagated through the pipeline. When the data are manipulated or frames are combined in some way the variance arrays are processed as appropriate. These variance arrays can then be used during analysis of the data.

3.3.1 Readnoise variance

Initially the readnoise variance is calculated. This is currently set to a single value for all pixels on the array. The raw read-noise level, $\sigma_{\rm rn}$, is measured by the ARRAY_TESTS recipe run at the start of each night. This value must be divided by the gain of the system, g, to get a value in data units rather than electrons. The UIST array is almost always read in NDSTARE (non-destructive read) mode. The signal on each pixel is measured n times ($n \geq 2$) during the integration and the signal measured is the gradient of the line fitted through these n values, which is proportional to the flux falling on the pixel (assuming that the signal is not large enough to reach the non-linear part of the response of the array). This reduces the readnoise by a factor, f, given by

$$f = \sqrt{\frac{n(n+1)}{6(n-1)}}, \tag{3.1}$$

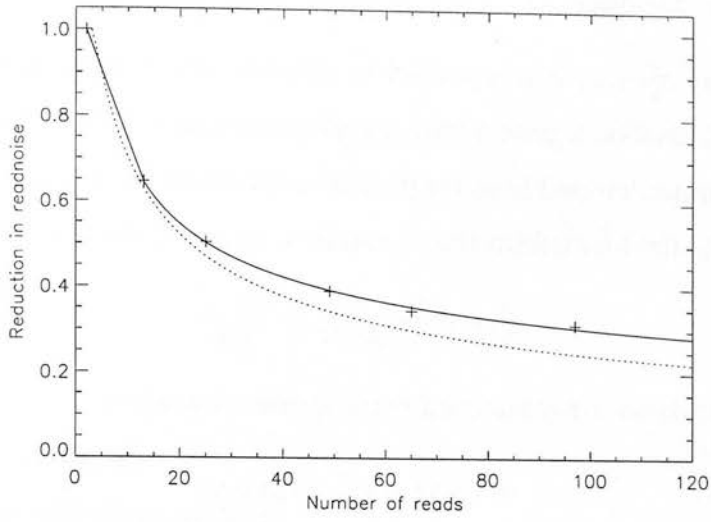

Figure 3.2: The factor by which the readnoise is reduced for multiple reads was measured for UIST and a line was fitted to these measurements (solid line), given by equation 3.2. The dotted line is given by equation 3.1.

as shown by Chapman et al. [1990]. Fitting a line through the n values is carried out within the EDICT system used to control and read the array. As part of this process cosmic rays are detected and removed. These operations therefore do not need to be carried out by ORAC-DR.

For UIST this does not accurately describe the reduction in readnoise when large numbers of reads are made. The readnoise was measured with numbers of reads, n, from 2 to 100 (figure 3.2), and a function was determined to fit this data with the form

$$f = \begin{cases} 1.0644 - 0.0322n & \text{if } n \leq 12 \\ 1.5616(n-1)^{-0.3568} & \text{otherwise} \end{cases} \tag{3.2}$$

There may also be more than one exposure in an integration. In this case the readnoise is reduced by a further factor of $\sqrt{N}$, where N is the number of exposures in the integration. The readnoise variance value of each pixel of the array is therefore given by

$$\sigma'^2_{\mathrm{rn}} = \frac{\sigma^2_{\mathrm{rn}}}{Nf^2g^2}.$$

3.3.2 Poisson variance

A variance array $\sigma_p^2(x, y)$ is constructed to represent the Poisson noise on the measurement. The signal on a given pixel, $s(x, y)$ is given by n_e/gN where n_e is the total number of electrons detected from the pixel over the entire integration (which consists of N exposures) after bias subtraction if required, so the Poisson variance on $s(x, y)$ is

$$\sigma_p^2(x, y) = \frac{n_e}{g^2 N^2} = \frac{s(x, y)}{gN}$$

The initial variance array attached to the frame is therefore

$$\sigma^2(x, y) = \sigma_{rn}'^2 + \sigma_p^2(x, y)$$

3.4 Reduction of flat-field frames

The first frame to be observed in any sequence of IFU observations should be a flat-field frame. This is made by observing either the IR grey-body source or the halogen lamp in the UIST calibration unit using the same grism and filter as is to be used for astronomical observations. An unreduced flat-field frame is shown in figure 3.4. The flat-field is used not only to remove pixel to pixel and larger scale variations in sensitivity of the detector array, but also to account for the variation in transmission from one slice to another of the IFU and to locate the slices on the array. The operation of the REDUCE_FLAT recipe is outlined in figure 3.3, and described in more detail below. A reduced flat-field frame produced from the frame shown in figure 3.4 is shown in figure 3.5.

3.4.1 Locating the slices on the array

In order to extract the 2-d spectrum produced by each slice and use it to form a plane in a datacube it is essential to locate the top and bottom of each slice on the array. The curvature and tilt of the spectra formed on the array is sufficiently small (sub-pixel) to allow us to neglect these effects when extracting the spectra. When no grism is in the beam an image of the IFU slices is formed on the array. In theory inserting a grism into the beam should simply disperse this image in the x-direction on the array, leaving the positions in the y-direction unchanged. However, small misalignments and deviations

REDUCE_FLAT

measure offset of positions of slices relative to positions in `ifu_profile.dat` file

mask bad pixels

add readnoise variance

add Poisson variance

locate slices

extract slices

normalise the flat-field

file it with the calibration system

Figure 3.3: Flat-field frames are reduced and filed with the ORAC-DR calibration system by the REDUCE_FLAT recipe.

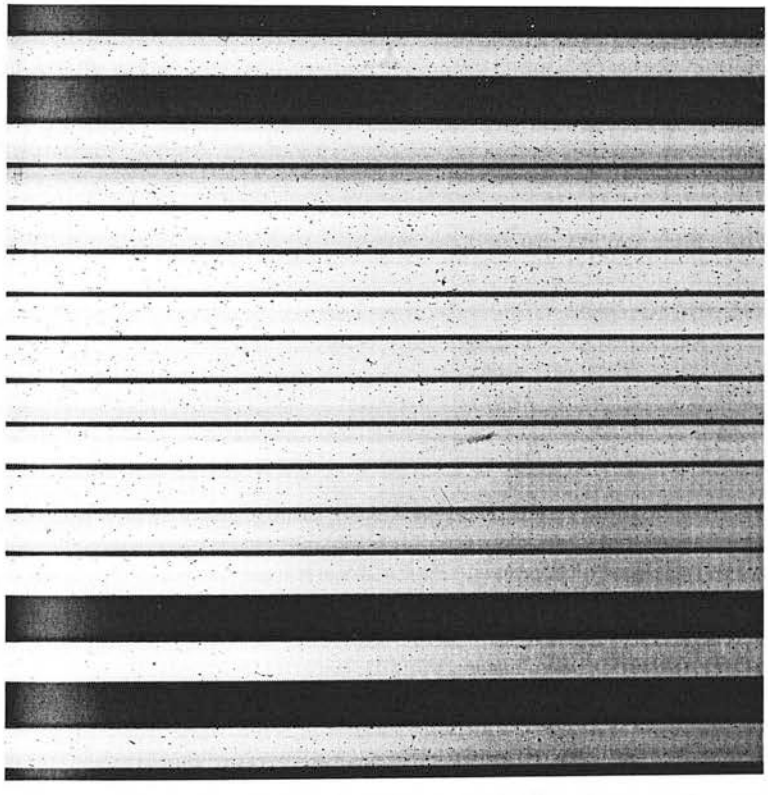

Figure 3.4: An unreduced flat field frame made using the short-*K* grism and the blackbody source in the UIST calibration unit.

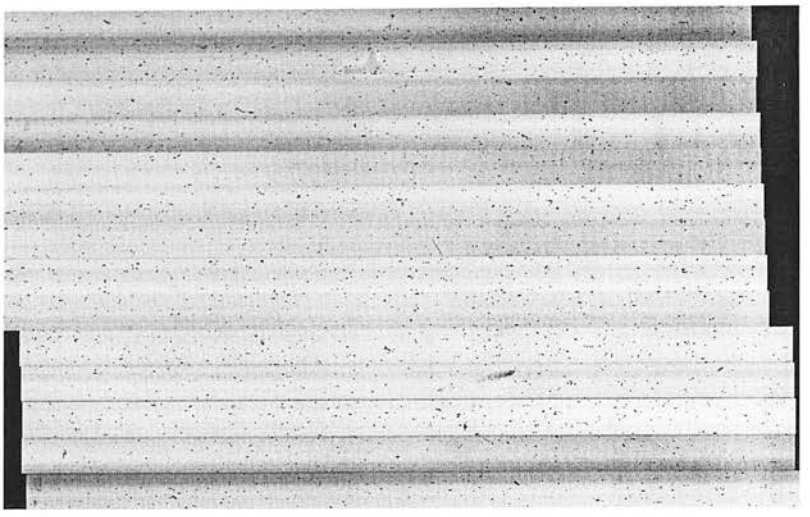

Figure 3.5: The flat-field frame shown in figure 3.4 after reduction. The slices have been cut out of the image, approximately aligned in the dispersion direction and rearranged in the order in which they appear on the field of view of the IFU and without gaps between one another. The spectrum has been normalised using a black-body spectrum.

from flatness of the surfaces of the grisms cause the image to be shifted on the array. Shifts in the dispersion direction are compensated for during wavelength calibration. To locate the top and bottom of each slice we need to know the relative positions of all the slices and the shift which should be applied to these positions when a particular grism is inserted.

The relative positions of the slices were obtained by averaging a flat-field frame in the dispersion direction. The top and bottom of each slice was then measured as the position at which the intensity fell to 50% of the maximum intensity. A shift was applied to all these positions so that the bottom of the slice at the bottom of the array was at 0. The positions of all the slices were then listed in the order in which the slices should appear in the final datacube, rather than the order in which they appear on the array, and were then stored in a file in the ORAC-DR calibration directory, which can be accessed by recipes and primitives. This file also includes the shifts which should be applied to approximately align each slice in the dispersion direction and to align each slice in the y-direction in the final data-cube to correctly reconstruct the image. The values in this file should not change except after physical adjustment of the optics

y-start	y-end	x-shift	y-shift
743	789	31	-0.10
286	332	25	0.71
628	674	26	-0.39
400	446	24	-0.13
514	560	22	-0.14
457	503	-9	4.41
571	617	-12	2.88
343	389	-15	4.19
686	732	-16	4.58
229	275	-20	4.13
800	846	-21	5.59
114	160	-26	3.16
914	960	-25	4.90
0	46	-32	3.53

Table 3.1: The values in the `ifu_profile.dat` file, described in the text. The y-shift values were obtained from observations made on 5 December 2002, during UIST commissioning, as described in 4.1.

of the IFU. The contents of this file are shown in table 3.1.

When a flat-field frame is reduced the _MEASURE_OFFSET_ primitive is used to measure the offset which must be applied to the statically determined positions to locate the slices. A one dimensional profile, $A(y)$, is formed by averaging in the dispersion direction. A similar profile, $B(y)$, is created which contains a value of 1 within the slices whose positions are given in the `ifu_profile.dat` file and 0 otherwise. The shift between the two is given by the integer value of s which maximises the cross-correlation (and, therefore, the total transmitted flux)

$$\theta(s) = \sum_y A(y)B(y+s).$$

The value of s is then stored with the ORAC-DR calibration system for use with that grism and filter combination.

The _LOCATE_SLICES_ primitive is then used to combine the relative positions stored in the calibration file with the offset measured and filed with the calibration system. The position of the top and bottom of each slice on the array is calculated and these positions, along with the x and y-shifts given in the calibration file are written into the headers of the file for use by subsequent primitives. As in the calibration file

these values are stored in the order in which the slices are arranged on the sky rather than the order in which they appear on the array.

3.4.2 Extracting the slices

Once the slices have been located on the array by the _LOCATE_SLICES_ primitive they can be extracted by the _EXTRACT_SLICES_ primitive. This reads the positions and x and y-shifts from the headers of the file. Each slice is then cut out of the image, shifted in x by the distance specified (which is an integer, so no resampling takes place) and pasted into a new image in such a way that the slices are now arranged in the order in which they cover the field of view. The shift in the x direction approximately aligns all the spectra in the dispersion direction. The frame now looks similar to a conventional long-slit spectrum, and indeed can be treated as such for many subsequent stages of the reduction. The new positions of the slices are written into the same headers from which the original positions were read, preserving the y-shift values and setting the x-shift values to 0.

3.4.3 Normalising the flat-field frame

Once we have extracted the spectra and approximately aligned them in the dispersion direction we can use the standard ORAC-DR spectroscopy primitives to reduce our flat-field frames. All rows of the image are divided by a black-body spectrum at the temperature of the IR filament source in the UIST calibration unit or by a polynomial fit to the average spectrum over the whole array when the halogen lamp is used. This removes large scale features in the spectrum of the flat-field source. The accuracy of this stage is not critical to the data reduction because the same flat field image will be used for the reduction both of the object being observed and the standard star used for flux calibration and removal of spectral features due to the atmosphere. When the object spectrum is divided by the standard spectrum the dependence on the spectrum of the light source used to produce the flat-field frame disappears. The flat-field image is normalised to have a mean value of 1 and filed with the ORAC-DR calibration system for later use.

The resulting flat-field looks a lot less flat than would be expected from a long-slit

spectrometer. This is because the flat-field is used not only to remove pixel to pixel and larger scale variations in the sensitivity of the array but also to account for the different transmission of individual slices of the IFU.

3.5 Reduction of arc spectra

An arc spectrum will generally be observed after the flat-field and before making observations on the sky. The UIST Calibration Unit contains two arc lamps (argon and krypton) for wavelength calibration. When an arc spectrum is reduced the slices are again extracted and approximately aligned in the dispersion direction in the same way as the flat-field frame. The frame is then divided by the normalised flat-field. A raw arc spectrum and the slices extracted from this spectrum are shown in figures 3.7 and 3.8.

3.5.1 Determining the wavelength calibration

The standard spectroscopy recipes in ORAC-DR do not use the arc frame to accurately wavelength calibrate subsequent data. Instead, an estimated linear wavelength scale is applied using the angle of the CGS4 or Michelle grating or the choice of UIST grism to set the central wavelength and dispersion. The observer is then expected to calibrate the arc frame and apply the calibration to their data. This is not practical for IFU data because it is necessary to resample all the rows of the 2-d spectrum to the same wavelength scale before forming them into a datacube.

After flat-fielding, the 2d spectrum from each slice is smoothed in the y-direction with a 6 pixel median filter. This effectively interpolates over any bad pixels (the FIGARO **iarc** routine does not understand bad pixels) and increases the signal to noise ratio of weak lines. The spectrum from each slice varies very slowly in the y-direction so the spectrum is not degraded by this process. Each row of the 2d spectrum is then individually wavelength calibrated using the **iarc** routine from the Starlink FIGARO package. This routine was designed to remove curvature from spectral lines in long-slit spectra. A file containing a list of arc lines giving a wavelength and x-position of each line is required. For straightening curvature in conventional long-slit spectra this

REDUCE_ARC

mask bad pixels

add readnoise variance

add Poisson variance

locate slices

extract slices

divide by flat-field

interpolate over bad pixels

obtain appropriate arc lines file from calibration system

run **iarc** to wavelength calibrate

file with calibration system

resample all rows to common wavelength scale

Figure 3.6: Arc frames are reduced using the REDUCE_ARC recipe. Once the wavelength calibration has been measured all rows are resampled to a common wavelength scale, allowing the user to check that the calibration has been successful (easily seen by whether all the arc lines are straight).

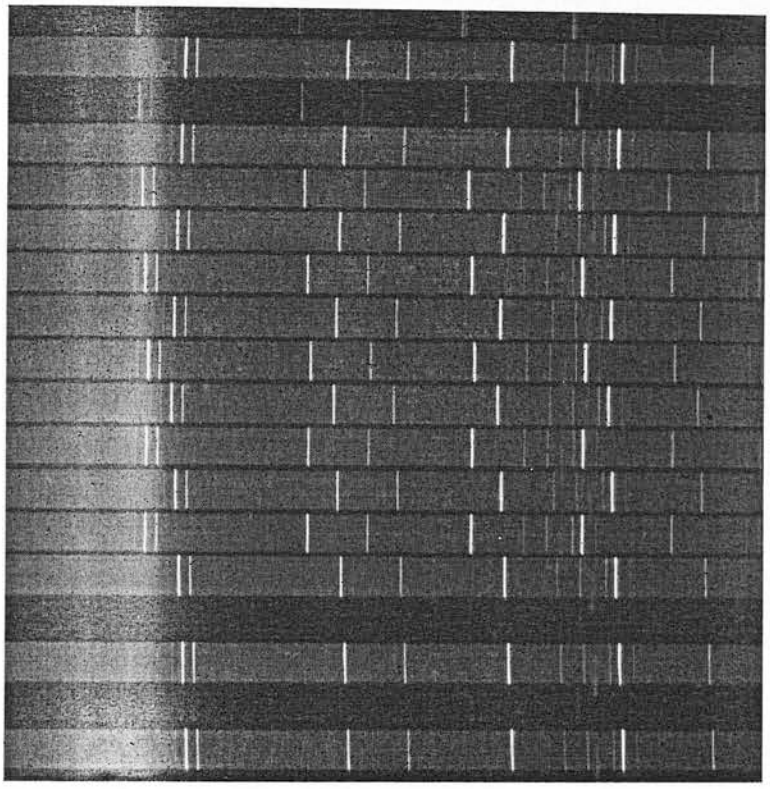

Figure 3.7: An unreduced arc frame made using the short-*K* grism and the argon lamp in the UIST calibration unit. The wavelength increases to the left. The intensity shown in this image is proportional to the logarithm of the flux for increased clarity.

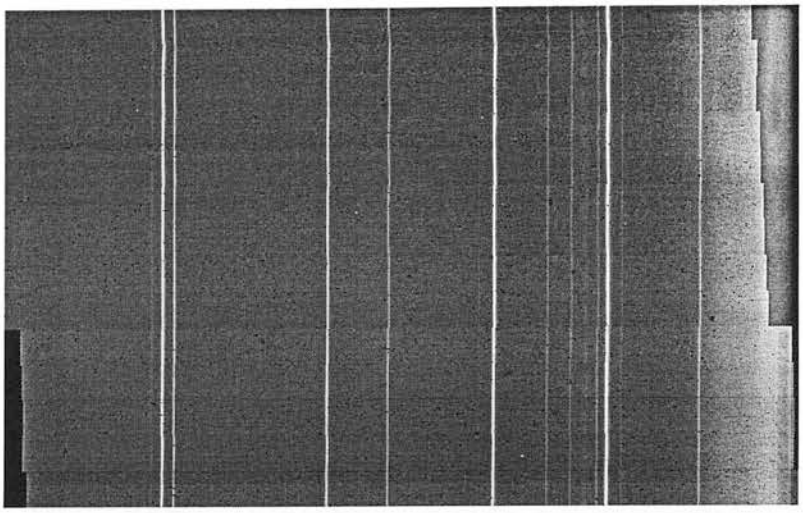

Figure 3.8: The slices are extracted from the image shown in figure 3.7, rearranged in the order in which they cover the field of view, with no spaces between them and approximately aligned (to $\sim$ 1 pixel) in the dispersion direction. This frame is used to determine the wavelength calibration.

list is generally obtained by extracting a single spectrum from the 2-d frame and identifying the arc lines using the FIGARO **arc** routine. This file is then read by **iarc**, which begins at the row from which the spectrum was extracted and traces each identified arc line from one row to another, writing a file containing a wavelength calibration, specified as a set of polynomial coefficients, for each row of the spectrum. This method can be used to determining a wavelength calibration for each row of an IFU frame because the shifts that have been applied to the spectra in the dispersion direction have aligned them to an accuracy of $\sim$ 1 pixel, allowing the arc lines to be traced from one slice to another. It is also not necessary to generate a new list of arc lines each time an arc is reduced because, unlike the continuously variable central wavelength of the spectrum when a grating spectrometer is used, the UIST grisms each give a single spectral range. The accuracy to which the UIST grism and slit wheels can be positioned ensures that the arc lines always fall in the same place on the array to $\ll$ 1 pixel, so once a list of arc lines has been generated it should be usable unless some part of the UIST optics is realigned. This allows non-interactive wavelength calibration using a set of static arc line lists, which were determined during the commissioning period at UKIRT. The file produced by **iarc** containing the wavelength calibration for each row of the frame is

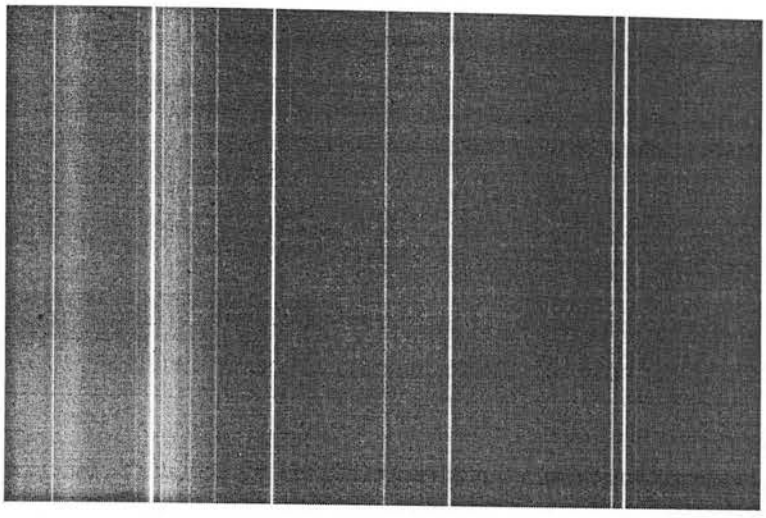

Figure 3.9: After applying the wavelength calibration to the arc spectrum and resampling all rows to a common wavelength scale the arc lines are straight to sub-pixel accuracy. The wavelength scale now increases to the right.

stored with the calibration system for use in wavelength calibrating subsequent observations. The IFU recipes produce automatically wavelength calibrated spectra rather than the estimated wavelength scale applied by the existing spectroscopy recipes.

3.5.2 Applying the wavelength calibration

Once the wavelength calibration has been obtained it is then used by the FIGARO **iscrunch** routine to resample all the rows onto a common, linear wavelength scale and the resulting 2-d spectrum is displayed (figure 3.9). It is not absolutely necessary to apply the wavelength calibration to the arc frame in this way – the calibration is intended to be used to calibrate other frames – but this allows the observer to check that the automatic wavelength calibration has worked correctly by seeing that the arc lines are now straight.

When the spectra are resampled their associated variance arrays are resampled in the same way. This is not strictly correct because resampling introduces correlations between adjacent pixels, and the simple variance arrays should, theoretically, be replaced by a covariance array specifying the correlated errors. In practice this would be a huge, unwieldy matrix, slowing down processing speeds and using unacceptable amounts of disc space and it would provide little benefit because the standard data

analysis packages would not be able to make use of it.

Resampling the variance array in the same way as the data is a good approximation. This was shown by generating a spectrum, $s_0(x)$, consisting of 1000 elements each with a value of 100, and adding Gaussian spikes with a FWHM of 3 pixels and height of 100. Gaussian noise was added to 100 copies of this spectrum, $s_1(x) \ldots s_{100}(x)$ with $s_n(x) = s_0(x) \pm \sqrt{s_0(x)}$, simulating Poisson noise. All of these spectra were then scrunched to a linear wavelength scale using the FIGARO **iarc** routine, producing resampled spectra $s'_n(x)$. The r.m.s. error from the correct value at each pixel was measured as

$$\sigma^2_{\text{meas}}(x) = \frac{1}{100} \sum_n (s'_n(x) - s'_0(x))^2.$$

The noise added to the model spectra was purely Poisson noise, so the variance array associated with the model spectra was equal to the data array $s_0(x)$. The scrunched variance array is therefore given by $s'_0(x)$. The ratio of the error given by the scrunched variance array to the true error on a given pixel is

$$\alpha(x) = \sqrt{\frac{s'_0(x)}{\sigma^2_{\text{meas}}(x)}}.$$

It was found that $\alpha(x)$ did not vary systematically with x (with proximity to the Gaussian peaks). When the 1000 pixel test spectrum was scrunched to 800 pixels the mean value of $\alpha(x)$ over the spectrum, $\overline{\alpha}$, had a value of 1.09, showing that the scrunched variance array gives a 9% overestimate of the error on a given pixel. When the test spectrum is scrunched to 1200 pixels $\overline{\alpha}$ rises to 1.20. There is also significant correlation of the errors on adjacent pixels. The overestimated errors and the correlations are produced because the resampling acts as a mild smoothing filter. If the data are binned in the resampled direction with N pixels per bin the signal to noise ratio will not be increased by a factor of $\sqrt{N}$ due to the correlated errors, however the errors on adjacent bins will no longer be strongly correlated and $\sqrt{s'_0(x)/N}$ becomes a more accurate estimate of the error on each binned value.

When we resample IFU spectra we are scrunching from a slightly non-linear wavelength scale to a linear scale with the same number of pixels, which will produce a slight variation in α across the spectrum. Typically the error on a given pixel will be overestimated by $\sim 15\%$ by the scrunched variance array.

Accuracy of the wavelength calibration

In order to measure the accuracy of the wavelength calibration an argon arc frame taken using the *HK* grism was reduced in this way. The wavelength calibration produced was then applied to the arc frame itself before the median filter was used to interpolate over bad pixels. An arc line of known wavelength (21540.09 Å) was measured for all 658 rows in the spectrum by fitting a Gaussian profile to the line. The mean measurement of the wavelength over all rows was found to be (21540.10 ± 0.01) Å, so there is no significant systematic discrepancy between the measurements and the known wavelength. The random scatter in the measurement gives an r.m.s. discrepancy from the known wavelength of 0.3 Å corresponding to 0.03 pixel (the *HK* grism has a dispersion of 10.7 Å/pixel).

From these measurements we see that any systematic discrepency is much smaller than the random error from one row to another. The wavelength calibration of a given row is correct to 0.03 pixel. For most applications the accuracy of wavelength measurements will be limited by the accuracy to which a Gaussian profile can be fitted in the presence of noise, rather than the accuracy of the wavelength calibration.

3.6 Reduction of standard star observations

Standard star observations with the IFU are generally made with one sky and one object position, producing a sky-subtracted datacube of a single 3.3 × 6.0 arcsec field. To reduce overheads due to time spent offsetting the telescope the observations are generally made following the pattern object-sky-sky-object (however, the data reduction software does not assume this order). Each of these blocks of four frames is known as a 'quad'. The sequence of operations carried out by the STANDARD_STAR recipe is shown in figure 3.10.

3.6.1 Sky subtraction and coadding of observations

An unreduced standard-star spectrum is shown in figure 3.11.The frame is initially treated in the same way as the arc frame. The slices are cut out of the frame and shifted, the frame is flat-fielded. If the frame is the first of a sky-object or object-sky

STANDARD_STAR

mask bad pixels
add readnoise variance
add Poisson variance
locate slices
extract slices
divide by flat-field
if the frame completes a pair
    subtract sky from object frame
    resample all rows to common wavelength scale
    if the group file already exists
        n = number of pairs already included in group file
        multiply group file by n
        add new sky-subtracted frame
        divide by $n + 1$ to produce updated group file
    else
        copy frame to create new group file
    endif
    extract spectrum using optimal extraction
    divide by exposure time
    look up magnitude and spectral type on Simbad
    store V-magnitude, spectral type and temperature in calibration system
    generate black-body spectrum at T of star, normalised to 1 at central wavelength
    divide stellar spectrum by normalised black-body
    file standard-star spectrum with calibration system
endif

Figure 3.10: Observations of a standard-star are reduced and filed with the calibration system using the STANDARD_STAR recipe.

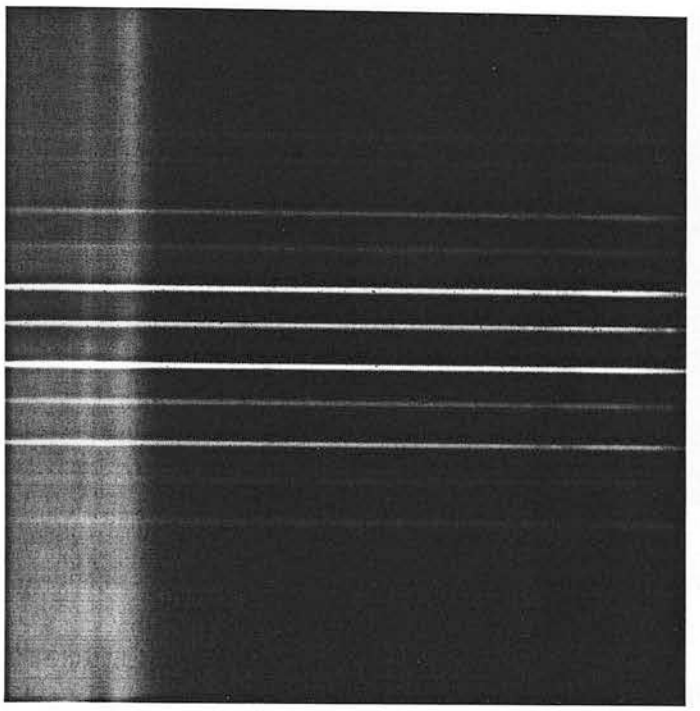

Figure 3.11: An unreduced standard star spectrum observed using the short-*K* grism.

pair then the reduction of the frame ends at this stage. If the frame is the second of a pair then the sky frame is subtracted from the object frame. The frame should be identified as 'OBJECT' or 'SKY' by one of the headers in the file. The value of this header is set in the ORAC-OT sequence used to control the telescope and instrument during the observations.

The wavelength calibration measured from the arc frame is applied to the resulting sky-subtracted frame to resample all the spectra to a common wavelength scale, as shown in figure 3.12. This frame is then coadded to a group frame, containing a 2-d spectrum which will increase in signal to noise ratio as more frames are added.

3.6.2 Extracting the standard-star spectrum

The spectrum of the standard star is obtained from this 2d group file using the FIGARO profile and optextract routines, which implement the optimal extraction method described by Horne [1986] which weights each pixel in order to give the highest possible signal to noise in the spectrum while maintaining an unbiased measurement of the flux at each wavelength. The spectral type and magnitude of the standard-star are

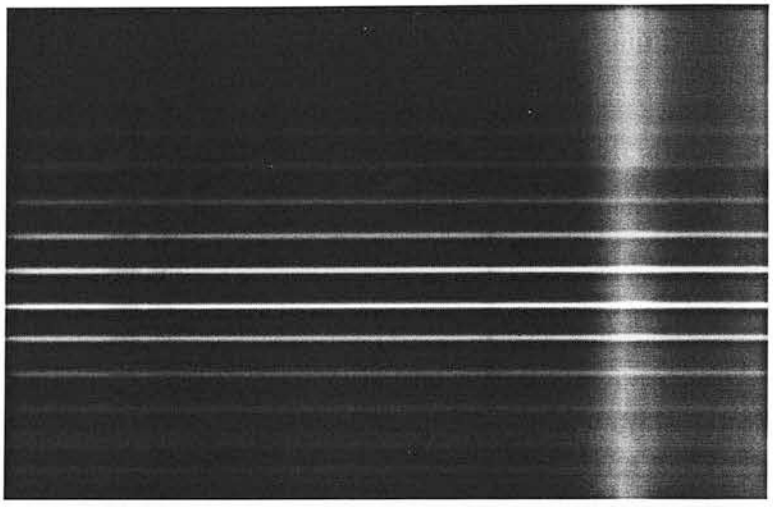

Figure 3.12: A reduced standard star spectrum, produced from the raw spectrum shown in figure 3.11. The slices have been extracted and rearranged and all spectra have been resampled to a common wavelength scale.

looked up automatically in the Simbad catalogue, and are stored by the calibration system. A black-body spectrum at the temperature of the star (taken from the stellar type) is created and normalised to have a value of 1 at the central wavelength of the spectrum. The standard star spectrum is divided by this normalised black-body spectrum in order to remove the intrinsic spectral shape of the star, leaving a measurement of the transmission of the atmosphere, telescope and instrument as a function of wavelength. This spectrum is then filed with the calibration system for later use. The spectrum produced by the reduction of the group of which figure 3.11 forms one frame is shown in figure 3.13.

3.6.3 Forming a datacube

The frame is then formed into a datacube. This is to allow an image of the field of view of the IFU to be produced by averaging the datacube over a range of wavelengths, which can be shown to the observer in order to check that the star is well within the field of view.

The _FORM_DATACUBE_ primitive reads the positions of the slices from the headers of the file. The slices are cut out of the frame in the order in which they are listed in the headers and each becomes one (y, λ) plane of the datacube. Each plane

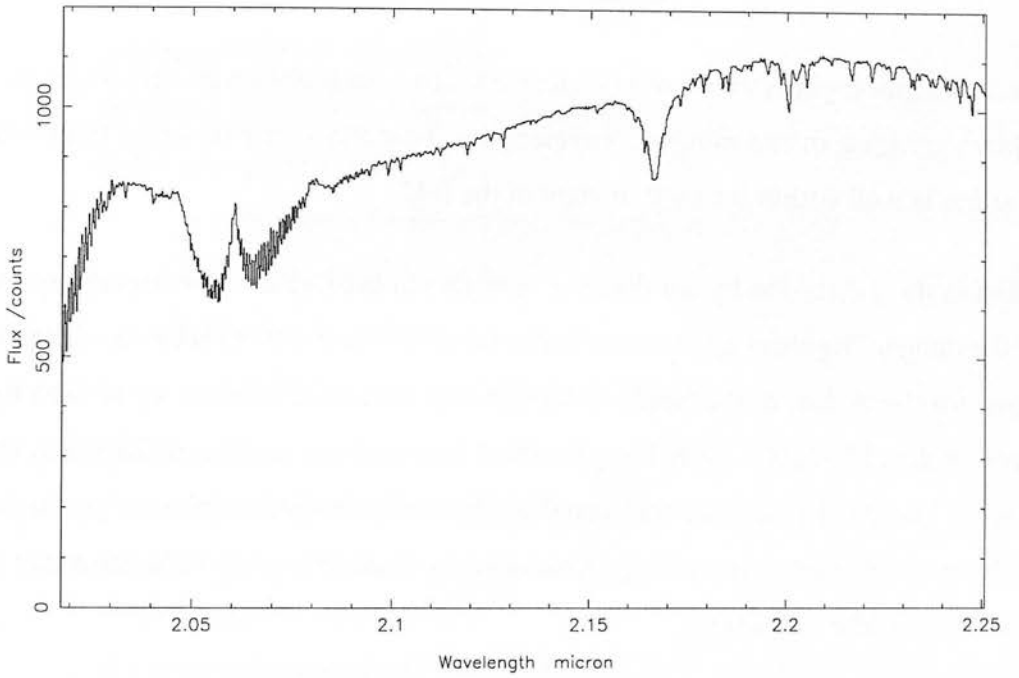

Figure 3.13: The 1-d spectrum extracted from the 2-d spectrum shown in figure 3.12 by optimal extraction and divided by a black-body spectrum of appropriate temperature.

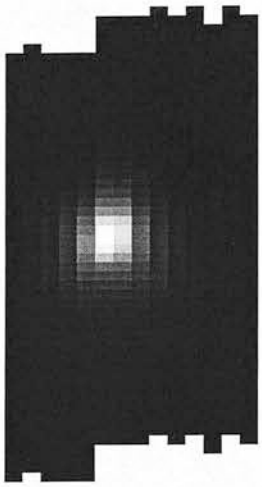

Figure 3.14: Once the spectrum has been formed into a datacube an image can be produced by averaging over a range of wavelengths. This allows the observer to ensure that the star is well within the field of view of the IFU.

is shifted in the y direction by the distance specified in the headers to correctly reconstruct the image. The slices are also shifted in the dispersion direction by the distance specified for the x-shift in the headers, though this should have been set to zero for all slices by the _EXTRACT_SLICES_ primitive. The variance array is reshaped in the same way. The y-shift distance will generally be a non-integer number of pixels, so again the true covariance array is approximated by resampling the variance array in the same way as the data array.

3.7 Observing a single pointing

The most common use of the IFU is expected to be observations of one object and one sky position. Reduction of these observations is carried out using the EXTENDED_SOURCE recipe, outlined in figure 3.15. A variant of this recipe: EXTENDED_SOURCE_NOSTD is also available. This does not divide the spectra by that of a standard star or flux calibrate them. It is intended for use when observation of the standard-star has been postponed until after observation of the object. The _NOSTD version can be used to monitor the progress of the observation, and the data can then be re-reduced once the standard-star has been observed and the calibration data reduced.

EXTENDED_SOURCE

mask bad pixels
add readnoise variance
add Poisson variance
locate slices
extract slices
divide by flat-field
if the frame completes a pair
    subtract sky from object frame
    resample all rows to common wavelength scale
    if the group file already exists
        n = number of pairs already included in group file
        multiply group file by n
        add new sky-subtracted frame
        divide by $n + 1$ to produce updated group file
    else
        copy frame to create new group file
    endif
    form group file into datacube
    if we are not using the EXTENDED_SOURCE_NOSTD version of the recipe
        divide by standard-star spectrum
        divide by exposure time
        flux calibrate
    endif
    extract images and spectra and display them
endif

Figure 3.15: The EXTENDED_SOURCE recipe is used to reduce observations made with a single pair of pointings: one on the object and one on the sky. A variant called EXTENDED_SOURCE_NOSTD is also available. This omits division by a standard star and flux calibration.

Again the variance arrays are added, the slices are located and extracted and the frame is flat-fielded. If the observation is the first in a pair then this is the end of the reduction of this frame. If the frame completes a pair then the sky frame is subtracted from the object frame in the same way as for the standard star and the sky. The sky-subtracted frame is then wavelength calibrated and coadded to the group file which is formed into a datacube.

The sequence described above is certainly not the only sequence in which these operations could be carried out. It would, for example, be possible to form each sky subtracted frame into a datacube before adding it to a group datacube, rather than adding the 2-d sky subtracted frame to a group 2-d frame then forming that into a datacube. For the purposes of assessing the observations as soon as possible it is useful to have a coadded 2-d frame because, although it is hard to visualise the morphology of the emission, this is where it is easiest to see by eye whether a signal is being detected as the signal to noise ratio increases.

3.7.1 Flux calibration

The datacube is divided by the exposure time to give a measurement in counts/sec and then divided by the standard star spectrum (which has already been normalised to an exposure time of 1 second and divided by an appropriate black-body spectrum). This accounts for variations in the transmission of the atmosphere, telescope and instrument as a function of wavelength. The resulting datacube gives the ratio of the flux reaching each pixel to the flux from the standard-star at the centre of the wavelength range. The magnitude of the star in the appropriate band of the spectrum is derived using the V-magnitude and spectral type retrieved from the Simbad database and this is used to calculate the flux from the standard-star. Multiplying the datacube by this flux gives a flux calibrated datacube.

3.7.2 Displaying images and spectra

Images and spectra are displayed during the reduction. A spectrum is produced by taking the mean over a 3.3 × 3.3 arcsec square region in the centre of the field of view. A 'white-light' image will be created from the datacube with the suffix `_im` by com-

pressing the datacube over its entire wavelength range. Other images can be automatically extracted from the datacube by creating a file in the output data directory with the filename `extract.images`. Each line of this file contains the desired suffix for the file containing the image (without the underscore) and either two or four wavelengths (in microns). If a line contains two wavelengths then an image will be extracted from the cube between those wavelengths. If four wavelengths are given then two images will be extracted and the second will be subtracted from the first. Any lines beginning with # are ignored.

```
# Extract a broad-band K image
K   2.1   2.3
# and a continuum subtracted H_2 1-0 S(1) image
S1  2.1208   2.1228   2.1250   2.1270
```

To display these images it is necessary to edit the `disp.dat` file which configures the ORAC-DR display system, specifying how each image should be displayed.

3.8 Mapping an extended source

Many sources are larger than the 3.3 × 6.0 arcsec field of view of the IFU, and it would frequently be useful to map a larger area using several pointings and then mosaic the observations together into a single datacube. It would also have the additional benefit of removing bad pixels, which is often the primary reason for mosaicing normal imaging observations. Reduction of observations of this type can be carried out using the MAP_EXTENDED_SOURCE recipe, summarised in figure 3.16. The stages of the reduction are carried out in a slightly different order to that used when observations of a single pointing are reduced using the EXTENDED_SOURCE. It is no longer possible to coadd each frame into a 2-d group file, which is then formed into a datacube. Instead, each frame, once it has been sky-subtracted and wavelength calibrated, is formed into a datacube, which is then mosaiced into the group datacube.

When images are mosaiced using ORAC-DR it first attempts to register the frames to one another by locating point sources in each image and measuring the offsets required to produce the best alignment. If this fails because there are too few bright

MAP_EXTENDED_SOURCE

mask bad pixels
add readnoise variance
add Poisson variance
locate slices
extract slices
divide by flat-field
if the frame completes a pair
    subtract sky from object frame
    resample all rows to common wavelength scale
    form the frame into a datacube
    if we are not using the MAP_EXTENDED_SOURCE_NOSTD version of the recipe
        divide by standard star
        divide by exposure time
        flux calibrate
    endif
    convert offsets for base position into x and y pixels and use to set frame origin
    if the group file already exists
        add the frame to the list of files to be included in the mosaic
        form all frames in the group so far into mosaic
    else
        add the frame to the list of files to be included in the mosaic
        copy frame to create new group file
    endif
    extract images and spectra and display them
endif

Figure 3.16: The MAP_EXTENDED_SOURCE recipe is used to reduce observations made using telescope offsets to map a region larger than the IFU field of view.

point sources in the image then the telescope offsets used to produce the mosaic are read from the headers and used instead. When IFU fields are mosaiced there will rarely be enough sources to automatically register one to another and the overlap between the frames will tend to be small, so the telescope offsets are always used. The shift required across and along the slices, Δx and Δy (in pixels), can be derived from the offsets in RA and dec, $\Delta\alpha$ and $\Delta\delta$ (in arcsec), the angle of the UIST image rotator, θ and the pixel scale of the image on the UIST array, s (in arcsec/pixel), assuming a slice width of $2s$.

$$\Delta x = (\Delta\alpha \cos\theta - \Delta\delta \sin\theta)/2s$$

$$\Delta y = -(\Delta\alpha \sin\theta + \Delta\delta \cos\theta)/s$$

These shifts are rounded to an integer number of pixels to avoid yet more resampling of the data. It is therefore recommended that the offsets used are an integer multiple of 0.12 arcsec along the slices and 0.24 arcsec across the slices.

The observations should be made in sky-object pairs, though as before the two frames in each pair can be in either order, so the most efficient pattern is likely to be a object-sky-sky-object sequence. The recipe does not require a particular pattern or number of offsets and it is not required that the same amount of time is spent on each position. Each sky-subtracted pair is processed and added to the mosaic individually. The variance array attached to the datacube accounts for variations in signal to noise ratio over the mosaiced datacube due to variations in total integration time.

3.9 Using these recipes with other IFUs

It should be straightforward to use these recipes to reduce data from other image slicing integral field spectrographs, in the same way as the imaging and spectroscopy recipes are used to reduce data from a number of instruments. All of the UIST specific parameters, such as the number of slices, the order in which they occur on the array, the positions and lengths of the slices, the alignments needed to correctly reconstruct the image and the wavelength calibration are included in calibration files in a UIST subdirectory of the ORAC-DR calibration directory. Generating values for use with a different instrument should be straightforward following the procedures described in

this chapter, in chapter 4 and in Todd [2003]

Chapter 4

On-sky testing of the IFU

In the autumn of 2002 I spent two months in Hawaii commissioning the instrument with Suzanne Ramsay Howat, Chris Davis and Sandy Leggett. During this period I was responsible for carrying out and analysing the measurements needed to test and calibrate the IFU.

Once UIST had been delivered to UKIRT and installed on the telescope it became possible to carry out a number of tests of the IFU which could not easily be done in the laboratory. These included tests of the imaging performance of the IFU and tests at longer wavelengths which would been prevented by saturation of the detector by the room background in the laboratory.

4.1 Image reconstruction

When the output from the IFU is formed into an (x, y, λ) datacube the two-dimensional spectrum from each slice of the IFU becomes a single (y, λ) plane. The x-position of each slice is known because it is determined by the position of the slicing mirror in the slicing plane and we know in what order the slicing mirrors cover the slicing plane, and that they are all the same width and adjacent to one another. The y-position in the datacube is determined by the optical alignment of the IFU and must be calibrated.

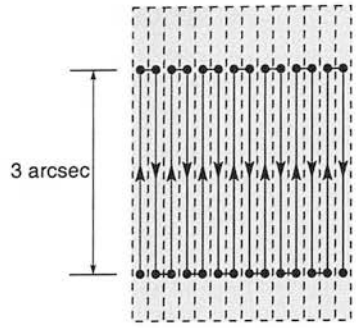

Figure 4.1: An image of a star was moved along and across the field of view of the IFU to determine the alignment of the slices relative to one another and the plate scale of each slice.

4.1.1 Measuring the alignment

The shift which should be applied to each slice in the y-direction was measured using a series of observations in which a star was observed using the IFU and the HK grism and was moved around the field of view by offsetting the telescope, as shown in figure 4.1. Observations were made in pairs, with each pair containing observations offset by 3 arcsec along the slices relative to one another. Between each pair of observations the image was moved across the IFU field of view by 0.24 arcsec (one slice width). One of the frames in each pair was then subtracted from the other to give a positive image of the star at the bottom of the IFU field and a negative image at the top (figure 4.2a). The resulting sky-subtracted frames from all the pairs were then added together. If the alignment of the slices were perfect this would give an (x, λ) plane of positive values across the bottom of the datacube and a plane of negative values across the top. An image was formed by averaging the datacube in the λ dimension (figure 4.2b). From this image it is clear that the initial alignment is far from perfect. The most obvious feature in this image is a discontinuity between the five slices on the left which come from one column of slice images at the output of the IFU and the nine slices on the right which come from the other column. This is likely to be caused by a small vertical offset of one column of reimaging mirrors relative to the other column.

In order to measure the y-offsets which should be applied to the (y, λ) planes of the datacube each column of this image was cross-correlated with all the other columns

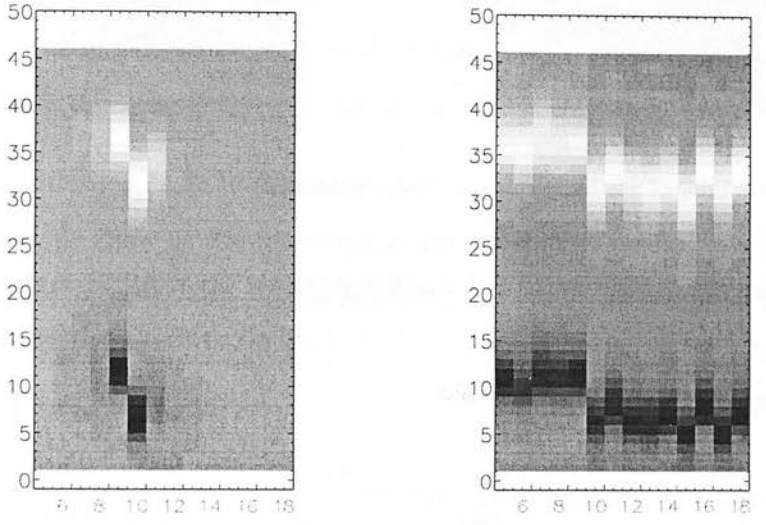

Figure 4.2: (a) Observations were subtracted in pairs, giving a positive and a negative image of the star separated by 3 arcsec. This image shows the poor image reconstruction before the y-offsets were determined. (b) The observations were added together giving a positive and negative line of images across the field of view from which the offset from one slice to another could be measured.

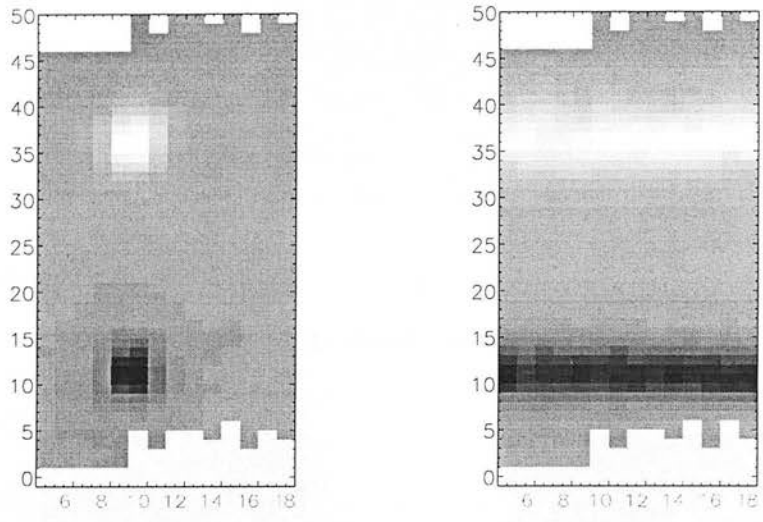

Figure 4.3: After measuring and applying the y-offsets the positive and negative images of the star shown in figure 4.2a are reconstructed accurately and the line of images shown in figure 4.2b is straightened .

in turn, producing a two-dimensional antisymmetric array of measurements:

$$S_{ij} = -S_{ji} = \text{shift of slice } j \text{ relative to slice } i.$$

If slice k is now offset by a_k then a_k is added to every value in the kth row of S_{ij} and subtracted from every value in the kth column. The optimum set of offsets are given by the values of a_k which minimise

$$\alpha = \sum_{i,j} (S_{ij} + a_j - a_i)^2.$$

For each slice the value of α was calculated for values of a_k at intervals of 0.001 pixels and spanning the range of plausible offsets (-6 to $+6$ pixels) to find the position of the kth slice which minimised α. This procedure was carried out for each slice in turn. These offsets were then applied, so $S_{kj} \rightarrow S_{kj} + a_k$ and $S_{ik} \rightarrow S_{ik} - a_k$. The process was repeated until none of the values of a_k were changed by 0.001 pixels or more in a single iteration over all the slices.

Two sets of measurements were made in this way. These two sets of observations were identical except for a 0.50 arcsec offset along the slices to better centre the images of the star. The images in figures 4.2 and 4.3 are taken from this second set. In the first set the peak of the star was very close to the bottom edge of those slices which have large offsets. This does not seem to significantly increase the error on the shifts measured using this data. The r.m.s. difference between the offsets derived from the two sets of observations was 0.13 pixels with a maximum difference of 0.21 pixels for one slice. The error on a single measurement is less than the error on the difference by a factor of $\sqrt{2}$. Using the mean of the two offsets derived for each slice should reduce the error by a further factor of $\sqrt{2}$. We therefore estimate that the r.m.s. error on the derived offsets is 0.07 pixels. The results of the alignment can be seen in figure 4.3.

Comparing the two sets of measurements also allows us to place an upper limit on any systematic drift of the telescope offset. Random errors in telescope offsets will merely contribute to the measurement error which, as we have seen, is small. A systematic drift with a component parallel to the slices would not be visible from a single set of measurements because the effect would be to introduce an additional shear into the misaligned slice positions seen in figure 4.2b, which would then be removed along with the misalignment of the slices.

The two sets of observations were made immediately one after another, maintaining guiding on the target throughout. No changes were made between the two sets of observations except a 0.50 arcsec offset of the telescope along the slices. In the absence of any drift of the telescope parallel to the slices there should be a constant 0.50 arcsec (4.17 pixel) offset between the positions in the two sets of measurements. A constant drift with a component parallel to the slices would produce a larger or smaller offset. The shift in position of the positive and negative images between the two sets of observations was measured for each slice. The mean shift was found to be (4.18 ± 0.04) pixel, or (0.497 ± 0.005) arcsec (using the plate scale of 0.119 arcsec/pixel, the measurement of which is described below), so drift of the telescope offset over the period of making these measurements was, therefore, less than ± 0.05 pixel over the course of making each set of measurements (at the 1σ certainty level). This would be insignificant when reconstructing images: it would correspond

to shearing the image so that one edge was offset by less than 0.05 pixel along the slices relative to the opposite edge, which would be a smaller effect than the random error in aligning the slices.

4.1.2 Measuring the plate scale

The observations made to determine the offsets required for accurate image reconstruction also allowed us to determine the plate scale along each slice of the IFU. An image extracted from the sum of all the observations, as shown in figure 4.3b was used. Gaussian profiles were fitted to the positive and negative images on each slice to determine the separation of the peaks in pixels, known to correspond to 3 arcsec on the sky. These measurements were made using both sets of observations mentioned in the previous section. There were three slices for which only one measurement could be made because the positive peak was on the edge of the field of view of the IFU in one set of observations. Having two sets of measurements allows us to make an estimate of the error on the measurements. The r.m.s. difference between the two measurements of the plate scale of a given slice was 1.0×10^{-3} arcsec/pixel. This is the error in the difference between two measurements, so the error on a single measurement is 7×10^{-4} arcsec/pixel, $\sqrt{2}$ times smaller. Taking the mean of two measurements (where available) reduces the error by another factor of $\sqrt{2}$ to 5×10^{-4} arcsec/pixel. The results of these measurements are shown in figure 4.4.

There appears to be a small change in plate scale at the right hand side of the field of view of $\sim$ 2.5%, corresponding to a difference of $\sim$ 1 pixel over the length of the IFU. This is just visible in figure 4.3b, where the lines diverge slightly on the right hand side of the image. The variation in plate scale from one slice to another will be irrelevant in virtually all cases due to the small field of view. Taking the mean over all slices gives a mean plate scale of 0.119 arcsec/pixel with an r.m.s. deviation of 0.001 arcsec/pixel.

4.1.3 The effect of changing grism on the image reconstruction

Initially it was assumed that the relative positions of the slice images on the array would be constant because the optics of the IFU are entirely reflective. It is now be-

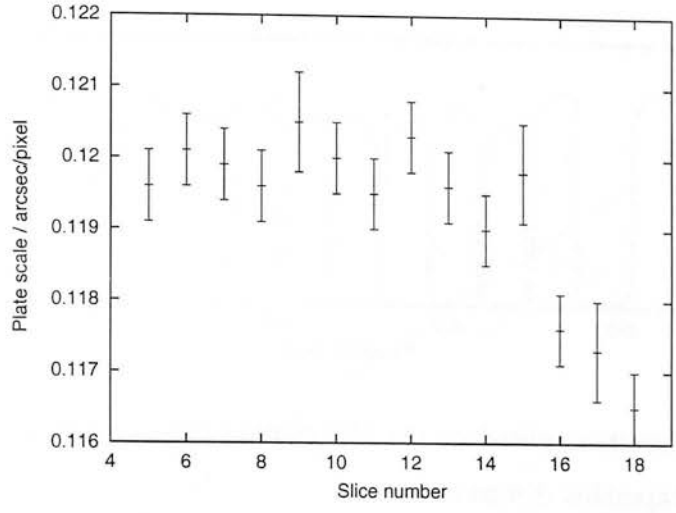

Figure 4.4: The plate scale of each slice of the IFU was measured by measuring the distance between the positive and negative image on each slice in the image shown in figure 4.3b.

lieved, however, that the surfaces of some of the grisms are slightly curved. One effect of this is to significantly shift the optimum position of the focus mechanism. A second effect is to slightly magnify or demagnify the image formed on the array. The change in magnification is very small ($\sim 0.1\%$) and is insignificant in long-slit spectroscopy modes, but it is significant for IFU observations. The primary effect of this magnification on an IFU observation is to change the relative positions of the slices on the array (it also changes the plate scale on each slice but this is, if anything, even less significant than for long-slit spectroscopy due to the small field of view). Slices at opposite ends of the array will be shifted by ~ 1 pixel relative to each other, so if the relative positions are assumed to be fixed the (y, λ) planes of the datacube will be shifted in the y direction by ~ 1 pixel relative to each other. This effect is made more obvious by the order in which the slices are arranged: slices adjacent to one another at the edge of the field of view are at opposite ends of the array.

The magnification introduced by each grism was measured using an IFU flat-field spectrum for each grism. The magnification was measured relative to that of the *HK* grism because the alignment had been determined for the *HK* grism, and this would allow us to generate a correction for each grism. The raw IFU flat-field frame was divided by an imaging mode flat-field to remove variations in intensity due to the

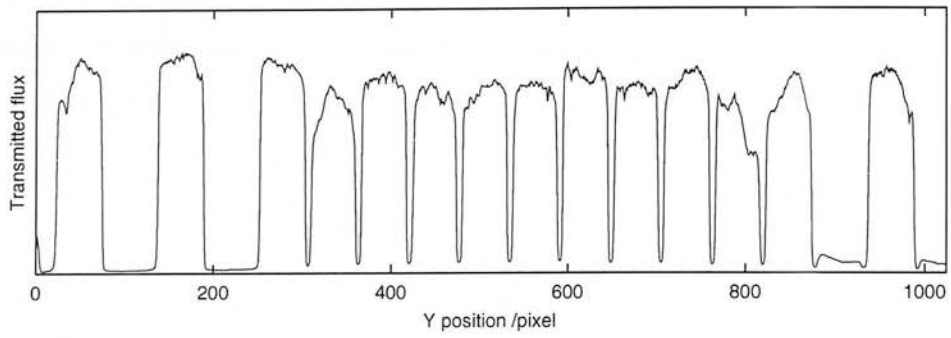

Figure 4.5: The flux transmitted by the IFU plotted against y-position on the array averaged in the dispersion direction.

sensitivity of the array. The 2-d frame was then collapsed in the x-direction, excluding points more than 5σ from the mean in order to exclude bad pixels. This created a 1-d profile giving the positions of all the slices for a given grism, as shown in figure 4.5. Each profile was approximately aligned to that of the *HK* grism using a shift of an integer number of pixels. The position of each slice within the profile was then measured relative to the position of the same slice in the profile of the *HK* grism using cross-correlation over the length of the slice plus six pixels at each end.

If a spectrum is magnified relative to that of the *HK* grism then plotting the offset of each slice against the y-position of the slice on the array will give a straight line with gradient m. The magnification factor is given by $m + 1$, so a positive gradient corresponds to a magnification and a negative gradient corresponds to a de-magnification. The magnification factor for each grism was obtained by fitting a straight line to the data from each grism using a least-squares fit. The measurements made using the long-J grism (showing strong evidence of magnification) and short-H grism (no evidence for magnification) are shown in figure 4.6. The results from all grisms are summarised in table 4.1.

4.2 Point source image quality

The observations described in the previous section were made at a time when the seeing was very good. Individual pairs of observations from this series are therefore ideal for examining the point source image quality of the IFU. Stellar images were

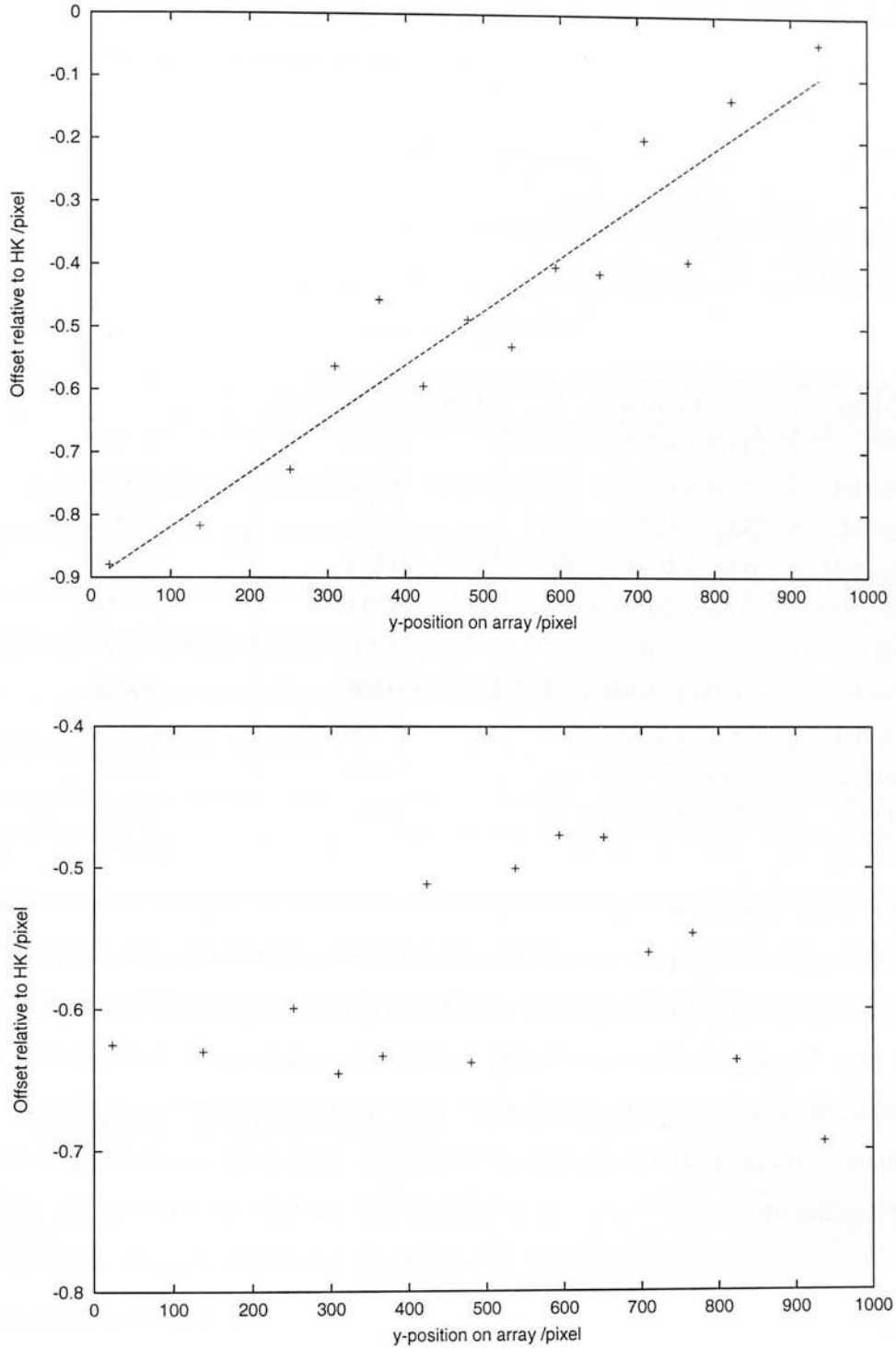

Figure 4.6: The shift in position of each slice image on the array is clearly correlated with position on the array when the *HK* grism is replaced with the long-*J* grism (top), indicating that the 2-d spectrum formed on the array using the long-*J* grism is magnified relative to that formed by the *HK* grism. When the short-*H* grism is compared to the *HK* grism (bottom) there is no significant correlation.

Grism	Gradient	Correlation coeff.	r.m.s. residual /pix
IJ *	$(5.43 \pm 0.74) \times 10^{-4}$	0.911	0.070
short-*J*	$(7.25 \pm 0.68) \times 10^{-4}$	0.950	0.066
long-*J*	$(8.61 \pm 0.85) \times 10^{-4}$	0.946	0.082
short-*H*	$(0.40 \pm 0.75) \times 10^{-4}$	0.136	[0.068]
long-*H* *	$(0.63 \pm 0.60) \times 10^{-4}$	0.314	[0.046]
HK	0	n/a	n/a
short-*K* *	$(-1.56 \pm 0.50) \times 10^{-4}$	-0.688	0.042
short-*L*	$(-0.60 \pm 1.14) \times 10^{-4}$	-0.151	[0.102]
long-*L* *	$(1.68 \pm 0.53) \times 10^{-4}$	0.691	0.051
M *	$(-0.97 \pm 0.47) \times 10^{-4}$	-0.527	0.045

Table 4.1: The magnification of the 2-d spectrum produced by a given grism relative to that produced by the *HK* grism is given by (1+gradient). The measurements from several grisms (marked with *) contained one or two points lying more than 4σ from the best fit line. These points were excluded and the line recalculated. Grisms for which the correlation coefficient was less than 0.4 were assumed to have a gradient of zero and the r.m.s. residual shown (in square brackets) is simply the standard deviation of the measurements.

fitted using the **psf** routine of the Starlink KAPPA package. This finds the centre of the star and the ellipticity and fits a function of the form

$$D = A \exp\left[-\frac{1}{2}\left(\frac{r}{\sigma}\right)^{\gamma}\right] \tag{4.1}$$

where r is calculated from the true radial distance from the star centre allowing for image ellipticity. When $\gamma = 2$ this function is a Gaussian. The full-width half-maximum (FWHM) of the peak can be calculated from σ and γ.

Both the positive and the negative image in each of 26 pairs of frames was fitted in this way (figures 4.7 and 4.8). The FWHM seeing was found to have a mean of 0.418 arcsec along the minor axis with a standard deviation of 0.076 arcsec. The mean major to minor axis length ratio was 1.148 with a standard deviation of 0.196 with the major axis always parallel to the slices. The mean value of γ was 1.69 with a standard deviation of 0.17. None of these parameters showed any significant trends correlated with the position of the stellar image in the field of view.

It is not possible to separate the contribution of the IFU to the PSF from the effects of seeing, the telescope and the rest of the UIST optics without having images of a star in the same seeing conditions made using UIST in imaging mode. We can, however, say from these measurements that the point source image quality of the IFU is very high both parallel and perpendicular to the slices and that there is no evidence of variation of the PSF across the field of view.

4.3 Measuring the throughput using observations of stars

When a star is observed with the IFU the signal at a given pixel of the rearranged IFU frame, (x, y), or equivalently (λ, y), where the mapping from x to λ depends on the grism used, is given by:

$$S_{\mathrm{IFU}}(x, y) = F(\lambda, y)\, T(\lambda, y)\, \alpha(x, y)$$

where $F(\lambda)$ is the flux from the star, $T(\lambda, y)$ is the transmission of the IFU and $\alpha(x, y)$ is the sensitivity of the detector array.

The signal detected at pixel (x, y) when the slit is used is given by

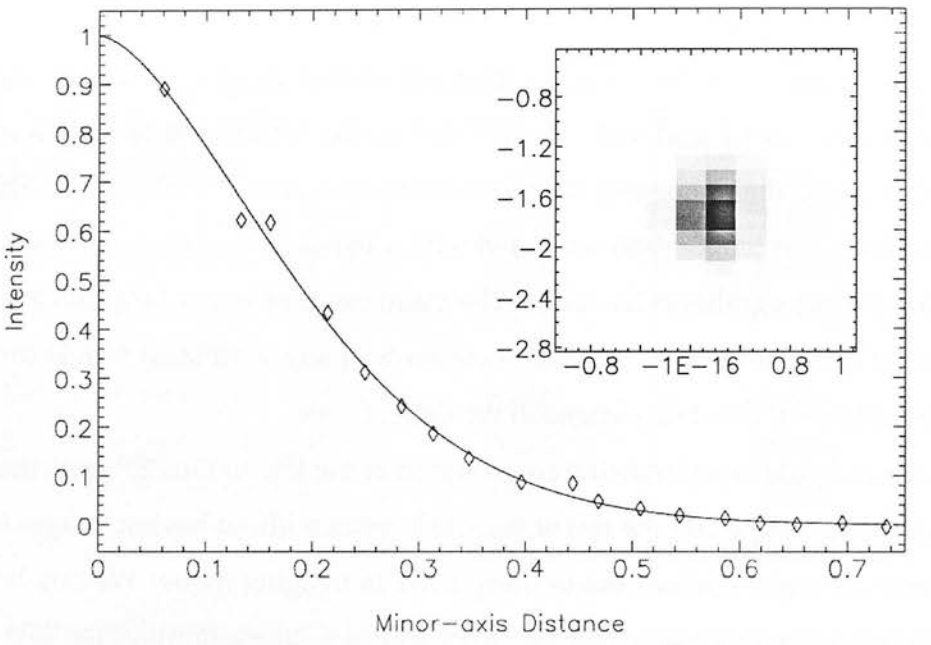

Figure 4.7: The point spread function was measured by fitting equation 4.1 to images of a star. One such image is shown here with axes labeled in arcsec offsets from the centre of the field of view of the IFU. The graph shows the intensity of the image, normalised to have a peak value of one, as a function of radial distance in arcsec taking ellipticity into account. The curve is the best fitting model for this image, with $\gamma =$ 1.61 and FWHM seeing of 0.37 arcsec along the minor axis. The ratio of major to minor axis length was 1.28.

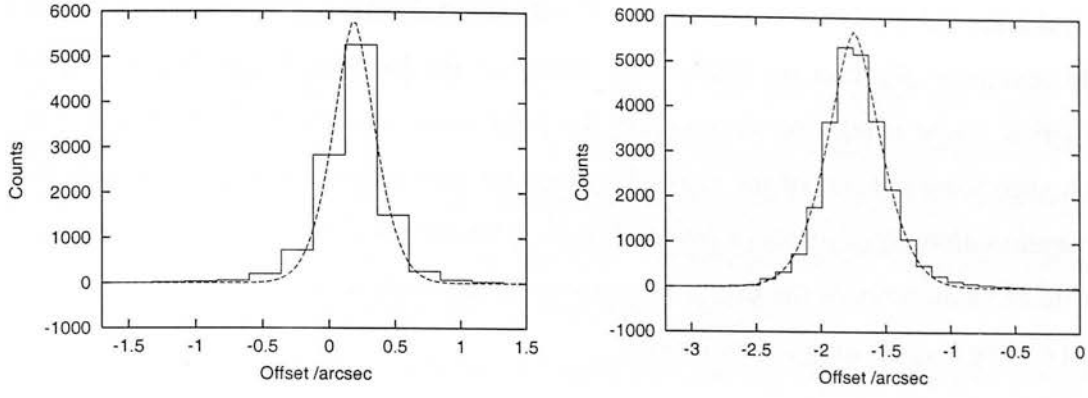

Figure 4.8: Cuts through the stellar image shown in figure 4.7 in the x-direction (left) and y-direction (right). The dotted line shows a function of the form of equation 4.1 using the parameter values described in the caption to figure 4.7. This gives a FWHM of 0.37 arcsec in the x-direction and 0.47 arcsec in the y-direction.

$$S_{\text{slit}}(x, y) = F(\lambda, y)\, \alpha(x, y)\, \beta(\lambda)$$

where $\beta(s)$ is the proportion of the stellar PSF transmitted by the slit, which is a function of the seeing, which will vary with wavelength.

Using a set of measurements of $S_{\text{IFU}}(x, y)$ and $S_{\text{slit}}(x, y)$ we want to calculate the average of $T(\lambda, y)$ over all values of y, $T_\lambda(\lambda)$, which we can then compare to the values measured in the laboratory using the argon and halogen lamps, as described in section 2.6.4.

4.3.1 Flat-fielding the frame

When measuring the transmission using observations of stars it is necessary not only to account for variations in sensitivity of the array but also for variations of the transmission of the IFU over the field of view. This ensures that the derived transmission will not depend on the location of the star in the field of view, and allows us to measure the average transmission over the field of view of the IFU.

The pixel-to-pixel and larger scale variations in sensitivity of the array and the variation in T with y can be removed by constructing a flat-field frame which includes these variations but contains no information about the spectrum of the source used

to make the flat-field or the variation of T with λ. To do this a conventional IFU flat-field spectrum of either the black-body source or the halogen lamp (depending on the grism being used) and an imaging flat-field were combined. The spectra from each slice were cut out of the flat-field spectrum and approximately aligned in the dispersion direction, creating a frame $A(x, y)$. Each row of this image was divided by the mean of all rows of the image to remove the dependence on the spectrum of the light source use, creating a new frame:

$$B(x, y) = \frac{A(x, y)}{\sum_y A(x, y)/n_y}.$$

This image contains information about pixel-to-pixel variations in sensitivity of the array and the variation of transmission of the IFU with y at each wavelength and large scale variations in sensitivity of the array with y, but includes no information on large scale variations of α in the dispersion direction. This information was obtained using the imaging flat-field. The same regions of the imaging flat-field as had been extracted from the IFU frame were then extracted and shifted in exactly the same way. A one-dimensional image was created from this containing the mean over all y values $C(x)$. All rows of $B(x, y)$ were then multiplied by $C(x)$ to give a final flat field:

$$F_{\mathrm{IFU}}(x, y) = \frac{A(x, y)}{\sum_y A(x, y)/n_y} \times C(x).$$

Dividing our original image by this flat field gives us:

$$\frac{S_{\mathrm{IFU}}(x, y)}{F_{\mathrm{IFU}}(x, y)} = F(\lambda, y) T_\lambda(\lambda).$$

Extracting the stellar spectrum from this image either by simply coadding all rows or by optimal extraction (as described in section 3.6.2) gives us a spectrum which is the product of the flux of the star and the transmission of the IFU as a function of wavelength.

Similarly a flat-field was generated for the slit spectrum by dividing every row of a spectrum of either the black-body source or the halogen lamp by the average spectrum over all rows to remove the shape of the spectrum and multiplying by the average over all rows of the imaging flat-field to restore information about variations in sensitivity of the array in the x-direction.

4.3.2 Compensating for slit-losses

When the two-pixel slit (0.24 arcsec wide on the sky) is used a significant fraction of the light from a point source falls outside the slit and is lost, particularly when the seeing is poor. When the IFU is used all the flux is collected unless it falls outside the field of view of the IFU. In order to obtain a measurement of the transmission of the IFU it is necessary to compensate for the flux lost by the slit.

If the distribution of flux from a point-source is given by $\psi(x, y)$ then the proportion of flux transmitted by a slit of width $2w$ and assumed to be infinite in length is given by

$$f = \frac{\int_{-\infty}^{+\infty} \int_{-w}^{+w} \psi(x, y)\, dx\, dy}{\int_{-\infty}^{+\infty} \int_{-\infty}^{+\infty} \psi(x, y)\, dx\, dy} \tag{4.2}$$

If we assume that the PSF is gaussian, so $\psi(x, y) = Ae^{-(x^2+y^2)/2\sigma^2}$ then this is a separable function $\psi(x, y) = A \times e^{-x^2/2\sigma^2} \times e^{-y^2/2\sigma^2}$ so the proportion of the light transmitted is given by

$$f = \frac{1}{\sigma\sqrt{2\pi}} \int_{-w}^{+w} e^{-x^2/2\sigma^2}\, dx \tag{4.3}$$

This integral cannot be evaluated analytically. Results of numerical integration are shown in figure 4.9. Note that this plot shows f as a function of the FWHM seeing, which is given by 2.355σ. When $\sigma \gg 2w$ (i.e. when the seeing is poor) ψ is approximately flat over the range $x = -w$ to $+w$ and equal to the peak height of the gaussian, so $f \approx \frac{2w}{\sigma\sqrt{2\pi}}$ or $1/f \approx 4.435s$, where s is the FWHM seeing, as shown in figure 4.10. From these figures we see that f varies rapidly with s over the range of typical values for the seeing at UKIRT (generally ~ 0.4 to ~ 1.0 arcsec), so accurate measurements of s are vital if we are to correct for the slit-losses.

Further flux is lost if the star is not centred on the slit. The effect of this is shown in figure 4.11 for seeing of 0.4 arcsec and 0.8 arcsec. We have no way of measuring this offset, and hence compensating for it.

In order to measure the slit losses it was assumed that the PSF was circularly symmetric. The PSF is better described by equation 4.1 with $\gamma \sim 1.6$ than by a gaussian. As shown in figure 4.12, such a PSF can equally well be described by the sum of two Gaussian profiles.

$$\psi(r) = A\left(\phi \exp\left[-\frac{1}{2}\left(\frac{r}{\sigma_a}\right)^2\right] + (1-\phi)\exp\left[-\frac{1}{2}\left(\frac{r}{\sigma_b}\right)^2\right]\right).$$

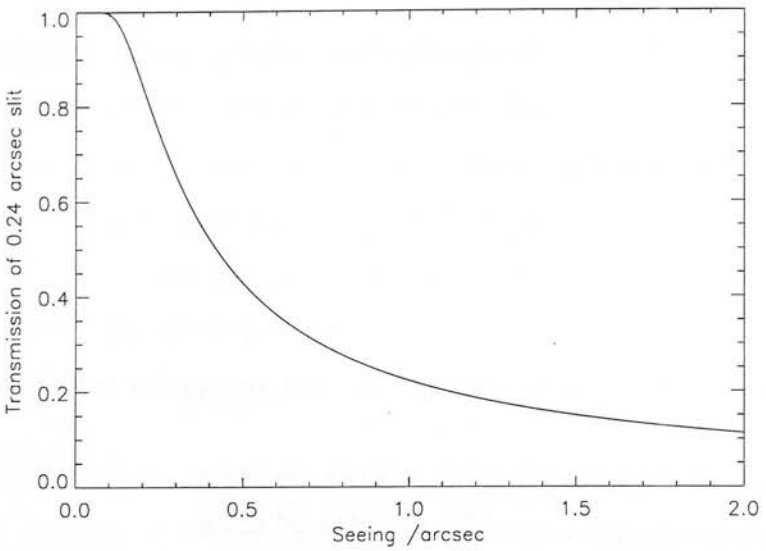

Figure 4.9: This graph shows the proportion of flux from a gaussian PSF centred on the slit transmitted by a 0.24 arcsec wide slit as a function of FWHM seeing.

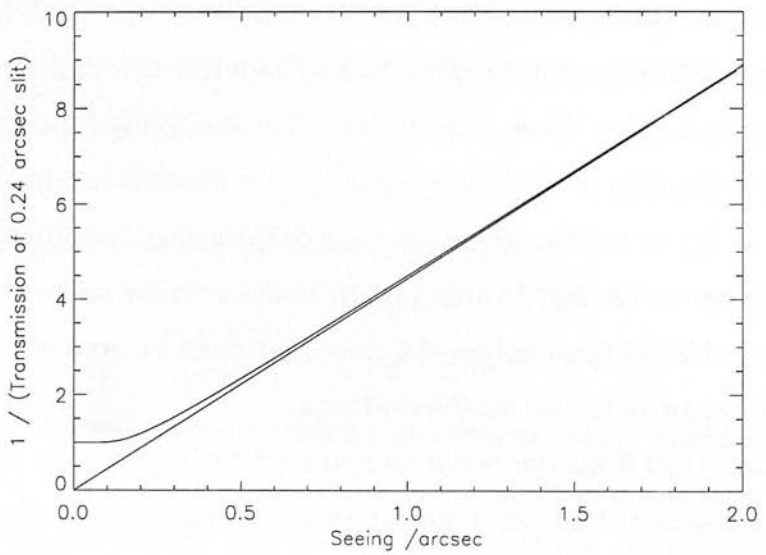

Figure 4.10: This is the inverse of the function plotted in 4.9. This shows how much more flux would be transmitted by a perfectly transmitting IFU (assuming that the field of view of the IFU is significantly larger than the seeing) than by a 0.24 arcsec slit as a a function of FWHM seeing. The straight line has a gradient of 4.435. The curve approaches this line asymptotically as the seeing increases.

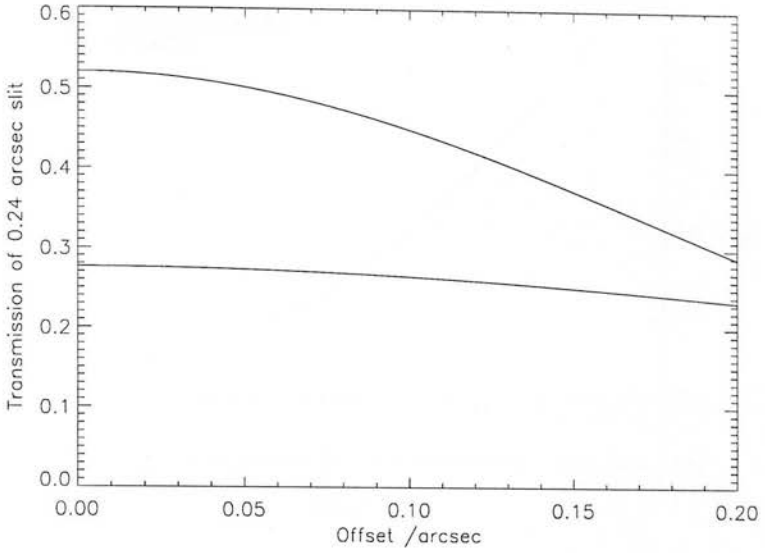

Figure 4.11: The variation of transmission of a 0.24 arcsec wide slit as a point source image is offset from the centre of the slit for 0.4 arcsec FWHM seeing (top line) and 0.8 arcsec FWHM seeing (bottom line).

The PSF was measured at 32 wavelengths for each grism, each obtained by averaging over 32 columns of the image. Two Gaussian profiles were then fitted to this profile and the fraction of light lost was calculated. This was then used to compensate for the slit losses and calculate the total flux from the star.

4.3.3 Results

One dimensional spectra were extracted from the IFU frame and from the long-slit spectrum with compensation for slit losses as described above. Both spectra were divided by the exposure time to obtain a normalised flux. The transmission of the IFU was then given by dividing the spectrum from the IFU by the spectrum from the long-slit producing a transmission spectrum. The transmission was measured over a number of wavelength ranges within the transmission spectrum by averaging over regions of good atmospheric transmission. The transmission measurements made using the *HK*, short-*L*, long-*L* and *M* grisms are shown in figure 4.13. The dotted line shown in this plot is the curve shown in figure 2.19. Each point shown has two error-bars. The bold error-bars centred on the data point show the random error estimated by the

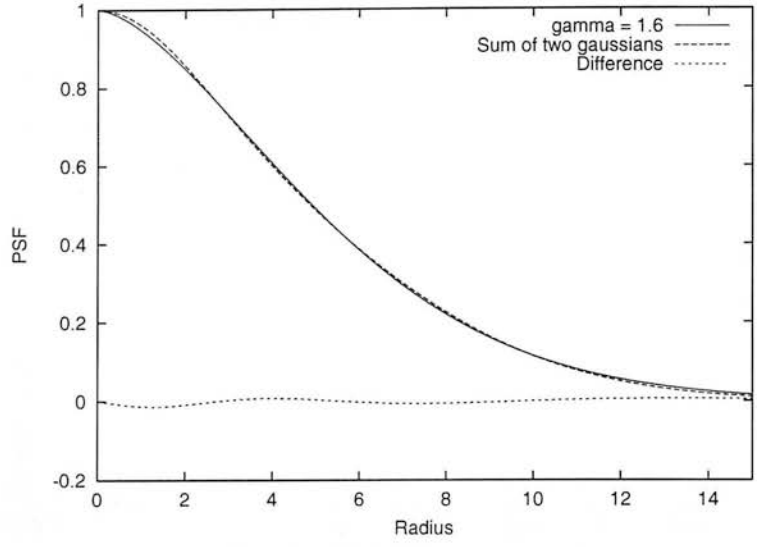

Figure 4.12: The PSF function given in equation 4.1 can be well approximated by the sum of two Gaussian functions. This plot shows two curves: one is described by equation 4.1 with $\gamma = 1.6$ and $\sigma = 4$ and the other is the sum of two Gaussian profiles with $\sigma_a = 2.12$ and $\sigma_b = 5.15$. The difference between the two curves is also plotted.

scatter of transmission values within the region averaged over to obtain the value. The much larger error bars extending further below each data point than above it show the estimated 1σ error that would be seen due to incorrect compensation for slit losses due to ellipticity of the point spread function or errors in centering the star on the slit. From UIST images it was found that the mean ratio of the maximum to minimum radius of the point spread function was 1.10 with r.m.s. deviation of 0.06. From this and from the curve shown in figure 4.9 the uncertainty due to the ellipticity of the stellar images was estimated to be $\pm 10\%$. If we assume that the star was centred on the slit to an accuracy of 0.1 arcsec then the transmission would be overestimated by up to $\sim 10\%$ in 0.6 arcsec seeing. Assuming no correlation between these two effects then these combine to give an error of $+7\%/-14\%$. These errors should, perhaps, be considered as systematic errors rather than random errors. Correlation would certainly be expected between the errors on the measurements made with a single grism because neither effect is expected to vary strongly with wavelength. There is also likely to be correlation between the errors due to the ellipticity of the point spread function on consecutive observations.

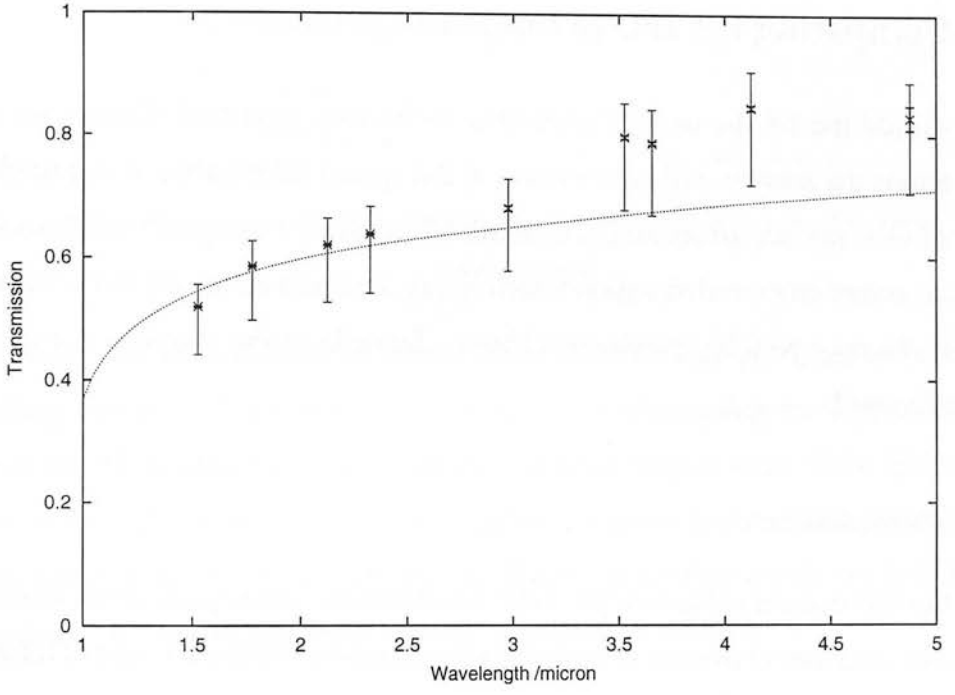

Figure 4.13: The transmission of the IFU measured from stellar spectra. The dotted line is given by equation 2.5 using the parameter values found by fitting the curve as described in section 2.6.4. The significance of the two sets of error bars is explained in the text.

These measurements are consistent with the transmission measurements made using the halogen and argon lamps in the calibration unit described in section 2.6.4. The large uncertainties on the measurements shown here do not allow us to refine the previous fit of equation 2.5. These new measurements extend to longer wavelengths than those made in the laboratory and reassure us that there are no significant unexpected losses in the IFU at longer wavelengths.

4.4 Comparing the IFU to long-slit spectroscopy

When should the IFU be used in preference to the two pixel slit? Clearly for some observations the answer will be obvious – if 2-d spatial information is required over a field of view several arcsec across then the IFU is ideal, whereas if variations in the spectrum across an extended region which is, say, 1 arcmin across are to be measured then the slit may well be the obvious choice. Sometimes the choice is not quite so straightforward.

4.4.1 Point sources

Using the IFU instead of the two pixel slit maintains the same spectral resolution and eliminates slit losses at the cost of the reduced transmission of the IFU and of offsetting to the sky rather than along the slit. When the seeing is sufficiently poor the advantages can outweigh the disadvantages. Figure 4.14 shows the time taken to reach a given signal to noise ratio on a point source using the IFU relative to the time taken using the two pixel slit taking both the IFU transmission and slit losses into account and including a factor of two due to the need to offset to sky when using the IFU rather than offsetting along the slit. Figure 4.15 shows the critical values of the seeing at which it becomes quicker to use the IFU rather than the slit as a function of wavelength. From these plots it can be seen that it is never significantly quicker to use the the IFU if the seeing is better than 0.7 arcsec. It is also virtually never an improvement in the J and H bands. In the K band it would be quicker to use the IFU if the seeing is worse than 0.75 arcsec. At a wavelength of 2.2 μm with seeing of 0.8 arcsec the time taken to reach a given signal to noise ratio with the IFU would be 0.8 times the time

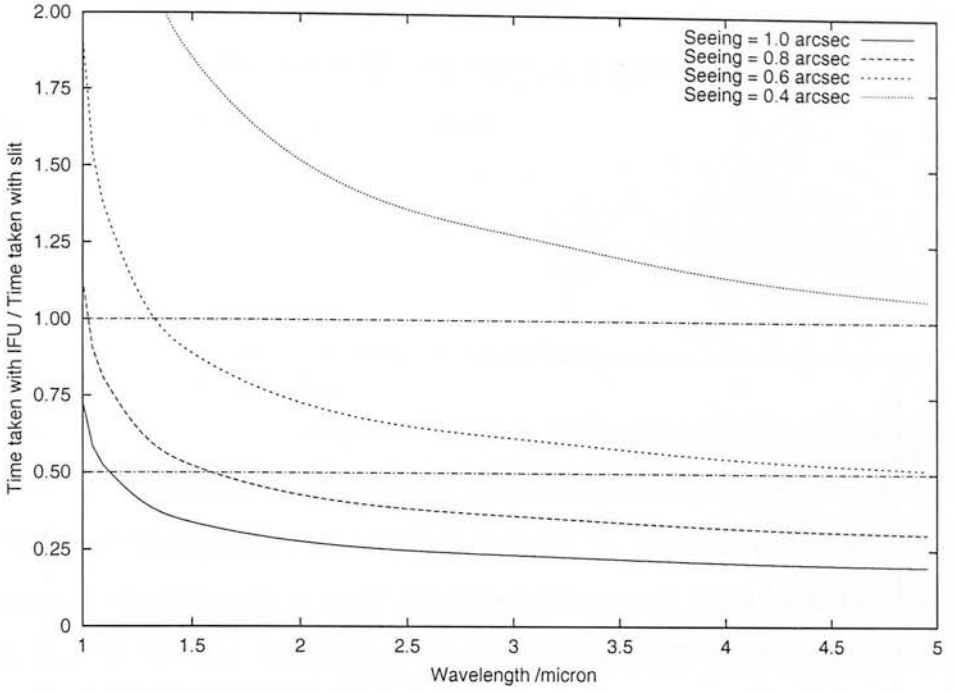

Figure 4.14: The ratio of time on source taken to reach a given signal to noise ratio observing a point source using the IFU to the time taken using the 2 pixel slit. The effect of the IFU transmission and slit losses are taken into account. If the IFU is offset to sky for sky subtraction then all points below the lower horizontal line (ratio = 0.5) are quicker with the IFU than with the slit. If the star is offset within the IFU then all points below the upper line (ratio = 1) are quicker with the IFU.

taken with the slit, and with a seeing of 1.0 arcsec it would take about half the time.

The IFU also provides greater photometric accuracy than the slit. When the slit is used variations in seeing between observing the standard-star and the target or small offsets from the centre of the slit lead to errors in photometry, as illustrated by section 4.3.3. There is also no time taken in peaking-up on the target when the IFU is used, increasing observing efficiency if a large number of targets are to be observed for a short time.

The IFU could be still faster relative to the slit if, rather than offsetting to sky, the source is shifted along the long axis of the IFU field of view, in the same way as one would use a long-slit. This would make the IFU faster than the 2 pixel slit under all but the best seeing conditions. This gain would, however, have to be balanced against

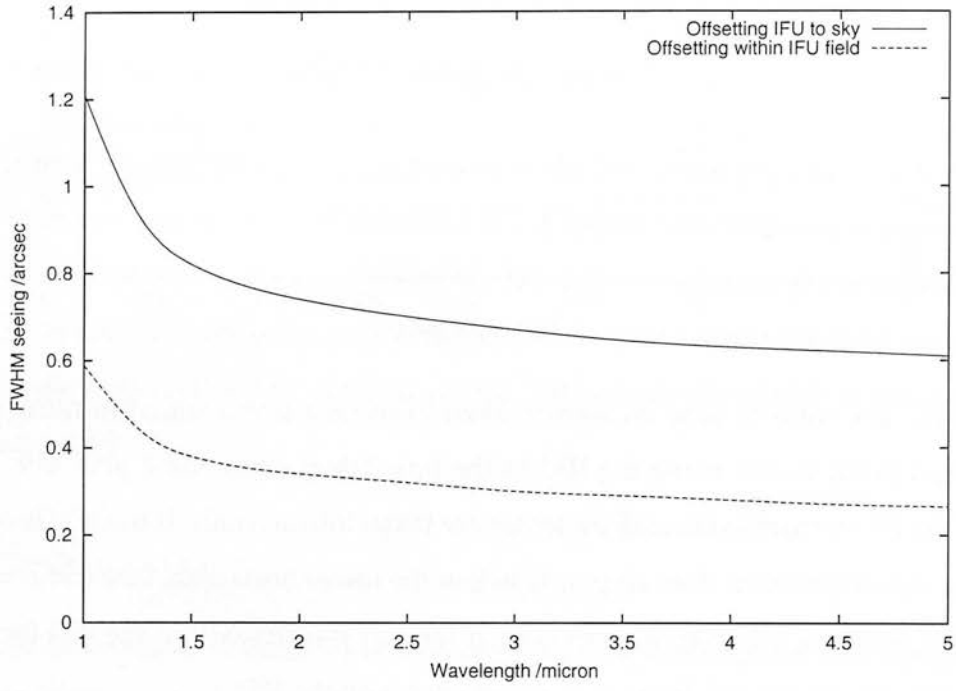

Figure 4.15: This shows the FWHM seeing at which it would take the same time to reach a given signal to noise ratio using the IFU or the slit taking into account IFU transmission and slit losses. If the IFU is offset to sky for sky subtraction then for points above the upper line the IFU will be quicker and for points below the line the slit will be quicker. If the source is offset within the field of the IFU then the IFU will be quicker for all points above the lower line.

the potential reduction in photometric accuracy due to the overlap of the positive and negative images and the increased time taken in acquiring the target with sufficient accuracy to allow this technique to be used.

4.4.2 Extended sources

When extended source are observed slit-losses are irrelevant, so reaching a given signal to noise ratio on each pixel will always take longer with the IFU than with the slit, particularly if the region is sufficiently compact to avoid having to offset to a separate sky position when the slit is used. However, sometimes it may still be worth using the IFU rather than the slit even when information about spatial variations are not required. If spatial variations are negligible over the scale of the IFU (6 arcsec) then it may make sense to average over some or all of the 650 spatial pixels of the IFU, increasing the signal to noise ratio by a factor of up to 25, assuming that the observations are background limited. It is unlikely to make sense to average over 650 pixels along the slit. When the average spectrum from 50 pixels (6 arcsec) along the slit is formed this only increases the signal to noise by a factor of 7, so there could be a significant advantage in using the IFU instead of the slit, particularly if it is necessary to offset to sky when using the slit.

The time advantage of using the IFU to map a source rather than scanning a 2 pixel long-slit across the source to obtain the same spectral resolution and signal to noise ratio is greatest when the source is roughly the size of the IFU field of view. In this case there is a choice between using a single IFU position or 14 slit positions. Even taking into account the transmission of the IFU and the time taken to offset to sky with the IFU, which is not required with the slit, the IFU is five times faster than the slit. If the source is smaller and requires fewer slit positions the time advantage will be smaller, but scanning the slit will always have the disadvantage of being affected by changes in the sky transparency and seeing during the observation. Similarly if the source is sufficiently extended to require two or more IFU fields to be placed end-to-end then the ratio of slit positions to IFU positions is decreased.

4.5 Mapping an extended source

The capabilities of the IFU and the data reduction software were demonstrated by observing a 6.5 × 14.2 arcsec^2 region of the bright planetary nebula NGC 7027 with the *HK* grism. Six IFU pointings were used which were mosaiced together into a single datacube by the ORAC-DR recipes. Images extracted from the resulting datacube are shown in figure 4.16. Spectra were extracted from two 1 × 1 arcsec regions of the datacube: one from the region with the brightest continuum emission (figure 4.17)and one from the region with the brightest H_2 emission (figure 4.18), both on the top edge of the bright ring seen the the images in figure 4.16. The spectral lines detected in these spectra are shown in tables 4.2 and 4.3.

In the continuum and Brackett-γ the dense inner envelope, ionised by the hot central star is seen. In the H_2 image emission from the neutral outer envelope is seen. This emission has a complex morphology with four-fold symmetry, as seen in the images shown by Cox et al. [2002], who obtained velocity maps of the Brackett-γ and H_2 emission using the BEAR imaging fourier transform spectrograph (FTS) on the Canada-France-Hawaii Telescope (CFHT). They argue from their data that the complex morphology of the H_2 emission can best be explained either by simultaneous multiple bipolar outflows from the central star or by a single episodic bipolar outflow along an axis which precesses or wobbles.

These observations clearly demonstrate the power of the IFU. This datacube was constructed from six pointings, each of which was observed for 288 sec on source, taking a total of 1 hour to observe the entire mosaic including offsets to sky. As discussed in section 4.4.2, mapping a large source like this the speed advantage of the IFU over scanning a long-slit across the source is smaller than that seen for mapping sources sufficiently compact to fit within a single IFU field, however it is still quicker. To map this area at the same signal to noise ratio and spectral resolution using a long-slit it would be necessary to use 27 positions of the 2 pixel slit to cover the 6.4 arcsec wide field. Taking into account the transmission of the IFU at *H* and *K* ($\sim$ 0.6) it would be necessary to spend 220 sec on source for each slit position to reach the same signal to noise ratio as we have obtained in 288 sec with the IFU. There would be no need to offset to sky – the source is compact enough to fit within the 2 arcmin slit – so the total

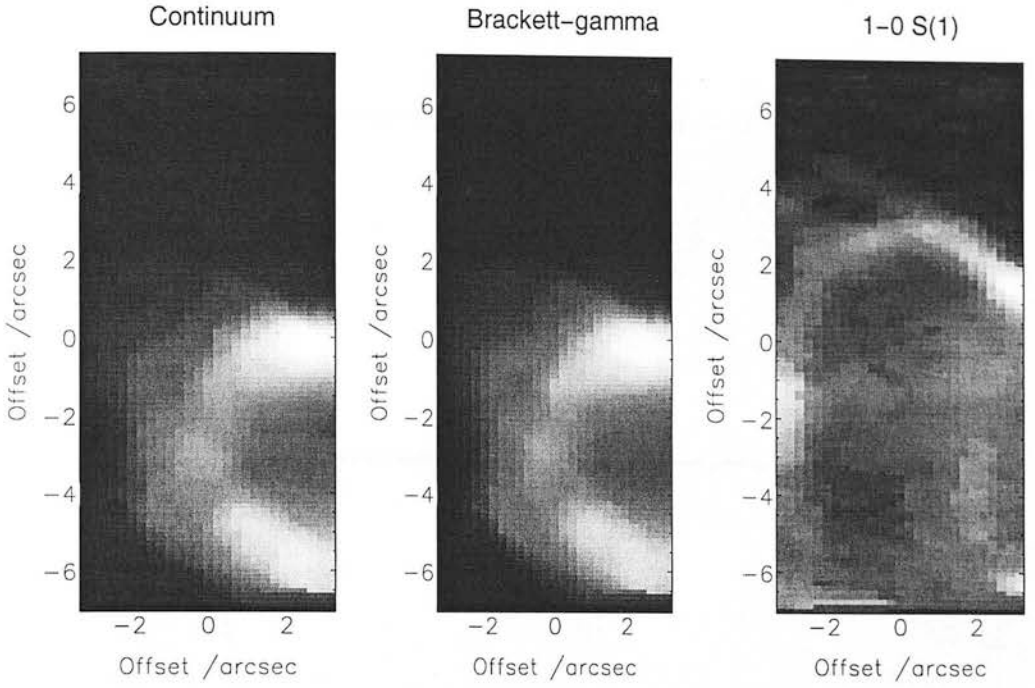

Figure 4.16: Images of the planetary nebula NGC 7027 extracted from the datacube formed by mosaicing six IFU pointings. (a) *K*-band continuum image, (b) continuum subtracted Brackett-γ image, (c) continuum subtracted H_2 $1-0$ S(1) image.

observing time would be 220 s $\times$27 positions, or 1.7 hours. Mapping the source with the IFU also allowed an overlap between adjacent positions so that variations in sky transmission could be measured and corrected.

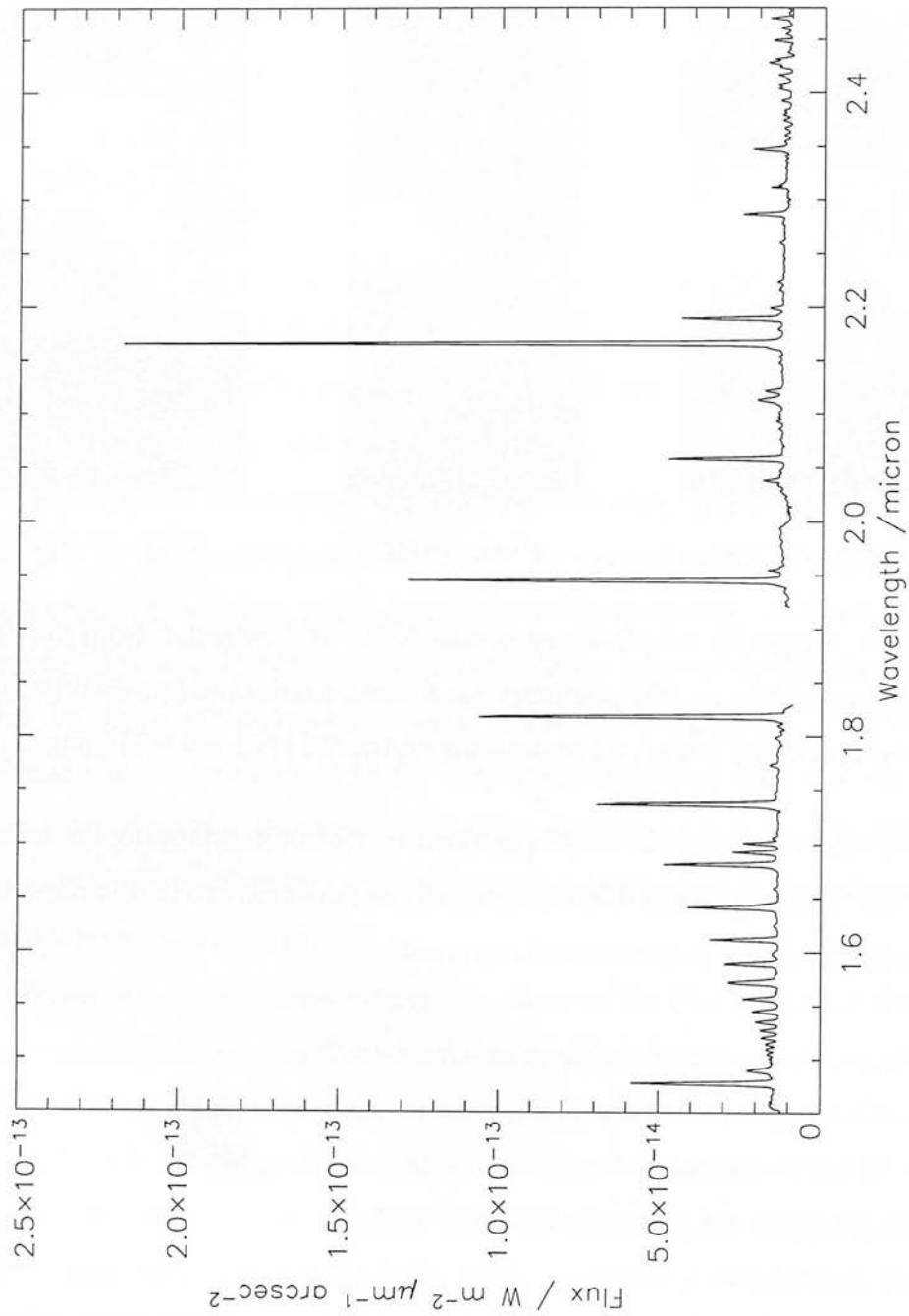

Figure 4.17: A spectrum on NGC 7027, extracted from the same datacube as the images in figure 4.16. This is the spectrum of a 1×1 arcsec region which encloses the brightest continuum emitting region visible in figure 4.16a.

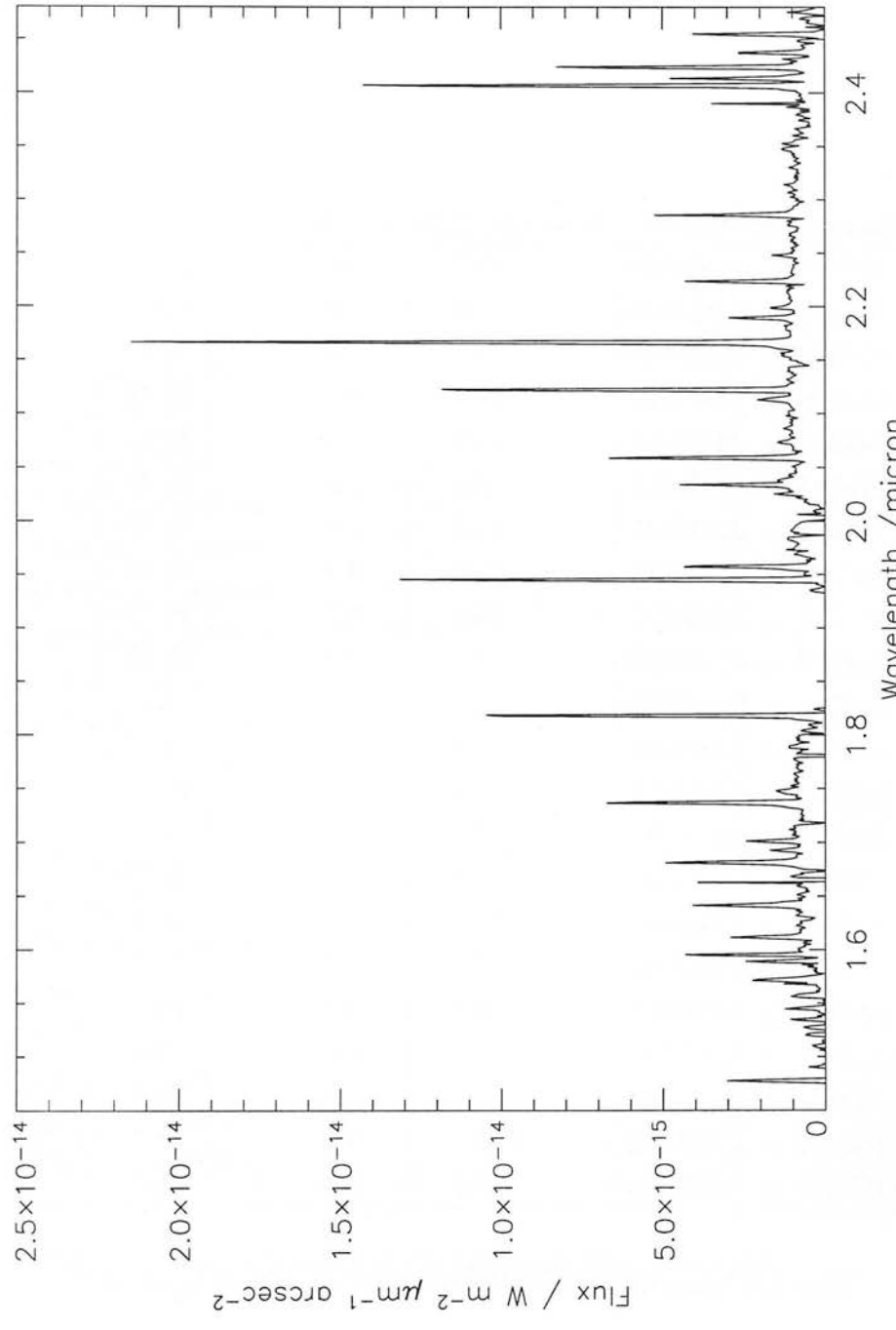

Figure 4.18: A spectrum of NGC 7027,extracted from the same datacube as the images in figure 4.16. This is the spectrum of a 1×1 arcsec region which encloses the brightest H_2 emitting region visible in figure 4.16c.

Wavelength /micron	Flux / 10^{-18} W m^{-2} arcsec^{-2}	Identification
1.477300 ± 0.000039	132.0 ± 4.0	He II
1.489482 ± 0.000120	21.8 ± 1.8	He II
1.520340 ± 0.000586	9.4 ± 7.4	Br 19–4
1.535098 ± 0.000220	19.1 ± 3.5	Br 18–4
1.544843 ± 0.000060	23.8 ± 1.1	Br 17–4
1.556515 ± 0.000022	31.6 ± 0.6	Br 16–4
1.571656 ± 0.000141	42.4 ± 3.9	Br 15–4
1.588805 ± 0.000026	50.5 ± 0.9	Br 14–4
1.611720 ± 0.000030	60.9 ± 1.5	Br 13–4
1.641578 ± 0.000060	75.0 ± 3.3	Br 12–4
1.659091 ± 0.000093	4.5 ± 0.4	HeII
1.681320 ± 0.000016	102.9 ± 1.2	Br 11-4
1.692539 ± 0.000174	36.8 ± 6.0	He II
1.700919 ± 0.000053	31.8 ± 1.8	He I
1.736805 ± 0.000043	162.6 ± 5.8	Br 10–4
1.818027 ± 0.000016	281.7 ± 3.5	Br 9–4
2.038045 ± 0.000092	14.3 ± 1.2	He II
2.058865 ± 0.000008	98.5 ± 0.7	He I
2.113476 ± 0.000105	16.7 ± 1.0	He I
2.122052 ± 0.000220	11.7 ± 2.6	H_2 1 − 0 S(1)
2.166279 ± 0.000012	510.1 ± 5.3	Br 7–4 (Br-γ)
2.189353 ± 0.000016	78.9 ± 1.1	He II

Table 4.2: Lines detected in the spectrum shown in figure 4.17.

Wavelength /micron	Flux / 10^{-18} W m^{-2} $arcsec^{-2}$	Identification
1.477337 ± 0.000064	11.5 ± 0.5	He II
1.571796 ± 0.000217	5.4 ± 0.7	Br 15–4
1.611834 ± 0.000049	6.6 ± 0.3	Br 13–4
1.641531 ± 0.000074	8.9 ± 0.5	Br 12–4
1.681318 ± 0.000138	12.2 ± 1.2	Br 11-4
1.701090 ± 0.000088	4.6 ± 0.4	He I
1.736850 ± 0.000039	17.4 ± 0.6	Br 10–4
1.818054 ± 0.000048	32.5 ± 1.5	Br 9–4
1.945122 ± 0.000014	35.5 ± 0.4	Br 8–4
1.957528 ± 0.000073	10.9 ± 0.7	H_2 1 – 0 S(3)
2.033867 ± 0.000047	8.6 ± 0.4	He II
2.058867 ± 0.000024	16.2 ± 0.4	He I
2.121972 ± 0.000021	30.8 ± 0.6	H_2 1 – 0 S(1)
2.166331 ± 0.000023	51.1 ± 1.1	Br 7–4 (Br-γ)
2.189407 ± 0.000038	4.8 ± 0.2	He II
2.223569 ± 0.000054	8.2 ± 0.4	H_2 1 – 0 S(0)
2.285762 ± 0.000071	10.2 ± 0.7	?
2.406705 ± 0.000065	33.4 ± 2.2	H_2 1 – 0 Q(1)
2.423869 ± 0.000025	18.5 ± 0.4	H_2 1 – 0 Q(3)
2.437592 ± 0.000096	5.3 ± 0.5	H_2 1 – 0 Q(4)
2.454828 ± 0.000067	9.1 ± 0.5	H_2 1 – 0 Q(5)

Table 4.3: Lines detected in the spectrum shown in figure 4.18.

Chapter 5

Shocked H_2 around G25.65+1.05

5.1 Introduction

5.1.1 Bipolar outflows in high-mass star formation

High-mass stars form in conjunction with low-mass stars in massive molecular clouds. Such clouds are much less common than regions in which only low-mass star formation takes place, and therefore the distances to the closest regions of high-mass star formation (a few kpc) are much greater than the distances to the nearest regions of low-mass star formation ($\sim$ 100 pc). This, combined with the high extinction at optical wavelengths due to the dusty molecular gas which makes up the clouds in which high-mass stars form, explains why high-mass star formation is significantly less well studied and understood than low-mass star formation.

Many regions of high-mass star formation are identified by the presence of ultracompact H II regions. These are small photoionised nebulae with diameters less than about 0.1 pc in diameter with electron densities greater than 10^4 cm^{-3}, excited by the intense ultraviolet radiation from the hot young star [Wood and Churchwell, 1989]. These regions emit bright radio continuum radiation, which is not absorbed by the surrounding cloud, making radio surveys an efficient way of searching for regions of high-mass star formation. Flux is also produced in the recombination lines of atomic hydrogen, but those lines at optical or ultraviolet wavelengths are likely to be entirely absorbed by extinction.

It has long been known that bipolar outflows play an important part in the for-

mation of low-mass stars. It has recently become clear that bipolar outflows are produced in the early stages of evolution of most, if not all, high-mass stars. Shepherd and Churchwell [1996b] observed 122 high-mass star forming regions selected from existing catalogues of ultracompact H II regions or from the *IRAS* point source catalogue using colour-colour selection criteria to identify ultracompact H II regions. Single dish observations of the ^{12}CO ($J = 1 - 0$) line were made using a 60 arcsec beam (half-power beam width). The full-width (FW) of this line was measured for each source to identify those containing high-velocity molecular gas. Only 10% were found to contain no high-velocity gas (FW < 15 km s^{-1}) and 41% had FW > 30 km s^{-1}. This, of course, said nothing about the morphology or source of the high velocity gas, but indicated that bipolar outflows might be found in a large proportion of high-mass star forming regions. Two of these sources (one of which was G25.65+1.05) were then mapped at low spatial resolution and were both found to be bipolar. The resolution of these maps was not sufficient to allow an estimate of the degree of collimation to be made or for the source of the outflow to be identified.

Since then further radio surveys of molecular line emission from high-mass star forming regions have confirmed that high-velocity molecular gas is associated with around 90% of these regions. It appears that in around 50% of the observed sources this gas takes the form of a bipolar outflow (Shepherd and Churchwell [1996a]; Zhang et al. [2001]; Ridge and Moore [2001]). Beuther et al. [2002b], mapping at a higher spatial resolution, found evidence of bipolar outflows in 21 of their 26 sources suggesting that bipolar outflows may be even more common than previously indicated, and may be associated with most young high-mass stars.

The mechanism by which a large mass of cold, neutral molecular gas can be accelerated to form an outflow is not known. The mass of the gas in the outflow may be tens of solar masses – comparable to, or even greater than, the mass of the protostar. Churchwell [2000] summarised four possible models:

1. *Accumulated stellar wind:* a high mass-flux, bipolar stellar wind perpendicular to the accretion disc accelerates material from the interstellar medium (ISM). It seems unlikely that this model can provide sufficient momentum or mass in the outflow to match the observed outflows.

2. *Entrained ISM in bipolar jets:* a highly collimated jet is produced by the protostar or inner disc or both. A mixing layer at the interface of the jet entrains ISM. Further ISM may be swept up by the leading shock (working surface) of the jet. There is evidence that this model describes reasonably well the outflows from low-mass stars in which a small fraction of a solar mass is entrained. It is not clear whether this mechanism allows the entrainment of the much larger masses seen in outflows from high-mass stars.

3. *Swept up ISM:* the working surface of an outflow lobe could sweep up a considerable mass of ISM if the opening angle of the flow is large (giving a large working surface), the working surface is reasonably continuous and the ISM in the region of the outflow is dense. From current observations it is not possible to quantify how effective wide angle outflows might be in sweeping up mass. The one example that we do have is the Orion IRC2 outflow, in which it appears that the flow does not sweep up dense ISM components, but sweeps round them, stretching them into filaments.

4. *Accretion driven:* infalling material is diverted into bipolar outflows due to high central pressures. This could be a mechanism by which angular momentum could be lost from the accreting material. This model does seem to be able to account for the large masses seen in outflows from high-mass stars. The outflow would be produced during a rapid accretion phase, which would also delay the formation of an ultracompact H II region [Churchwell, 1997]. Under this scenario the outflows which have been observed close to ultracompact H II regions are either relics of old outflows which are no longer driven or outflows from other young stars in the cluster at an earlier stage of evolution than the ionising star of the H II region.

The majority of the outflows observed so far appear to have much lower collimation factor – generally between 1 and 1.8 – than those seen from low-mass stars which often have a collimation factor of around 10 (see, for example, the interferometric observations of Richer et al. [2000]). This would be hard to explain if the outflows are formed by the same jet entrainment model as that believed to describe the outflows

from low-mass stars. However, Beuther et al. [2002b] argued that the observed degree of collimation could be significantly reduced by the low spatial resolution of the maps and that the low resolution maps would be consistent with high-mass flows which were just as well collimated as low-mass flows. Interferometric observations have shown collimation factors as high as 10 [Beuther et al., 2002a] in flows from high-mass stars and have revealed that some of these apparently uncollimated or poorly collimated flows can be resolved into several well collimated flows from separate young stars. Detection of multiple flows in a region in which high-mass stars are forming would not be surprising. High-mass stars are known to form in dense clusters [Garay and Lizano, 1999], so high spatial resolution observations are essential for identifying the source of an individual outflow. The presence of a collimated outflow would imply the presence of a stable accretion disc and hence strengthen the view that high mass stars are formed by steady accretion, in a similar way to low mass stars, rather than by merging of intermediate-mass protostars in the centre of dense clusters as has been suggested by Bonnell [1999].

5.1.2 G25.65+1.05

The ultra-compact H II region G25.65+1.05 (IRAS 18316−0602) has a radial velocity of 41.5 km s^{-1} [Shepherd and Churchwell, 1996b] which, using the galactic rotation curve of Brand and Blitz [1993], gives a distance of either 3.0 or 12.3 kpc. McCutcheon et al. [1991] argued that the far distance would imply an unreasonably high luminosity, and we therefore adopt the near distance. The H II region is thought to be excited by a young B1V star [Zavagno et al., 2002]. As described above, a highly energetic bipolar outflow was found to be centred on or close to the H II region by Shepherd and Churchwell [1996b]. A large *K*-band excess was detected from the central source of the H II region by Zavagno et al. [2002]. They argue that this, combined with the methanol masers detected by Walsh et al. [1998] – which lie in a line to the south of the H II region with velocities consistent with Keplerian orbits – and the absorption features of various ices detected by d'Hendecourt et al. [1996], suggest the presence of a disc.

We decided to observe G25.65+1.05 in the near-infrared in order to examine the

possibility of obtaining high spatial resolution information about the morphology of outflows in high-mass star forming regions. If it is possible to separate multiple outflows and determine the degree of collimation using near-infrared observations then this may be an attractive alternative to the radio interferometry observations discussed above. Most of the near-infrared flux detected from molecular outflows is emission from molecular hydrogen excited by shocks in the outflow or fluorescently excited by ultraviolet photons from the hot young star.

5.1.3 Shocks

Why do shocks exist?

We consider a radiationless, reversible flow in a fluid with no magnetic fields present, following the description given by Dopita and Sutherland [2003]. All flows must conserve mass and momentum. In vectorial form the *continuity equation*, describing the conservation of mass, can be written

$$\frac{\partial \rho}{\partial t} + \nabla.(\rho \mathbf{v}) = 0. \tag{5.1}$$

In a one dimensional flow this simplifies to

$$\frac{d\rho}{dt} + \frac{d}{dx}(\rho v) = 0. \tag{5.2}$$

The conservation of momentum is expressed in *Euler's force equation*, which states that the rate of change of momentum within a test volume is equal to the flux of momentum into the test volume plus the external forces (such as gravitational forces) and internal forces due to pressure gradients acting on the volume:

$$\rho\left[\frac{\partial \mathbf{v}}{\partial t} + (\mathbf{v}.\nabla)\mathbf{v}\right] = \mathbf{F} - \nabla P. \tag{5.3}$$

Again this can be simplified if the flow is one dimensional and no external forces are applied:

$$\rho\frac{dv}{dt} + \rho v\frac{dv}{dx} = -\frac{dP}{dx}. \tag{5.4}$$

If we consider a small disturbance propagating in a fluid, which is initially at rest, in which the change in velocity is small and the changes in ρ and P are small compared with their initial values ρ_0 and P_0 then we can neglect the second term in equation 5.4

as the product of two small quantities. Similarly the second term in the expansion of $d(\rho v)/dx$ in equation 5.2 can be neglected. Combining these gives

$$\frac{dv}{dx} = -\frac{1}{\rho_0}\frac{d\rho}{dt}. \tag{5.5}$$

The pressure change can be expressed in terms of the density change using the adiabatic equation of state $P = K\rho^\gamma$, where K is a constant and $\gamma = C_P/C_V$ is the ratio of specific heats at constant pressure and at constant volume:

$$dP = \left(\frac{\gamma P_0}{\rho_0}\right) d\rho, \tag{5.6}$$

which, when substituted into equation 5.4 and neglecting the small second term, gives

$$\frac{dv}{dt} = -\frac{1}{\rho_0}\left(\frac{\gamma P_0}{\rho_0}\right)\frac{d\rho}{dx}. \tag{5.7}$$

Differentiating equation 5.5 with respect to t and equation 5.7 with respect to x and subtracting one from the other gives

$$\frac{d^2\rho}{dt^2} + \left(\frac{\gamma P_0}{\rho_0}\right)\frac{d^2\rho}{dx^2} = 0. \tag{5.8}$$

This is a wave equation, and from this we see that the sound speed (the speed at which changes in density are propagated) is given by

$$c_s = \left(\frac{\gamma P}{\rho}\right)^{1/2}. \tag{5.9}$$

If the change being propagated is an adiabatic increase in density from ρ_1 to ρ_2, obeying $P = K\rho^\gamma$, then this implies that, following the compression, the sound speed in the medium is increased in the ratio $(\rho_2/\rho_1)^{(\gamma-1)/2}$ ($\gamma = 5/3$ in a monatomic gas or $7/5$ in a diatomic gas, such as H_2). As a result of this, further increases in density propagate faster and catch up with the initial propagating density increase. Successive increases in density pile up, creating a discontinuity in the flow variables (a shock).

J-shocks

In many astrophysical outflows the plasma is highly ionised, strongly coupling the ions and electrons, giving a very short mean free path of charged species. In such a shock, known as a jump-shock, or J-shock, the gas may be treated as a single fluid.

The thickness of the shock front (the region in which bulk flow is transformed into the random thermal motion of the particles) is short compared to the cooling length. The shock front itself is then non-radiative and the above model of an infinitely thin discontinuity in the flow variables is a good approximation.

Hollenbach [1997] described the structure and properties of a J-shock with $v_s = 80$ km s^{-1} incident upon ambient gas of density $n_a = 10^5$ cm^{-3}. The gas is first heated to $T > 10^5$ K, causing dissociation and ionisation and the emission of a considerable flux of ultraviolet photons. The gas behind the shock front cools to 10^4 K, at which temperature the Lyman photons from the shock-front maintain a temperature plateau by photoionisation heating of H. Once the UV photons have been absorbed the gas cools by atomic fine structure lines, especially the [O I] 63 μm line. Molecular hydrogen does not reform at a significant rate behind the shock front until the temperature falls below around 500 K, so the collisional excitation of the 2 μm H_2 vibrational lines is insignificant and only weak emission from newly-formed H_2 is expected. The heating effect of H_2 reformation when $n_a > 10^4 - 10^5$ cm^{-3} produces another temperature plateau at around 400 K in which the gas becomes increasingly molecular. H_2O is formed, and if $n_a > 10^6$ cm^{-3} then the conditions are ideal for H_2O maser production.

C-shocks

Continuous shocks, or C-shocks, are seen in slow (less than about 50 km s^{-1}) shocks in weakly ionised molecular gas in the presence of magnetic fields. The energy transfer between ionised and neutral species takes place over a timescale longer than the characteristic cooling time of the plasma. In such a shock the flow variables change continuously – the approximations to a discontinuous shock made above are no longer valid. The magnetic field is pinned to the ionised component of the gas and is compressed along with the ions. In general the Alfvén velocity in the ionised component of the gas is significantly higher than the sound speed (the speed at which the shock front moves). Information about the approaching shock is, therefore, communicated ahead of the shock front itself by a magnetic precursor which accelerates the ions, leading to a continuous variation of the flow variables [Dopita and Sutherland, 2003]. This produces relative motion between the neutral components of the gas and the ions

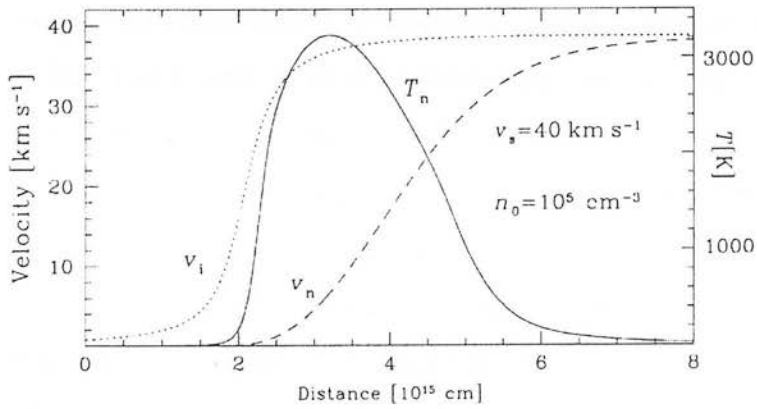

Figure 5.1: The structure of a C-shock, showing the temperature of the neutral component of the fluid (T_n) and the velocities of the ionised and neutral components (v_i and v_n) [Kaufman and Neufeld, 1996]

and magnetic field. The neutral components are accelerated and heated by collisions with the ions. If the radiation from the shock front is sufficient to suppress the temperature increase then this can produce a continuous variation in the flow variables of both the ionised and neutral components of the fluid. As can be seen from figure 5.1, which shows the velocities of the ionised and neutral components of the fluid in the frame of the preshock gas, the ions are accelerated first and then drag the neutral components to the shock velocity.

Almost all emission from a C-shock is produced as near-infrared emission from the gas being heated in the shock front, whereas the emission from a J-shock is given off largely in the mid-infrared after the initial heating by the shock front [Hollenbach, 1997]. C-shocks are generally non-dissociative because molecular cooling is necessary to maintain the C-shock, and the peak temperature therefore rarely exceeds 3000–5000 K. A large flux of 2 μm H_2 emission is produced and all oxygen not in CO is rapidly formed into H_2O, again providing the conditions for H_2O masers to form.

5.1.4 Near-infrared molecular hydrogen emission

The excitation and near-infrared emission lines of molecular hydrogen were reviewed by Sternberg [1988]. The ground electronic state of H_2 supports 15 bound vibrational levels, labelled by the quantum number ν. A series of rotational levels, labelled with

the quantum number j, is associated with each vibrational level. Near-infrared emission lines from H_2 are due to transitions between the different vibrational and rotational levels within the ground electronic state. The first excited vibrational level lies 6000 K above the ground state, and the separation between adjacent levels decreases with increasing v due to the the anharmonicity of the potential energy curve. Only electric quadrupole transitions are allowed between rovibrational levels in a homonuclear molecule, such as H_2. The selection rules for quadrupole transitions allow changes in j of 2, 0 or -2 (but 0–0 transitions are not allowed). There are no restrictions on the change in v, though transitions with smaller changes in v are more likely. A rovibrational transition is identified by the upper and lower vibrational quantum numbers, the letter S, Q or O depending on whether the rotational quantum number in the lower level of the transition is smaller than, equal to, or greater than that of the upper level, and the value of j in the lower level of the transition. For example, the 2.122 μm $1-0\,S(1)$ transition goes from an upper state with $v = 1$ and $j = 3$ to a lower state with $v = 0$ and $j = 1$. Large fluxes of H_2 emission can be produced in photodissociation regions around young stars emitting intense UV radiation or in shocks.

Emission from photodissociation regions

In low density photodissociation regions ($n < 10^4\ cm^{-3}$) the gas remains cold (around 100 K) due to efficient cooling by fine structure transitions of O I and C II. The ultraviolet photons produce electronically excited H_2 molecules, which rapidly decay to excited vibrational states in the electronic ground state. This UV pumping produces a cascade of radiative decays. This is a non-thermal process and the line ratios in the resulting spectrum correspond to excitation temperatures far higher than the kinetic temperature of the gas.

When dense photodissociation regions are exposed to intense UV fields the gas is heated by the collisional de-excitation of UV pumped H_2 molecules, with temperatures exceeding 1000 K. Collisional process dominate the lower excitation levels, producing a distribution which tends towards that expected from gas in local thermal equilibrium.

Emission from shocks

Molecular hydrogen is dissociated in J-shocks. Molecules reform in the post-shock gas once the temperature falls to around 500 K, as described above. At this temperature little H_2 emission would be produced. Some emission may be observable from molecules which reform in an excited state. The line ratios expected from such emission would be similar to that produced by UV pumping. C-shocks are non-dissociative and produce gas with peak temperatures of 1000–5000 K. This leads to H_2 emission with line ratios corresponding to local thermal equilibrium at the temperature of the gas.

Diagnostics

As we have seen, near-infrared emission from molecular hydrogen can be produced either by thermal excitation in shock-fronts or fluorescent excitation by ultraviolet photons from hot young stars. These cases can often be distinguished using the ratio of the intensity of the $1-0$ S(1) line to that of the $2-1$ S(1) H_2 line. In thermally excited gas this ratio is ~ 12 at 2000 K, falling as the temperature is increased, whereas in fluorescently excited gas the ratio is ~ 2 if the density is below $\sim 10^4$ cm^{-3} [Sternberg and Dalgarno, 1989]. This line ratio is a useful diagnostic because the lines are close in wavelength, so measuring the ratio accurately is straightforward, and they originate from excitation states with very different upper energy levels. At higher densities in the presence of high intensity ultraviolet radiation the spectrum tends towards that seen from purely thermally excited gas making it more difficult to distinguish fluorescent and shock excited gas. However, when molecular hydrogen is excited by non-ionizing ultraviolet photons ($91.2 < \lambda < 110.8$ nm) there will also be dissociation of molecules by ionizing photons ($\lambda < 91.2$ nm), resulting in emission in the 2.166 μm Brackett-γ recombination line.

The properties of four classes of shocks were summarised by Davies et al. [2000]:

1. *fast J shock* (100–300 km s^{-1}): hydrogen molecules are dissociated and reform producing a spectrum similar to that of UV fluorescence. The flux of Brackett-γ and H-band Fe II lines are comparable to the $1-0$ S(1) flux.

2. *slow J shock*: strong H_2 lines are produced and molecules are not dissociated. However, in normal ionization fractions, magnetic field strengths and gas densities, such shocks are expected to evolve into C-type shocks.

3. *fast C shock*: shock velocities of $\sim$ 40 km s^{-1} heat the gas to $\sim$ 2000 K or more (dependent on the velocity) producing strong H_2 lines.

4. *slow C shock*: peak temperature 300 K or less, resulting in very weak H_2 emission.

5.2 Observations

5.2.1 Imaging

Imaging observations of G25.65+1.05 were made on 29 June 2002 using UFTI at the UK Infrared Telescope (UKIRT). UFTI is a 1 to 2.5 μm camera using a 1024 $\times$ 1024 HgCdTe array with a plate scale of 0.091 arcsec/pixel. A single 9-point jitter in a 3 $\times$ 3 pattern with offsets of 10 arcsec was observed with 60 sec exposures using the *K*98 broad-band filter, giving 9 min on source. The same 9-point jitter pattern was repeated three times using exposures of 100 s with the 2.122 μm 1 $-$ 0 S(1) H_2 narrow-band filter giving a total of 45 min on source. The individual frames from each filter were flat-fielded and mosaiced together automatically by the ORAC-DR pipeline.

Sources emitting in the 1 $-$ 0 S(1) H_2 line will be detected in both the broad-band and narrow-band images but will appear brighter relative to the continuum sources in the narrow-band images. The two mosaics are shown in figure 5.2. The narrow-band image with 0.6 arcsec seeing was smoothed to match the 0.7 arcsec seeing of the broad -band image. The broad-band image was scaled in intensity and subtracted from the narrow-band image to leave 1 $-$ 0 S(1) H_2 emission as shown in figure 5.3. The H II region itself and some stars around it appear negative in this subtracted image due to extinction, which reddens the image, making it appear brighter in the scaled broad-band image than in the narrow-band image because the central wavelength of the broad-band filter transmission is longer than that of the narrow-band filter. A number of point sources are visible in addition to the extended emission. These are ghost images of bright stars produced by the narrow-band filter and residuals left where

stars have been imperfectly subtracted. The complete mosaic covers a 1.8×1.8 arcmin field centred on the H II region. No H_2 emission was detected outside the region shown here.

The brightest H_2 emission was detected to the south-east of the H II region, taking the form of a region of faint, diffuse emission containing a number of bright, compact sources (A–D). To the north-west of the H II region there is a straight, narrow line of faint emission with a bright source (E) at one end. There is also faint, diffuse emission to the south and north-east of the H II region.

5.2.2 Long-slit spectroscopy

Long slit spectra were obtained on 30 June 2002 using CGS4 at UKIRT. The 40 l/mm grating was used, giving a wavelength coverage of 1.9 to 2.5 μm. A one pixel (0.6 arcsec) wide slit was used and the detector was stepped over 2 pixels in half-pixel increments to give a fully sampled spectrum with a spectral resolution of 600. Observations were made through thick, patchy cirrus causing large variations in the detected flux. Individual exposures were weighted by the square of the signal to noise ratio of the $1-0$ S(1) line before they were added together to maximise the signal to noise ratio of the combined data.

Sources C and D were observed with a single slit position. The resulting spectra are shown in figure 5.4. The high $1-0$ S(1) to $2-1$ S(1) ratio (6.8 ± 0.9 for source C and 8.7 ± 3.2 in source D) and the absence of Brackett-γ emission in these sources confirms that these are shock excited rather than fluorescently excited by UV flux from a nearby hot star.

5.2.3 Integral field spectroscopy

Sources A and B were observed on 24 October 2002 as part of the UIST commissioning observations. The HK grism was used, giving a spectral coverage of 1.4–2.5 μm with a spectral resolution of 800–1000. The target was acquired using UIST in K-band imaging mode. The IFU field of view was rotated to a position angle of 90°, making the long axis of the field run E-W. At this stage of commissioning the location of the IFU field of view on the imaging field was not accurately known and after observing two

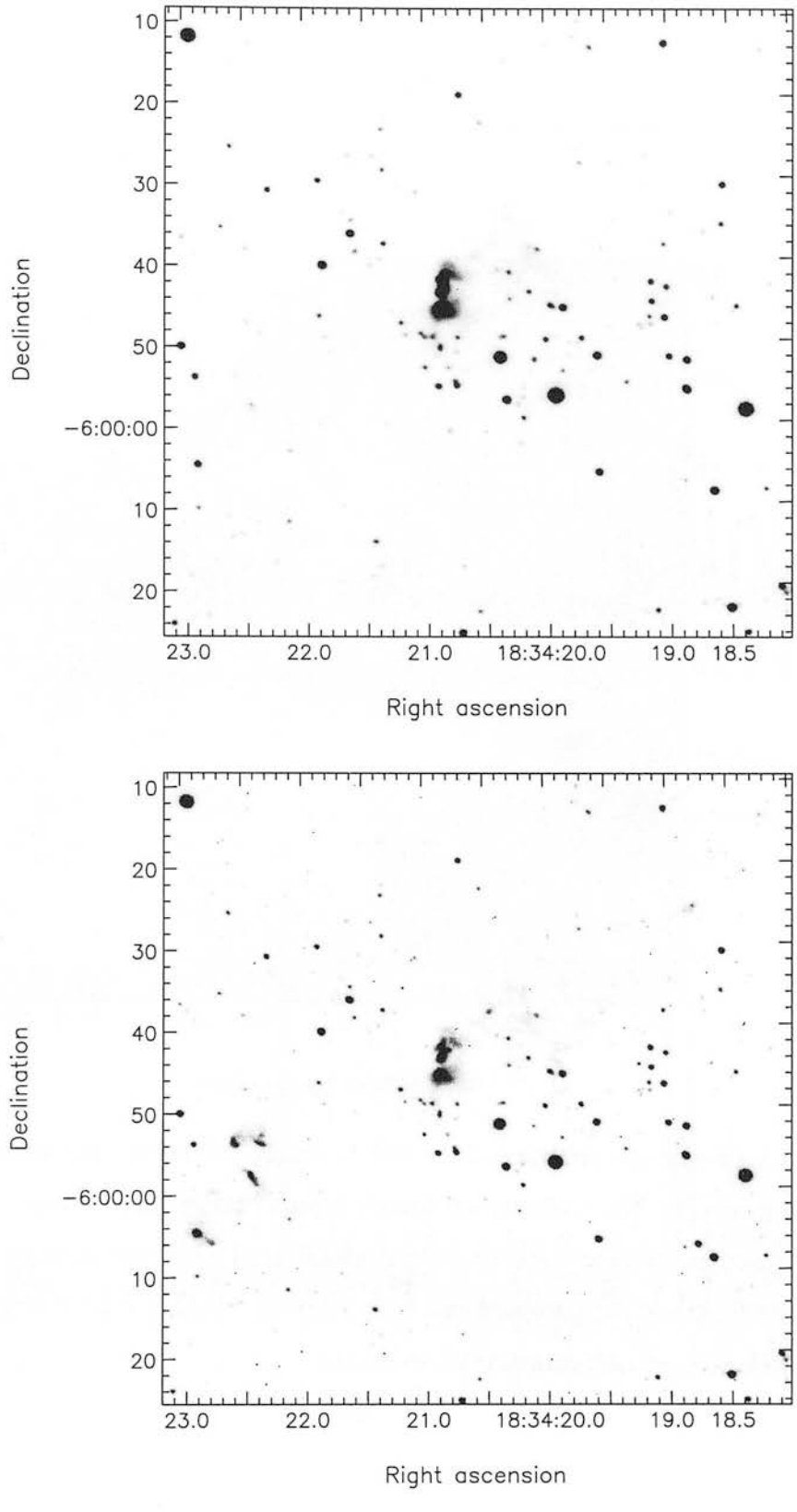

Figure 5.2: Part of the UFTI mosaic images (a) K98 broad-band filter; (b) $1-0$ S(1) narrow-band filter. All coordinates are J2000.

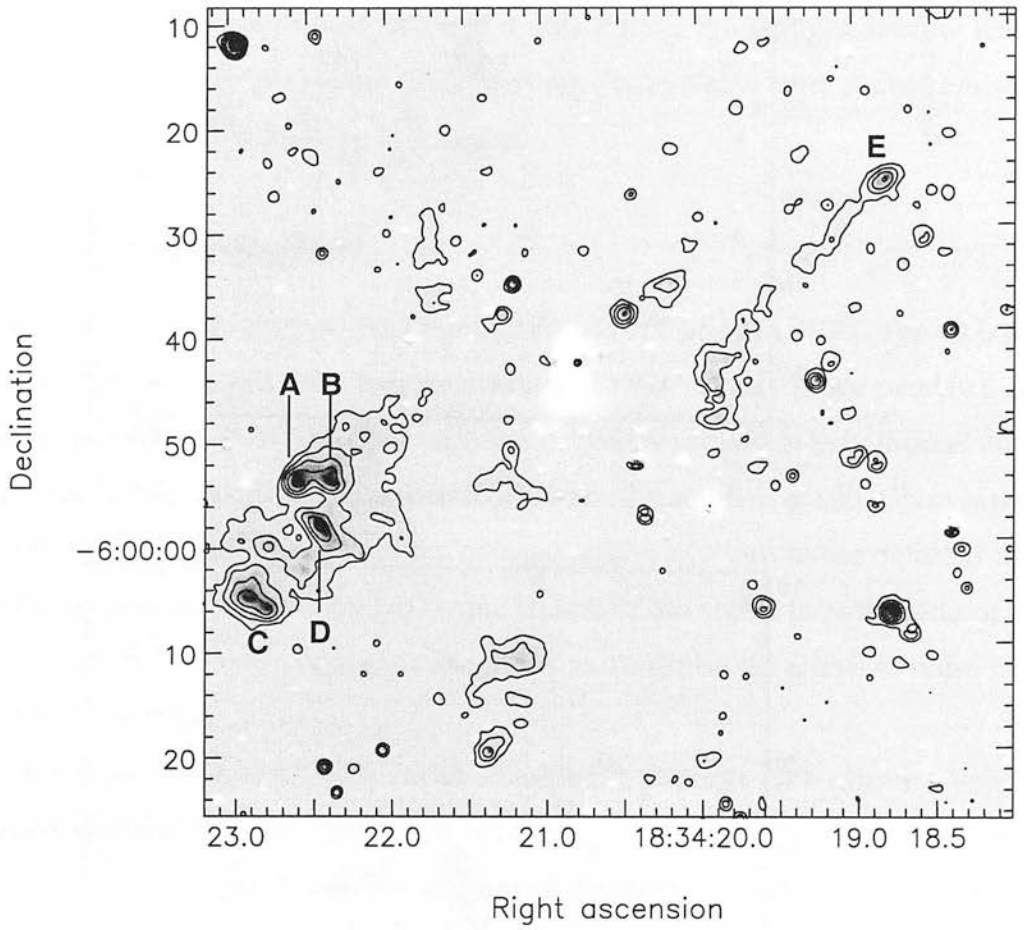

Figure 5.3: A continuum subtracted $1-0$ S(1) image created by subtracting figure 5.2a from figure 5.2b. The contours are drawn from a version of the image smoothed with a 0.5 arcsec gaussian and are logarithmically spaced with each contour a factor of two higher in flux than the previous one from a lowest contour at 3σ above the noise in the smoothed image. All coordinates are J2000.

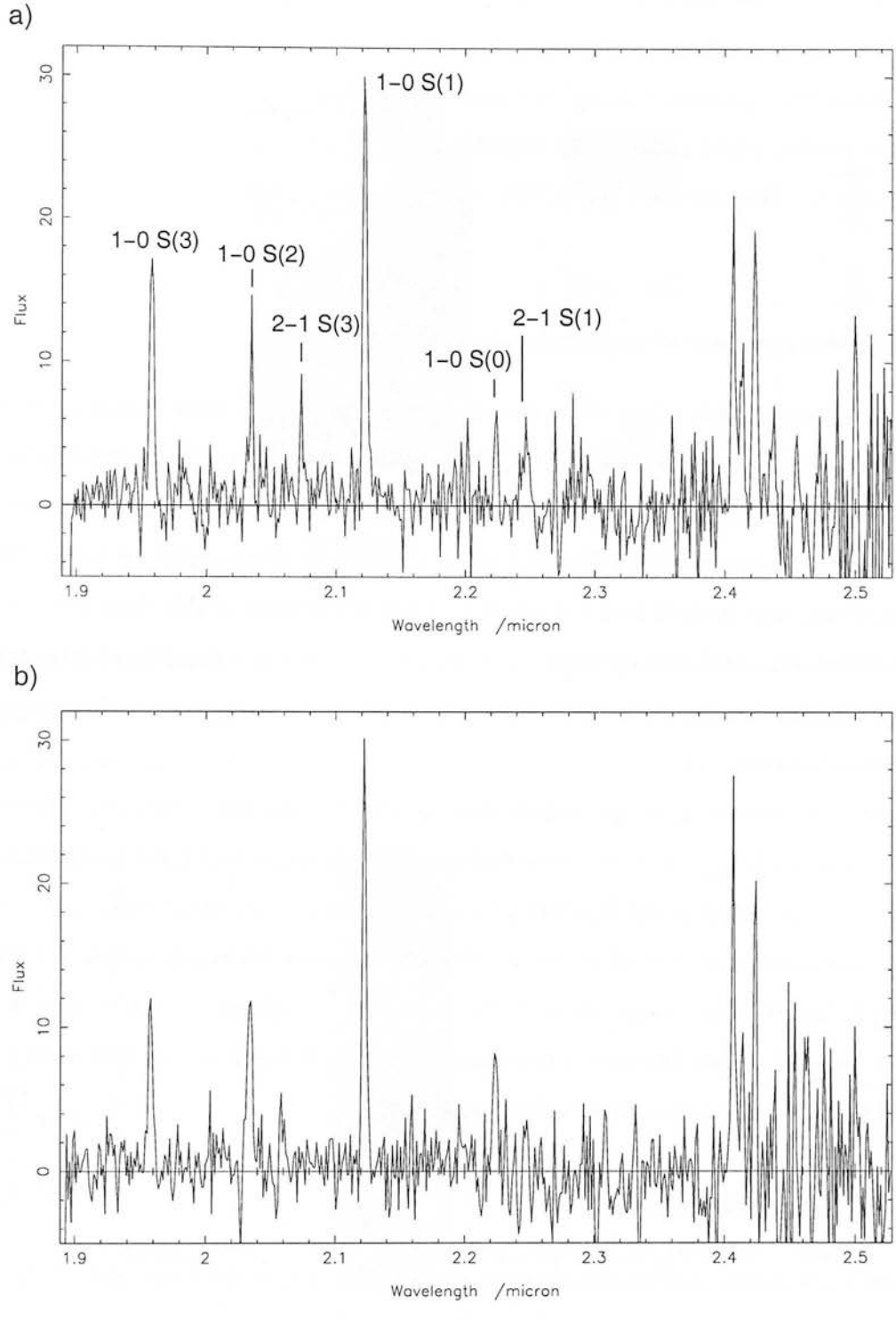

Figure 5.4: The spectra of (a) source C and (b) source D obtained using CGS4. No attempt was made at flux calibration due to the highly variable atmospheric conditions.

object-sky-sky-object 'quads' of frames the source was found not to be entirely within the IFU field. The position of the telescope was adjusted 1 arcsec east and then 1 arcsec south after a further set of observations. Two blocks of four frames were observed in each of these three positions using an exposure time of 120s, giving a maximum of 24 min on source (some parts of the object were only observed in one or two of the three positions). The standard star BS7260 was then observed with one block of four frames.

Combining the data into a single datacube

The observations at each of the three positions described above were formed into an (x, y, λ) data-cube using the ORAC-DR pipeline described in chapter 3. Each frame was divided by a flat-field frame. Pairs of frames were subtracted to give a sky-subtracted frame which was wavelength calibrated using a spectrum of an argon arc lamp. The resulting frame was formed into a datacube. All of the spectra in this datacube were divided by the standard-star spectrum to remove variations in atmospheric transmission with wavelength and flux calibrated using a black-body spectrum at the temperature of the standard-star.

The known 1 arcsec telescope offsets were used to register the three data-cubes in the two spatial dimensions. These were mosaiced into a single data-cube using **makemos**, which is included in the Starlink CCDPACK package. An image extracted from this datacube at the wavelength of the $1-0$ S(1) molecular hydrogen line (2.122 μm) is shown in figure 5.5a. A spectrum of the sum of the brightest part of source A is shown in figure 5.6. No Brackett-γ emission from atomic hydrogen or 1.64 μm Fe II emission was detected anywhere in the source.

Measuring the line intensities

A spectrum was formed by summing over all spatial pixels of the data-cube. A Gaussian profile was fitted to the bright $1-0$ S(1) line in this spectrum and was found to be centred at (2.12209 ± 0.00003) μm with FWHM $(2.28 \pm 0.05) \times 10^{-3}$ μm. The other lines are all much weaker, so to obtain the best possible measurement of the flux in each line a Gaussian profile was scaled to fit the line keeping the FWHM of the

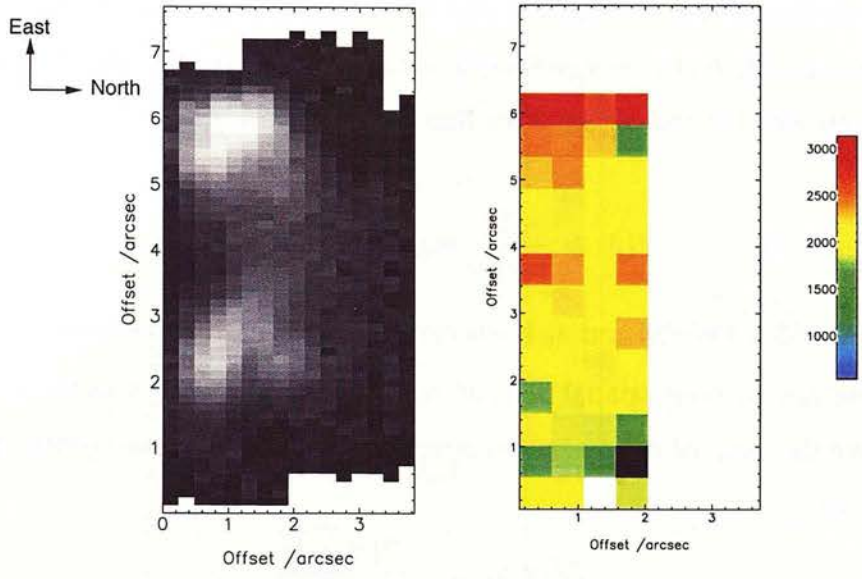

Figure 5.5: *left:* The $1-0$ S(1) line extracted from the mosaiced datacube. At a distance of 3 kpc 1 arcsec corresponds to 0.015 pc. *right:* The temperature map derived from the IFU data. Temperature in K.

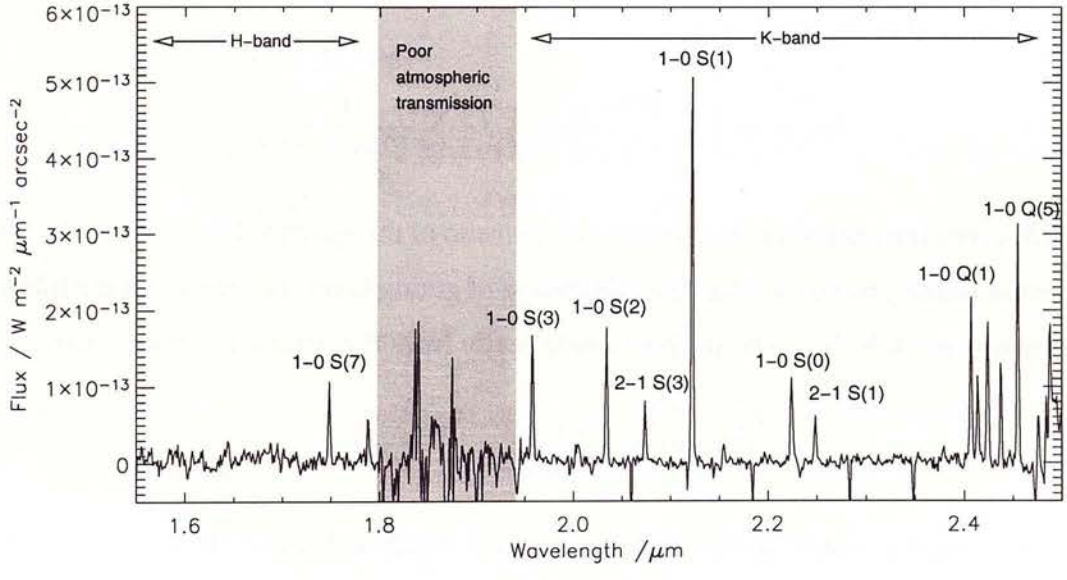

Figure 5.6: The spectrum obtained by summing over the brightest region of source A. Fluxes measured from this spectrum are given in figure 5.1.

line fixed at 0.00228 μm and the offset of the line from the $1-0$ S(1) line fixed by the known wavelength of the line.

This was done using the method described by Horne [1986]. A spectrum, $\Psi(\lambda)$, was generated with the same wavelength scale as the data containing a Gaussian peak with the same FWHM and centre as the line to be fitted and normalised to enclose unit area:

$$\Psi(\lambda) = \frac{1}{\sigma\sqrt{2\pi}} \exp\left(\frac{-(\lambda-\lambda_0)^2}{2\sigma^2}\right)$$

where $\sigma = 2.355 \times$ FWHM and λ_0 is the central wavelength of the spectral line.

The spectrum at every spatial pixel of the datacube, $D(x, y, \lambda)$ was then divided by $\Psi(\lambda)$ to give the ratio of the measured spectra line to the Gaussian profile generated with a flux of 1:

$$D'(x, y, \lambda) = \frac{D(x, y, \lambda)}{\Psi(\lambda)}$$

and the variance array associated with $D'(x, y, \lambda)$ was generated from the original variance array, $V(x, y, \lambda)$:

$$V'(x, y, \lambda) = \frac{V(x, y, \lambda)}{(\Psi(\lambda))^2}$$

An image, $I(x, y)$ was produced by taking a weighted mean of $D'(x, y, \lambda)$ over the λ dimension, weighting by $V'(x, y, \lambda)$:

$$I(x, y) = \left(\sum_\lambda \frac{D'(x, y, \lambda)}{V'(x, y, \lambda)}\right) \Big/ \left(\sum_\lambda \frac{1}{V'(x, y, \lambda)}\right)$$

This gives the optimal measurement of the ratio of the spectral line intensity to the model Gaussian profile, and has the advantage of giving Gaussian errors on the intensities measured which can be derived analytically from the original variance array:

$$\sigma^2(x, y) = 1 \Big/ \left(\sum_\lambda \frac{1}{V'(x, y, \lambda)}\right),$$

whereas a more general Gaussian fitting method which is designed to allow fits with more free parameters, such as that offered by the FIGARO **fitgauss** routine, must estimate the variance from the curvature in the χ^2 value as the fit converges [Shortridge et al., 2002].

Transition	λ_j /μm	E_j /K	A_j /10^{-7} s	g_j	Flux /W m^{-2} arcsec^{-2}
1 – 0 S(7)	1.7480	12817	2.98	57	$(2.4 \pm 0.2) \times 10^{-16}$
1 – 0 S(3) †	1.9576	8365	4.21	33	
1 – 0 S(2)	2.0338	7584	3.98	9	$(4.4 \pm 0.2) \times 10^{-16}$
2 – 1 S(3)	2.0735	13890	5.77	33	$(1.7 \pm 0.2) \times 10^{-16}$
1 – 0 S(1)	2.1218	6956	3.47	21	$(11.4 \pm 0.2) \times 10^{-16}$
1 – 0 S(0)	2.2235	6471	2.53	5	$(2.7 \pm 0.2) \times 10^{-16}$
2 – 1 S(1)	2.2477	12550	4.98	21	$(1.7 \pm 0.2) \times 10^{-16}$
1 – 0 Q(1) †	2.4066	6149	4.29	9	
1 – 0 Q(2) †	2.4134	6471	3.03	5	
1 – 0 Q(3) †	2.4237	6956	2.78	21	
1 – 0 Q(4)	2.4375	7586	2.65	9	$(3.0 \pm 0.3) \times 10^{-16}$
1 – 0 Q(5) †	2.4548	8365	2.55	33	

Table 5.1: The wavelengths, upper energy levels, Einstein A coefficients and degeneracies of the H_2 lines detected in our spectra. Lines marked † were found to be absorbed by unresolved atmospheric absorption features and were discarded. The fluxes given are measured from the spectrum in figure 5.6 and are not corrected for extinction.

Calculating the column density

The measured intensity, I, of a given H_2 line can be used to calculate the column density of the upper excitation level of the transition:

$$N_j = \frac{4\pi\lambda_j I}{A_j hc} \tag{5.10}$$

where A_j is the Einstein-A coefficient of the transition. The relative column densities of any two excitation levels can be expressed in terms of an excitation temperature T_{ex}:

$$\frac{N_i}{N_j} = \frac{g_i}{g_j} \exp\left(\frac{-(E_i - E_j)}{kT_{ex}}\right) \tag{5.11}$$

where g_j is the degeneracy and E_j is the energy of the level. The values of λ_j, E_j, A_j and g_j for the lines detected in our spectra are shown in table 5.1.

Extinction to the source

Before we could use our measured intensities to derive the excitation temperature of the gas it was necessary to measure and compensate for extinction. In the absence of more information it was assumed that the extinction was constant across the IFU field of view. An extinction law of the form $\tau(\lambda) = A_k\,(\lambda/2.2\,\mu\mathrm{m})^{-1.75}$ was used, giving a corrected intensity of $I_{\mathrm{corr}} = I/e^{-\tau(\lambda)}$. Plotting $\log(N_j/g_j)$ against E_j should give a straight line if we assume that in each pixel we are detecting gas at a single temperature. If the value of A_k used to correct the line intensities from which the column density is calculated is wrong then the scatter of the points will increase. Our measurements are particularly sensitive to this because we have measured one *H*-band line ($1-0$ S(7) at 1.748 μm) which comes from an upper level close in energy to the upper level of two *K*-band lines ($2-1$ S(1) at 2.248 μm and $2-1$ S(3) at 2.074 μm).

The value of A_k which minimised the scatter of the points was measured for each spatial pixel in the two brightest columns in the rebinned data-cube. It was found that the intensities of the $1-0$ S(3) line and all the Q-branch lines other than the $1-0$ Q(4) line were not consistent with any non-negative values of A_k. These lines were therefore assumed to be partly absorbed by the very narrow atmospheric lines which dominate the edges of the *K*-band window which, being spectrally unresolved, are not removed by dividing by the standard star. Once these lines were excluded the mean value of A_k over all the spatial pixels used was found to be $A_k = 0.7 \pm 0.1$, where the error on the derived value was estimated from the scatter of the value measured from one spatial pixel to another. The variation in the measurements appeared random, with no evidence for any systematic variation in extinction across the source. There was also no evidence of curvature in the N_j/g_j versus E_j plots, which are shown in figure 5.8, though the absence of any points with upper energy levels between 8000 and 12000 K would make it hard to detect small deviations from a straight line. A curved line in this plot would indicate deviation from local thermal equilibrium within a single spatial pixel, showing that measurement of a single excitation temperature would not be appropriate.

A alternative method to estimate the extinction is to look at the ratio of the $1-0$ Q(4) to the $1-0$ S(2) line. These two lines share the same upper energy level, so the

ratio is constant at 1:1.83 regardless of temperature, density or excitation conditions. From the measured ratio we can derive the extinction. Integrating the intensity of these two lines over the whole field of the IFU we find that $A_k = 0.75 \pm 0.25$. While the error bars are large on this measurement it is clearly consistent with the value derived above.

Variation in temperature

The line fluxes were measured at each spatial pixel in the rebinned data-cube and corrected for extinction using the extinction law described in section 5.2.3. The value of N_j/g_j was then derived from each corrected line flux using equation 5.10. The excitation temperature was measured by fitting equation 5.11 to all of the measurements made at a single spatial pixel using a maximum likelihood method. The fit is made to the values of N_j/g_j rather than fitting a straight line to $\log(N_j/g_j)$ because the errors on N_j/g_j are normally distributed, whereas the errors on $\log(N_j/g_j)$ are not even symmetrical. Using the maximum likelihood method is useful because we are carrying out a two parameter fit but we are only interested in the value of one parameter (T). Marginalising the two dimensional likelihood gives us a measurement of the likelihood distribution of T taking the uncertainty on the value of the constant of proportionality into account.

When equation 5.11 is fitted to a single line intensity there is a degeneracy between T and the constant of proportionality, causing the most likely value of the constant of proportionality to vary exponentially with T. For this reason equation 5.11 was reformulated as

$$\frac{N_j}{g_j} = \exp\left(\frac{-E_j}{kT} + \alpha\right) \tag{5.12}$$

where α is the logarithm of the constant of proportionality.

The likelihood of a range of values of T and α was calculated for each measured line flux assuming a Gaussian error distribution on the measurements of the line intensity and using a uniform prior probability density function for both parameters:

$$L_j(T, \alpha) \propto \frac{\exp[-(\delta/2\sigma)^2]}{\sigma\sqrt{2\pi}}. \tag{5.13}$$

In equation (5.13) δ is the difference between the value of N_j/g_j derived from the measured intensity using equation (5.10) and that calculated using equation (5.12) and

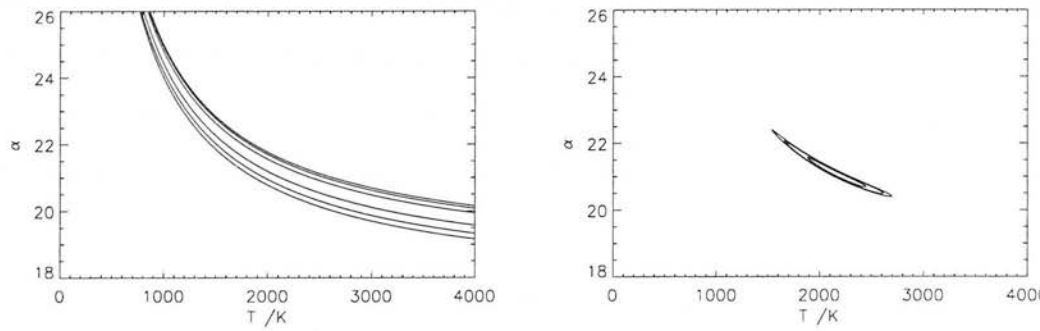

Figure 5.7: (a) The likelihood of the parameters T and α were evaluated for a single spatial pixel using the intensity of a single spectral line. (b) When other spectral lines are introduced the degeneracy is partly broken. On both plots the contours are at the 68%, 95% and 99% confidence levels, equivalent to 1σ, 2σ and 3σ error bars on a gaussian distribution.

σ is the 1σ error on the measured value of N_j/g_j. When this is evaluated for a single spectral line there is a degeneracy between the two parameters, as shown in figure 5.7a. The likelihood of the parameters using all the line fluxes is calculated by taking the product of all the individual likelihoods:

$$L(T,\alpha) = \prod_j L_j(T,\alpha) \tag{5.14}$$

This reduces the degeneracy (figure 5.7b). The likelihood of each value of T, taking into account the uncertainty in α, can be calculated by marginalising the likelihood, or summing over all values of α to produce a one dimensional likelihood curve (figure 5.8). The 68% confidence levels (the narrowest possible range of values of T to include 68% of the total area under the likelihood curve) were measured as an equivalent of 1σ error bars on a Gaussian distribution.

These measurements were carried out along three 0.48 arcsec wide strips on the left of the image shown in figure 5.5 which contain the brightest emission. The results are shown in figure 5.9 and in the temperature map shown in figure 5.5. The temperature clearly increases from around 1800 K to (2840 ± 230) K (averaging over the most easterly pixel of all three slices) at what may be the shock front. In source A there also appears to be a decrease in temperature of $\sim$ 200 K to the right (east) in the image shown in figure 5.5.

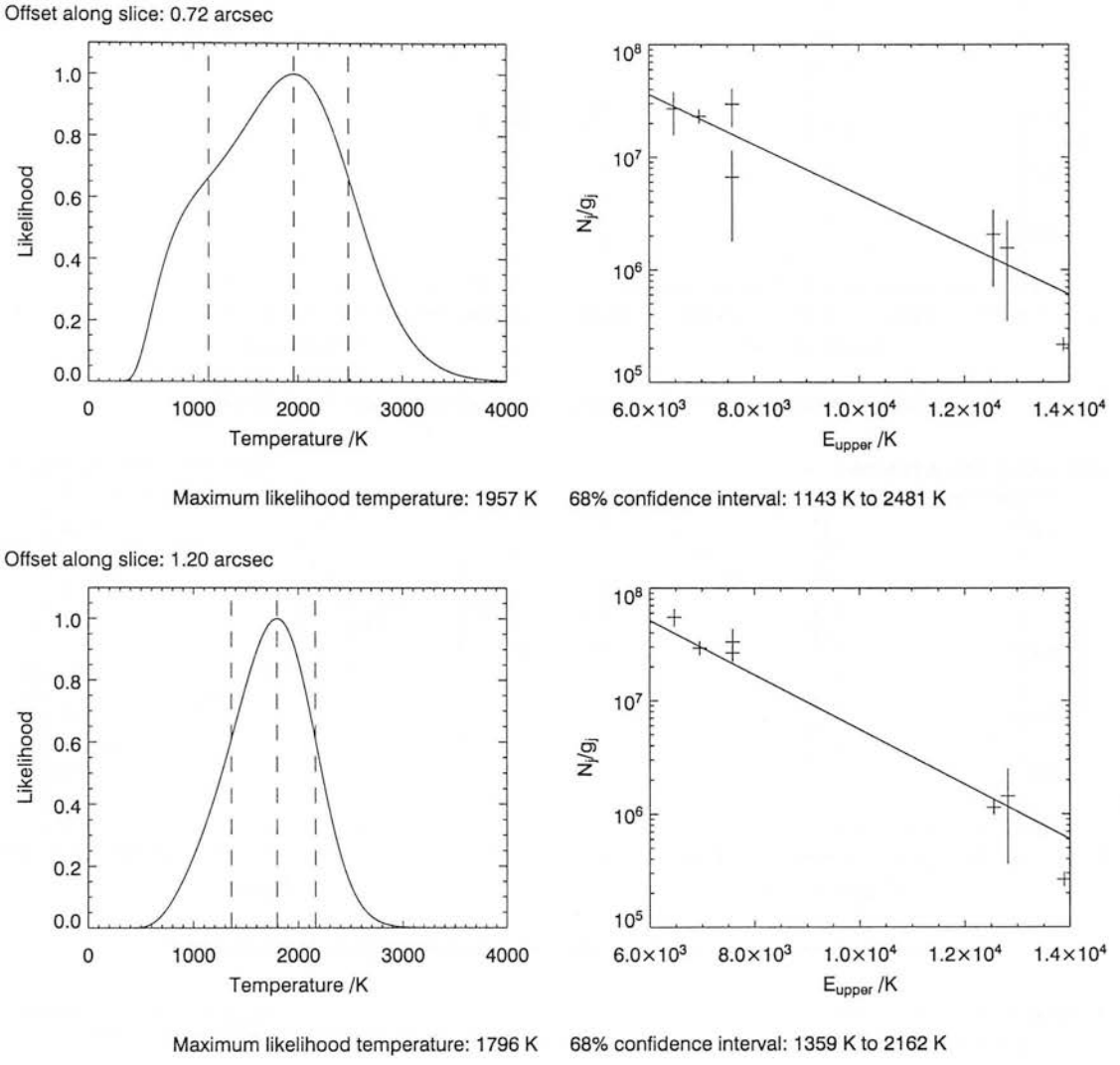

Figure 5.8: These plots show the marginalised likelihood distributions of T and the column densities with a line of the form of equation 5.12 with the most likely value of T and the most likely value of α given T. Each plot is taken from a 0.48×0.48 arcsec^2 region along a strip running parallel to the long axis of the IFU, from 0.48–0.96 arcsec from the left of the image in figure 5.5. The likelihood shown here is normalised to have a maximum value of 1. The maximum likelihood value of T and confidence 68% interval are shown by the dotted lines.

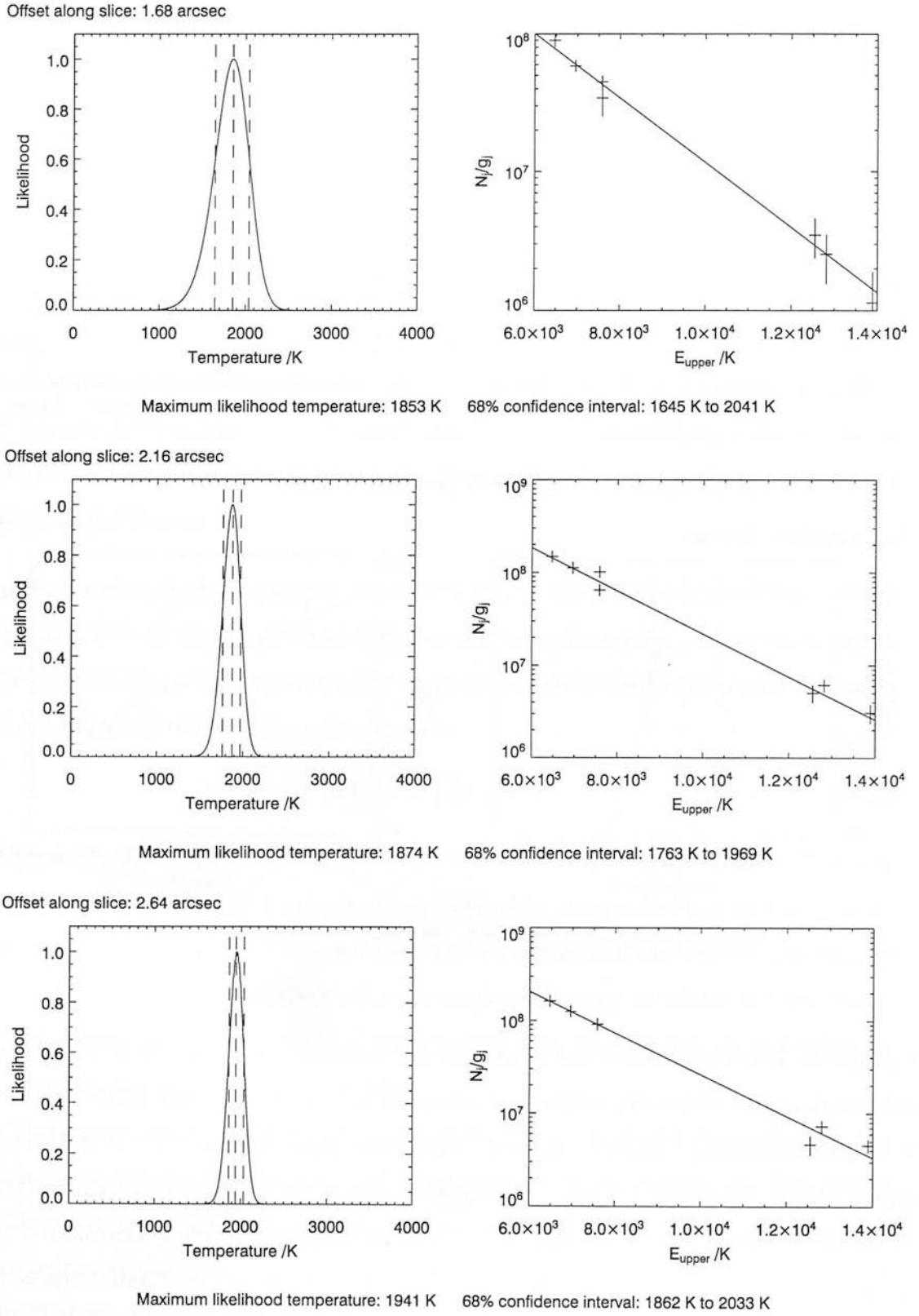

Figure 5.8: *continued*

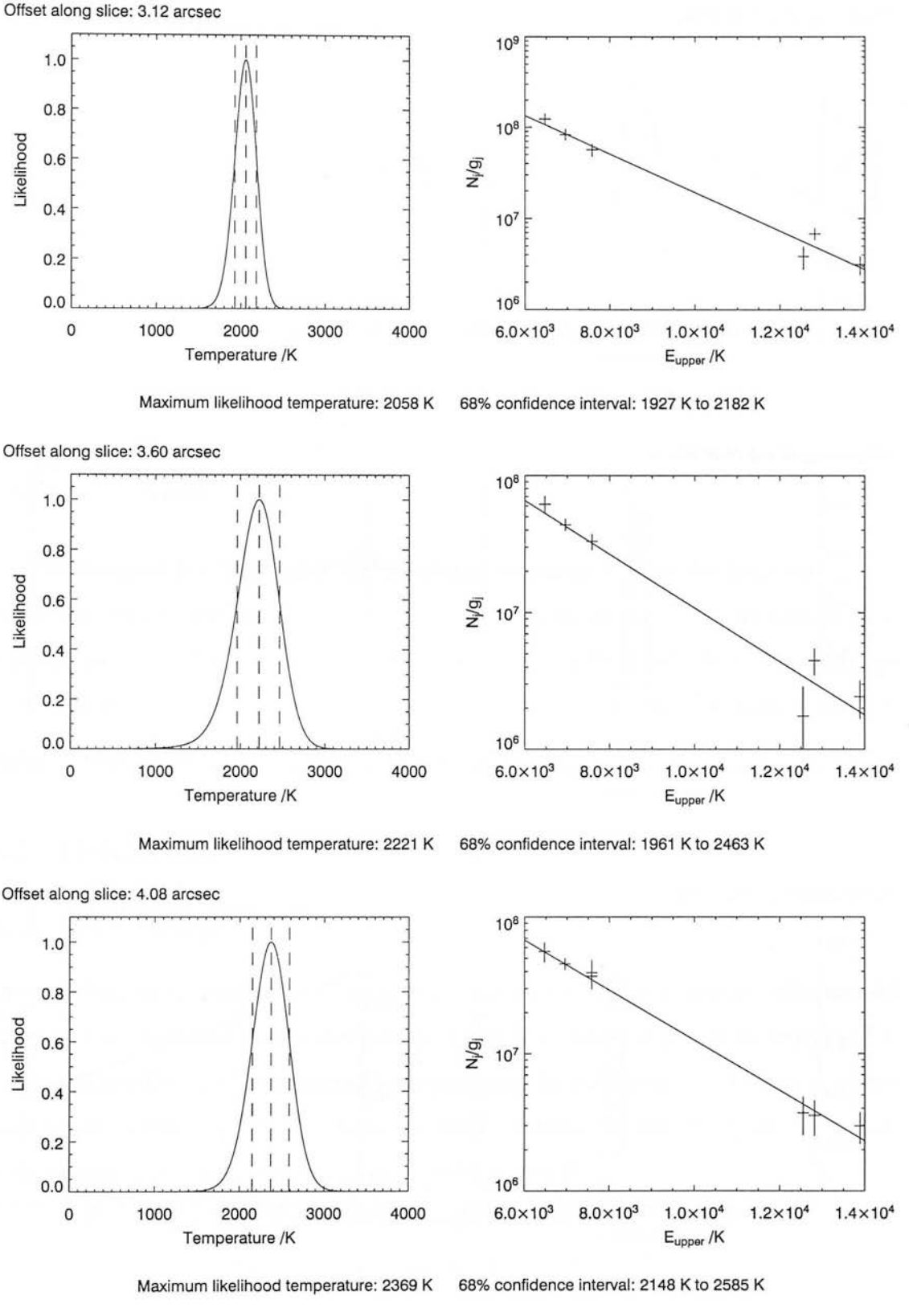

Figure 5.8: *continued*

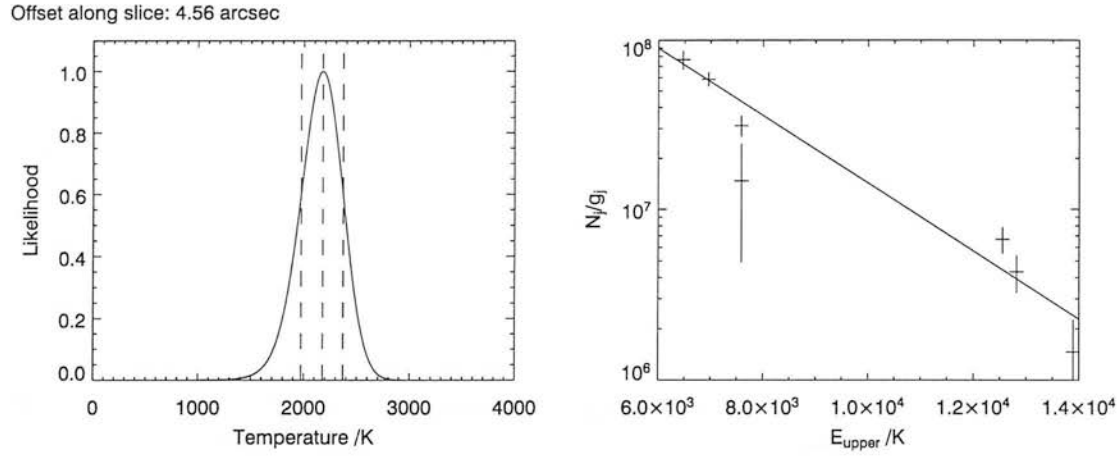

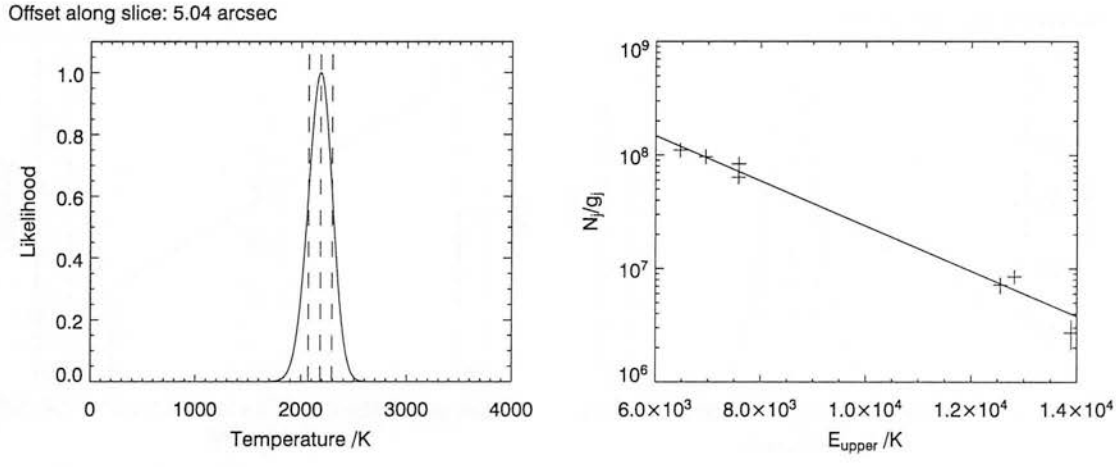

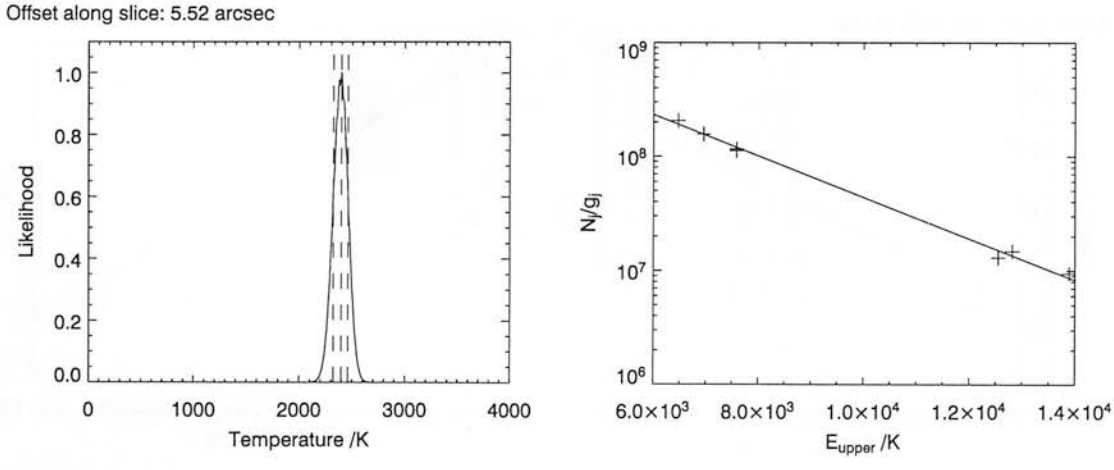

Figure 5.8: *continued*

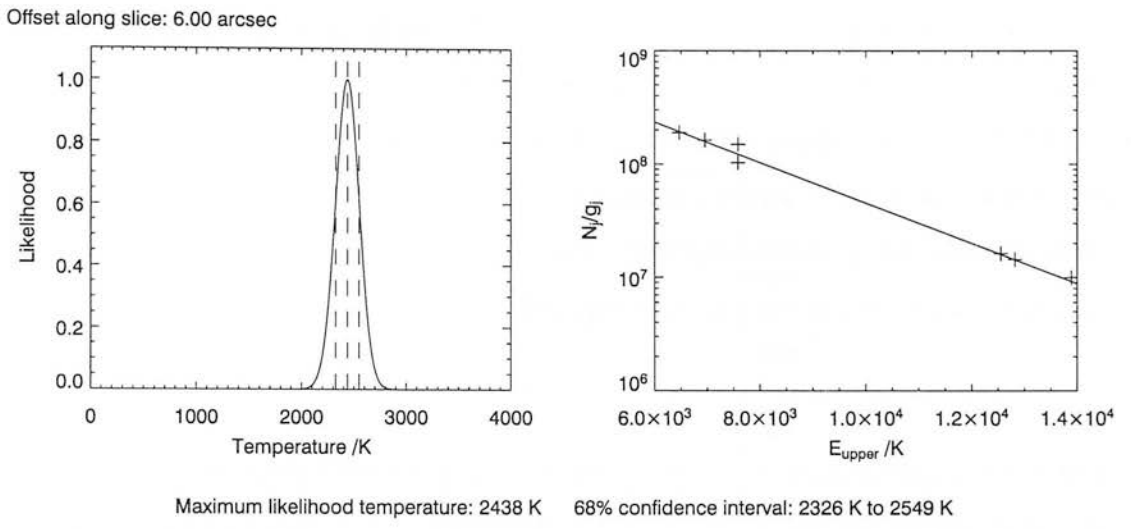

Figure 5.8: *continued*

The fluxes of five lines were also measured in source C from the long-slit spectra described above. Assuming the same extinction value of $A_k = 0.7$ then these give a temperature of 2730 K with 68% confidence levels of 2500 to 2954 K. The assumption of local thermal equilibrium is less likely to be valid in this case than in the IFU observations because we are now averaging over the entire source.

5.3 Discussion

5.3.1 Morphology

One possible interpretation of the morphology of the H_2 emission in this region would be to see sources A and B as bow-shocks in a highly collimated flow from west to east. Sources C and D would be assumed to be produced by a different outflow, or possibly even by two outflows. There is, however, little evidence for this interpretation other than the bow-shock like appearance of sources A and B.

An alternative would be to interpret sources A, B, C and D to all be bright sources in a single outflow originating in or near the H II region. This is suggested by the diffuse emission connecting sources A, B, C and D. The asymmetry in the north-south direction in both intensity and temperature of source A and in the intensity of source B adds support to the idea that the source of the flow is to the NW of A,B,C,D – in

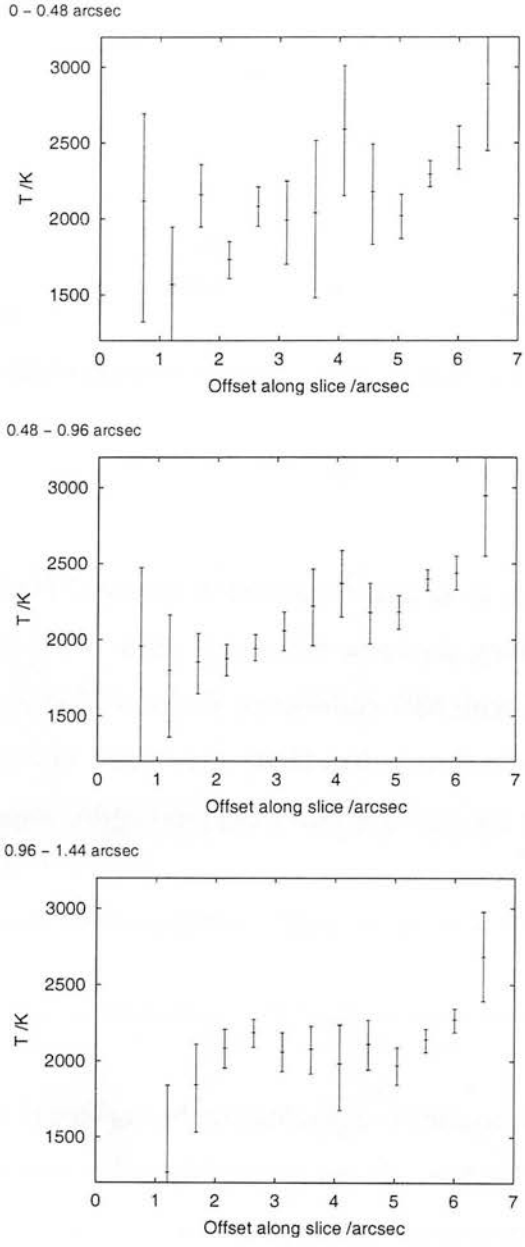

Figure 5.9: The temperature was measured along three 0.48 arcsec wide strips running west-east on the left of figure 5.5. The points and error bars on these plots show the maximum likelihood value and 68% confidence interval on the value of T marginalised over α, as described in the text.

or near the H II region. In figure 5.5 it can be seen that both sources are brighter on the left (south) side than on the right. The temperatures measured in source A are approximately 200 K higher on the south edge of the IFU field than 1.5 arcsec to the north. This implies that sources A and B are not produced by a flow from west to east, which would be expected to produce a symmetrical bow-shock, although asymmetry could also be produced by variations in density in the medium with which the outflow is interacting.

If the flow originates in or close to the H II region, as the morphology of the diffuse emission around sources A–D suggests, then this interpretation would imply that the collimation factor of the outflow is no more than about 3 if we assume that the outflow is at an angle of around 45° to the plane of the sky. This would indicate a lower degree of collimation than is seen in outflows from many lower mass systems. However, if we assume that this emission traces the full width of the outflow then it is significantly more collimated than is thought to be typical for outflows from high mass stars. It does not appear to be completely uncollimated like, for example the Orion outflow [Allen and Burton, 1993]. The emission is in a position consistent with the blue lobe of the massive outflow detected by Shepherd and Churchwell [1996b].

It is unclear whether the fainter diffuse emission to the south and north-east of the H II region are also excited by the same outflow as sources A–D, which would imply some outflow of material at very wide angles. Source E appears to be a highly collimated outflow originating from approximately 15 arcsec west of the H II region, but it is not possible to be certain that it is not a region of dense gas excited by a much wider outflow.

Combining high spatial resolution interferometric radio mapping with infrared imaging would help to resolve these ambiguities. When Beuther et al. [2003] combined interferometric observations with infrared images of IRAS 19410+2336 they found that what had appeared in single dish maps to be two outflows was the combination of at least seven and possibly as many as nine separate outflows. It seems likely that similar results might be found in this region.

5.3.2 Shock excitation

The absence of Brackett-γ emission from atomic hydrogen or Fe II lines and the excitation temperatures measured suggest that the fast C shock model is most appropriate of those described in section 5.1.4. A maximum post-shock temperature of (2840 ± 230) K would be produced by a shock velocity of (37 ± 3) km s^{-1} in the models of Kaufman and Neufeld [1996]. This would be consistent with the 29 km s^{-1} along the line of sight measured by Shepherd and Churchwell [1996b] when the uncertainty on the angle of incidence is taken into account implying an angle of incidence of $(38 \pm 6)°$. This angle is plausible for the outflow detected by Shepherd and Churchwell [1996b] – we know that it has a significant component along the line of sight because that is how the high velocity gas was initially detected and we know from the radio map that there is a significant component parallel to the plane of the sky. The temperatures measured in source A (offsets along the slice of between 4.5 and 6.5 arcsec) clearly decrease with distance from the shock front. The C-shock models of Flower et al. [1996] do predict a steady decrease in temperature over around 0.03 pc (2 arcsec at a distance of 3 kpc) behind the shock front, beyond which point the flux falls rapidly. This is consistent with what we see, though the proximity of source B and the uncertain geometry of the outflow complicates more detailed comparison with the models.

5.4 Summary

We have detected near-IR emission from H_2 excited by outflows in the region of G25.65+1.05. The morphology of the emission is complex and unambiguous interpretation would be greatly assisted by high spatial resolution radio mapping of CO.

The brightest H_2 emission is detected in a position consistent with the blue lobe of the bipolar outflow detected in the low-resolution map of Shepherd and Churchwell [1996b]. If the emission traces the full width of the outflow then the collimation factor of the outflow is ~ 3, higher than the 1 to 1.8 often though to be typical of outflows from high mass stars.

Integral field spectra of a region containing two compact sources of H_2 emission

showed a variation in temperature with a maximum of 2800 K close to the shock front. The temperatures and absence of dissociation suggest a C-shock with a shock velocity of (37 ± 3) km s^{-1}, which is also consistent with this H_2 emission tracing the same outflow as the CO emission detected by Shepherd and Churchwell [1996b]. The temperature in the brighter of the two sources falls steadily over around 0.03 pc at which point the intensity decreases significantly, which is consistent with the C-shock models of Flower et al. [1996].

Chapter 6

Conclusions and future work

6.1 Conclusions

UIST, including the IFU, was successfully commissioned in the autumn of 2002, and is now used by many visiting observers to UKIRT. The UIST IFU has demonstrated that it is practical to design, build and align an image slicing IFU using spherical mirrors, making it sufficiently compact to be mounted on the slit wheel and deployed in a multi-purpose instrument. The lessons learned from designing, building and testing the IFU will assist in the development of future image slicing IFUs.

I have shown here that the IFU works well, making certain types of observation significantly faster and easier than they would previously have been. However, it clearly does not perform quite as well as originally hoped due to the misalignment of the slicing mirrors during machining. This reduced the number of slices from 18 to 14, reducing the field of view by 22%.

The model of the transmission of the IFU which I showed in chapter 2 describes the measured transmission well, and shows that the losses in the IFU are dominated by the reflectivity of aluminium, rather than the surface roughness of the mirrors. The transmission would have been substantially increased by gold coating all the mirrors in the IFU. Gold has a higher reflectivity than aluminium at all wavelengths at which UIST operates [Bass, 1995], particularly at shorter wavelengths where the reflectivity of aluminium dips towards the 0.8 μm absorption feature visible in figure 2.17. A small increase in the reflectivity of all seven optical surfaces would significantly improve the

efficiency of the IFU. At 1 μm, increasing the reflectivity from 92% (aluminium alloy 6061) to 99.1% (gold) would increase the transmission of the IFU by 70%. Even at 5 μm, where the reflectivity of the aluminium alloy is 96%, a gold coating with reflectivity of 99.5% would increase the transmission by 30%.

While, as discussed above, if the IFU were to be built again the usable field of view and the transmission could be increased, the IFU that has been commissioned works sufficiently well to provide significant advantages over the alternative observing modes for many observations. The image quality obtained from the IFU is excellent, though careful calibration of the data-reduction software was essential to accurately reconstruct the image.

Reliable automatic data-reduction is essential for integral field spectroscopy on common user instruments because the raw data is very complex to interpret, making it hard for observers to monitor the progress of the observation. We have demonstrated the feasibility of real-time non-interactive reduction of IFU data. The data-reduction recipes prepared for use with UIST combine calibration frames, and object and sky frames to produce a calibrated datacube which can then be analysed using other software packages. This is a significant advance over the existing ORAC-DR spectroscopy recipes which merely estimated the wavelength scale, leaving the observer to manually calibrate the data using the arc lamp spectrum.

Our observations of the region of G25.65+1.05 demonstrate one class of observations for which the IFU provides a significant advantage over alternative observing techniques. The IFU has greatest advantage over long-slit spectroscopy for mapping extended sources which can be covered by one or a small number of IFU positions. There are also reasons to use the IFU for observations of point sources. Eliminating slit-losses makes the IFU significantly more efficient than the 2-pixel slit under many conditions, while maintaining spectral resolution and providing greater photometric accuracy due to the uncertainty in estimating the flux lost at the slit, which is a function of the seeing and the centring of the star in the slit.

λ_{min}	λ_{max}	Diffraction limit /arcsec at λ_{min}	at λ_{max}	Number of slices	Slice width /arcsec
5.00	7.71	0.21	0.32	18	0.23
7.71	11.89	0.32	0.50	9	0.46
11.89	18.35	0.50	0.77	6	0.69
18.35	28.30	0.77	1.19	6	0.92

Table 6.1: The Mid-infrared instrument (MIRI) on the James Webb space telescope will use four image slicing IFUs, each based on the design of the UIST IFU, each optimised for use over a different range of wavelengths.

6.2 The future of integral field spectroscopy

6.2.1 Mid-infrared integral field spectroscopy with the James Webb Space Telescope

The Mid-infrared instrument (MIRI) of the James Webb Space Telescope (JWST), is designed to provide imaging and integral field spectroscopy at wavelengths of 5–28 μm [European consortium MIRI team, 2002]. Four image slicing IFUs, the design of which is based upon that of the UIST IFU, will observe the field of view over different wavelength ranges simultaneously, using a set of dichroics to split the beam. The parameters of these four IFUs are given in table 6.1. The size and complexity of each is comparable to that of the UIST IFU. The main difference in the building of these IFUs will be in the mounting of the slicing mirrors and reimaging mirrors, which in the UIST IFU are held by friction in a clamp. For MIRI they will need to be fixed in a way which can survive the vibrations expected during the launch. Mid-infrared integral field spectroscopy at high spatial resolutions will provide a means of studying deeply embedded young stars and protostars, protoplanetary discs around nearby stars and very high redshift galaxies (Hα is shifted to 5 μm at a redshift of 6.6).

6.2.2 Multiple integral field spectroscopy

Single IFUs, such as that found in UIST provide an efficient method of obtaining spectra of compact, isolated sources. The slice width and pixel size of the UIST IFU was chosen to fully sample the point spread function of the telescope under most condi-

tions in order to take advantage of the high image quality at UKIRT. However, the IFU only makes use of a very small fraction of the UIST field of view: (3.3×6.0) arcsec^2 out of (2×2) arcmin^2. As larger telescopes are developed with higher spatial resolutions using adaptive optics making efficient use of the image produced by the telescope becomes still more difficult. The multi-conjugate adaptive optics system (MCAO) proposed for Gemini is expected to provide image sizes of 0.1–0.2 arcsec across a field of view up to 3 arcmin across. The Extremely Large Telescopes (ELTs) currently being considered are intended to provide images at the diffraction limit of the 50–100 m primary mirror (10–5 millarcsec at 2 μm) over a 10 arcsec field of view.

One technique which has significantly increased the efficiency of observing with large telescopes is that of multi-object spectroscopy, using either positionable fibres (for example, 2dF at the Anglo-Australian Telescope) or custom made slit masks (for example, GMOS on Gemini). These methods allow spectra to be obtained from a large number of stars or galaxies simultaneously. Studies are currently underway for instruments for Gemini (GIRMOS) and the VLT (KMOS) to develop a technique of multi-object integral field spectroscopy [Ramsay Howat et al., 2003]. These instruments would use a number of robotic pick-off arms which would be positioned in the focal plane. Each would relay a small part of the image to a fixed IFU. The design for GIRMOS proposes the use of 32 pick-off arms feeding 32 IFUs. Such instruments would allow spatially resolved, spectroscopic observations of large numbers of galaxies to be made, providing the data that is required for gaining further understanding of the physical processes within these galaxies. Looking further ahead, one of the primary science goals of ELTs is the study of extremely faint, distant galaxies. Multiple IFUs would be ideal for making these observations.

Bibliography

A. Allan. DATACUBE – an ifs datacube manipulation package. Starlink User Note 237, http://www.starlink.rl.ac.uk/star/docs/sun237.htx/sun237.html, 2001.

D. A. Allen and M. G. Burton. Explosive ejection of matter associated with star formation in the Orion nebula. *Nature*, 363(6424):54–56, 1993.

J. Allington-Smith and R. Content. Sampling and background subtraction in fiber-lenslet integral field spectrographs. *PASP*, 110:1216–1234, 1998.

R. Bacon, Y. Copin, G. Monnet, B. W. Miller, J. R. Allington-Smith, M. Bureau, C. Marcella Carollo, R. L. Davies, E. Emsellem, H. Kuntschner, R. F. Peletier, E. K. Verolme, and P. T. de Zeeuw. The SAURON project – I. the panoramic integral-field spectrograph. *MNRAS*, 326:23–35, 2001.

M. Bass, editor. *Handbook of Optics*, volume 2, chapter Properties of Metals, pages 35.29–35.49. McGraw Hill, 2 edition, 1995.

H. Beuther, P. Schilke, F. Gueth, M. McCaughrean, M. Anderson, T. Sridharan, and K. Menten. IRAS 05458+3543: Multiple outflows at the earliest stages of star formation. *A&A*, 387:931–943, 2002a.

H. Beuther, P. Schilke, T. K. Sridharan, K. M. Menen, C. M. Walmsley, and F. Wyrowski. Massive molecular outflows. *A&A*, 383:892–904, 2002b.

H. Beuther, P. Schilke, and T. Stanke. Multiple outflows in IRAS 19410+2336. *A&A*, 2003.

I. A. Bonnell. The formation of massive stars through stellar collisions. In J. E. Beckman and T. J. Mahoney, editors, *The evolution of galaxies on cosmological timescales*, 1999.

I. S. Bowen. The image-slicer, a device for reducting loss of light at slit of stellar spectrograph. *ApJ*, 88(2):113–123, 1938.

J. Brand and L. Blitz. The velocity field of the galaxy. *A&A*, 275:67–90, 1993.

R. Chapman, S. Beard, M. Mountain, D. Pettie, and A. Pickup. Implementation of a charge integration system in a low background application. In D. L. Crawford, editor, *Instrumentation in Astronomy VII*, volume 1235 of *Proc. SPIE*, pages 34–42, 1990.

E. L. Church and J. M. Zavada. Residual surface roughness of diamond turned optics. *Applied Optics*, 14(8):1788–1795, 1975.

E. Churchwell. Massive star formation: observational constrints. In B. Reipurth and C. Bertout, editors, *IAU Symposium 182 – Herbig-Haro flows and the birth of young stars*, pages 525–536, 1997.

E. Churchwell. Massive star formation: the role of bipolar outflows. In M. Livio, editor, *Unsolved problems in stellar evolution*, pages 41–58. Cambridge, 2000.

R. Content. New design for integral field spectroscopy with 8-m telescopes. In A. L. Ardeberg, editor, *Optical Telescopes of Today and Tomorrow*, volume 2871 of *Proc. SPIE*, pages 1295–1305, 1997.

G. Courtès, Y. Georgelin, R. Bacon, G. Monnet, and J. Boulesteix. A new device for faint objects high resolution imagery and bidimensional spectrography. In L. B. Robinson, editor, *Instrumentation for ground-based optical astronomy*, pages 266–274, 1987.

P. Cox, P. J. Huggins, J. Maillard, E. Habart, C. Morisset, R. Bachiller, and T. Forveille. High resolution near-infrared spectro-imaging of NGC 7027. *A&A*, 384:603–619, 2002.

R. Dallier, J. Cuby, J. Czarny, and J. Baudard. ISIS-IR: the first infrared fibre-fed spectrograph. *Experimental Astronomy*, 3:183–184, 1994.

R. Davies, M. Ward, and H. Sugai. Shock excitation in interacting galaxies: Markarian 266. *ApJ*, 535:735–747, 2000.

L. d'Hendecourt, M. Jourdain de Muizon, E. Dartois, M. Breitfellner, P. Ehrenfreund, J. Benit, F. Boulanger, J. L. Puget, and H. J. Habing. ISO-SWS observations of solid state features towards RAFGL 7009S. *A&A*, 315:L365–L368, 1996.

M. A. Dopita and R. S. Sutherland. *Astrophysics of the diffuse universe*, chapter 8. Springer, 2003.

M. Dubbeldam, R. Content, J. R. Allington-Smith, S. Pokrovski, and D. J. Robertson. Integral field unit for the gemini near-infrared spectrograph. In A. F. M. Masanori Iye, editor, *Optical and IR Telescope Instrumentation and Detectors*, number 4008 in Proc. SPIE, pages 1181–1192, 2000.

F. Economou, T. Jenness, M. Currie, A. Adamson, and A. Allan. ORAC-DR: overview and general introduction. Starlink User Note 230, http://www.jach.hawaii.edu/JACpublic/stardocs/sun230.htx/sun230.html, 2001.

European consortium MIRI team. NGST MIRI instrument concept summary report, 2002.

D. R. Flower, G. Pineau des Forêts, D. Field, and P. W. May. The structure of MHD shocks in molecular outflows: grain sputtering and SiO formation. *MNRAS*, 280: 447–457, 1996.

G. Garay and S. Lizano. Massive stars: their environment and formation. *PASP*, 111: 1049–1087, 1999.

P. M. Gray. Anglo-Australian Observatory fibre system. In D. L. Crawford, editor, *Instrumentation in Astronomy VI*, volume 627 of *Proc. SPIE*, pages 96–104, 1986.

T. G. Hawarden, N. P. Rees, T. C. Chuter, A. C. Chrysostomou, C. P. Cavedoni, R. Rohloff, E. Pitz, D. G. Pettie, R. J. Bennett, and E. Atad-Ettedgui. Postupgrade performance of the 3.8-m United Kingdom Infrared Telescope (UKIRT). In W. Roybal, editor, *Advanced Telescope Design, Fabrication, and Control*, volume 3785 of *Proc. SPIE*, pages 82–93, 1999.

R. Haynes and J. Allington-Smith. SMIRFS-II – multi-object and integral-field unit spectroscopy at the UKIRT. In S. Arribas, E. Mediavilla, and F. Watson, editors, *Fiber optics in astronomy III*, volume 152 of *A.S.P. Conference series*, pages 289–299, 1998.

J. M. Hill, J. R. P. Angel, J. S. Scott, and D. Lindley. Multiple object spectroscopy: the Medusa spectrograph. *ApJ*, 242:L69–L72, 1980.

D. Hollenbach. The physics of molecular shocks in YSO outflows. In B. Reipurth and C. Bertout, editors, *IAU Symposium 182 – Herbig-Haro flows and the birth of young stars*, pages 181–198, 1997.

K. Horne. An optimal extraction algorithm for ccd spectroscopy. *PASP*, 98(609–617), 1986.

T. Jenness and F. Economou. ORAC-DR: programmer's guide. Starlink User Note 233, http://www.jach.hawaii.edu/JACpublic/stardocs/sun233.htx/sun233.html, 2001.

M. J. Kaufman and D. A. Neufeld. Far-infrared water emission from magnetohydrodynamic shock waves. *ApJ*, 456:611–630, 1996.

M. A. Kenworthy, I. R. Parry, and K. A. Ennico. COHSI: a lens array and fiber feed for the near infrared. In S. Arribas, E. Mediavilla, and F. Watson, editors, *Fiber optics in astronomy III*, volume 152 of *A.S.P. Conference series*, pages 300–305, 1998.

A. Krabbe, R. Genzel, A. Eckart, F. Najarro, D. Lutz, M. Cameron, H. Kroker, L. E. Tacconi-Garman, N. Thatte, L. Weitzel, S. Drapatz, T. Geballe, A. Sternberg, and R. Kudritzki. The nuclear cluster of the milky way: Star formation and velocity dispersion in the central 0.5 parsec. *ApJ*, 447:L95–L100, 1995.

D. Lee, R. Haynes, and D. J. Skeen. Properties of optical fibres at cryogenic temperatures. *MNRAS*, 326:774–780, 2001.

P. Martini and D. L. DePoy. Optimal resolutions for ir spectroscopy through the oh airglow. In A. F. M. Masanori Iye, editor, *Optical and IR Telescope Instrumentation and Detectors*, number 4008 in Proc. SPIE, pages 695–702, 2000.

W. H. McCutcheon, P. E. Dewdney, C. R. Purton, and T. Sato. Protostellar candidates in a sample of bright far-infrared IRAS sources. *AJ*, 101:1435–1465, 1991.

T. W. Murphy, K. Matthews, and B. T. Soiffer. A Cryogenic integral field spectrograph for the Palomar 200 inch telescope. *PASP*, 111(763):1176–1184, 1999.

I. R. Parry, A. J. . Dean, R. S. Ellis, D. King, C. D. Mackay, R. G. McMahon, S. R. Medlan, J. M. Pritchard, and A. N. Ramaprakesh. CIRPASS: A Near-IR integral field spectrograph. In W. van Breugal and J. Bland-Hawthorn, editors, *Imaging the universe in three dimensions*, volume 195 of *A.S.P. Conference series*, pages 191–195, 2000.

S. K. Ramsay Howat, M. A. Ellis, D. C. Gostick, P. R. Hastings, M. Strachan, and M. Wells. Integration and testing of the UKIRT imaging spectrometer (UIST). In M. Iye and A. F. Moorwood, editors, *Optical and IR Telescope Instrumentation and Detectors*, volume 4008 of *Proc. SPIE*, pages 1067–1075, 2000.

S. K. Ramsay Howat, R. M. Sharples, G. S. Wright, P. R. Hastings, M. Wells, C. R. Cunningham, J. Schmoll, R. Content, and D. J. Robertson. Multiple integral field spectroscopy using image slicers. In A. F. M. Masanori Iye, editor, *Instrument Design and Performance for Optical/Infrared Ground-based Telescopes*, number 4841 in Proc. SPIE, pages 1315–1325, 2003.

S. K. Ramsay Howat, G. S. Wright, C. M. Mountain, D. Montgomery, and E. I. Atad-Ettedgui. Image quality with array spectrometers. In *Instrumentation in Astronomy VIII*, volume 2198 of *Proc. SPIE*, pages 467–478, June 1994.

E. H. Richardson. The spectrographs of the Dominion Astrophysical Observatory. *J. of the Royal Astronomical Society of Canada*, 62, 313–330 1968.

J. Richer, D. Shepherd, S. Cabrit, R. Bachiller, and E. Churchwell. Molecular outflows from young stellar objects. In *Protostars and Planets IV*, pages 867–894. Arizona, 2000.

N. A. Ridge and T. J. T. Moore. A single distance sample of molecular outflows from high-mass young stellar objects. *A&A*, 378:495–508, Nov. 2001.

P. F. Roche, P. W. Lucas, C. D. Mackay, E. Atad-Ettedgui, P. R. Hastings, A. Bridger, N. P. Rees, S. K. Leggett, C. J. Davis, A. R. Holmes, and T. Handford. UFTI: the 0.8 - 2.5 μm fast track imager for the uk infrared telescope. In A. F. M. Masanori Iye, editor, *Instrument Design and Performance for Optical/Infrared Ground-based Telescopes*, number 4841 in Proc. SPIE, pages 901–912, 2003.

M. S. Seigar, A. J. Adamson, N. P. Rees, T. G. Hawarden, M. J. Currie, and T. C. Chuter. Seeing statistics at the upgraded 3.8m uk infrared telescope (UKIRT). In P. J. Quinn, editor, *Observatory Operations to Optimize Scientific Return III*, volume 4844 of *Proc. SPIE*, pages 366–375, 2002.

D. S. Shepherd and E. Churchwell. Bipolar molecular outflows in massive star formation regions. *ApJ*, 472:225–239, 1996a.

D. S. Shepherd and E. Churchwell. High-velocity molecular gas from high-mass star formation regions. *ApJ*, 457:267–276, 1996b.

K. Shortridge, H. Meyerdierks, M. Currie, M. Clayton, J. Lockley, A. Charles, C. Davenhall, M. Taylor, T. Ash, T. Wilkins, D. Axon, J. Palmer, A. Holloway, and V. Graffagnino. FIGARO – a general data reduction system. Starlink User Note 86, http://www.starlink.rl.ac.uk/star/docs/sun86.htx/sun86.html, 2002.

A. Sternberg. The excitation of molecular hydrogen and its significance. In *Infrared spectroscopy in astronomy*, pages 269–280. ESA, 1988.

A. Sternberg and A. Dalgarno. The infrared response of molecular hydrogen gas to ultraviolet radiation: high-density regions. *ApJ*, 338:197–233, 1989.

M. Tecza, N. A. Thatte, F. Eisenhauer, S. Mengel, C. Roehrle, and K. Bickert. SPIFFI image slicer: revival of image slicing with plane mirrors. In A. F. M. Masanori Iye, editor, *Optical and IR Telescope Instrumentation and Detectors*, number 4008 in Proc. SPIE, pages 1344–1350, 2000.

S. P. Todd. ORAC-DR: integral field spectroscopy data reduction. Starlink User Note 246, http://www.jach.hawaii.edu/JACpublic/stardocs/sun246.htx/sun246.html, 2003.

C. Vanderriest and J.-P. Lemonnier. SILFID: a versatile fiber-optics spectrograph for faint objects. In L. B. Robinson, editor, *Instrumentation for ground-based optical astronomy*, pages 304–310, 1987.

A. J. Walsh, M. G. Burton, A. R. Hyland, and G. Robinson. Studies of ultracompact H II regions - ii. high-resolution radio continuum and methanol maser survey. *MNRAS*, 301:640–698, 1998.

L. Weitzel, A. Krabbe, H. Kroker, N. Thatte, L. Tacconi-Garman, M. Cameron, and R. Genzel. 3d: The next generation near-infrared imaging spectrometer. *A&AS*, 119: 531–546, 1996.

M. Wells, P. R. Hastings, and S. K. Ramsay Howat. Design and testing of a cryogenic image slicing IFU for UKIRT and NGST. In *Optical and IR Telescope Instrumentation and Detectors*, volume 4008 of *Proc. SPIE*, pages 1215–1226, 2000.

D. O. S. Wood and E. Churchwell. The morphologies and physical properties of ultracompact H II regions. *ApJS*, 69:831–895, 1989.

A. Zavagno, L. Deharveng, D. Nadeau, and J. Caplan. Near-infrared imaging of RAFGL7009S. *A&A*, 394:225–229, 2002.

Q. Zhang, T. R. Hunter, J. Brand, T. K. Sridharan, S. Molinari, M. A. Kramer, and R. Cesaroni. Search for CO outflows toward a sample of 69 high-mass protostellar candidates: frequency of occurrence. *ApJ*, 552:L167–L170, 2001.